

**Surface Science Approach to Catalyst Preparation:  
Palladium Deposition onto Iron Oxide Films from the  
Liquid Phase**



**Dissertation**

zur Erlangung des akademischen Grades des

**Doktors der Naturwissenschaften**

(Dr. rer. nat.)  
im Fach Chemie

eingereicht im Fachbereich Biologie, Chemie, Pharmazie  
der Freien Universität Berlin

vorgelegt von

**Hui-Feng Wang**

Berlin 2012

Diese Arbeit wurde von November 2008 bis Dezember 2011 am Fritz-Haber-Institut der Max-Planck-Gesellschaft in der Abteilung Chemische Physik unter Anleitung von Herrn Prof. Dr. H.-J. Freund angefertigt.

Gutachter:

1. Prof. Dr. H.-J. Freund
2. Prof. Dr. T. Risse

Disputation am: 02.10.2012

*The whole of science is nothing more than a refinement of everyday thinking.*

— *Albert Einstein*

**Dedicated to  
my beloved wife and son**

---

## ACKNOWLEDGEMENTS

First and foremost, I must thank my supervisor, Prof. Dr. Hans-Joachim Freund, for giving me the chance to study in his department. He has provided me a lot of opportunities such as seminars, conferences and workshops to communicate with different people and learn new things. His broad knowledge and wisdom have inspired me to improve myself as a scientist and a person.

I would like to thank Prof. Dr. Thomas Risse for being my co-supervisor and reviewing my thesis. I am also grateful for his instructions when he was the coordinator of the International Max Planck Research School (IMPRS).

I would like to particularly acknowledge Dr. Martin Sterrer. As the group leader, he has given a lot of help and instructions for my PhD work. He always encourages and helps me when I meet problems. After every discussion with him, I can get inspiration and have a deeper understanding of topics that we have discussed.

During my time working in the Catalysis/Laser Spectroscopy group which is a quite international team, I have met many great people and worked very well with them. I am grateful to Dr. Hiroko Ariga for helping me at the beginning of my PhD study and Dr. Bill Kaden and Dr. Esther Carrasco for their help and discussions. Rhys Dowler is my best partner in my PhD work. Thank him for sharing the machine and reading my thesis. It is a very nice experience with Rhys to help each other in the lab. Many thanks would also go to Dr. Matthew Brown, Franziska Ringleb and Yuichi Fujimori for discussions and support. I am thankful to Burkhard Kell for a lot of technical supports.

I would also like to thank Jan Rocker and Anja Seiler for IRAS measurement, Walter Wachsmann for helping with ultrapure water system in the chemistry lab and Max Schönberg for helping with single metal crystals preparation.

I would like to thank our secretaries, Gabriele Mehnert and Manuela Misch, for a lot of administration work.

I would like to thank Bettina Menzel for her cares and support in IMPRS and thank Dr. Niklas Nilius and all other people in IMPRS. I have had a very good time with all of you through seminars, block courses and workshops.

I would like to thank my Chinese friends in our department. They are Dr. Xiang Shao, Dr. Bing Yang, Dr. Yi Pan, Dr. Hengshan Qiu, Dr. Yi Cui, Xin Yu, Bo Hong Liu, Dr. Yingna Sun, Dr. Yu Lei, Dr. Xiao Lin, Dr. Zhihui Qin, Dr. Kai Huang and Xin Song. Thank you all for helping with my life in Berlin. I also want to thank all other Chinese friends at the Fritz Haber Institute.

I would like to thank all other colleagues in the department for their help and support with the things I could not handle by myself.

Finally I would like to thank my loving wife, Yanhua Zhao, for her understanding, support and encouragement during these years. Without her support, I cannot finish my study so smoothly. I want to especially thank my lovely son, Hugo Bohu Wang, who has brought me so much joy. It is him, makes me forget any worry and feel happy every day.

---

## ABSTRACT

In this work, results of surface science studies related to the preparation of supported metal catalysts on well-defined oxide surfaces applying procedures used in real-world catalysis are presented. Specifically, a thin  $\text{Fe}_3\text{O}_4(111)$  film grown on  $\text{Pt}(111)$  was chosen as support and its surface was exposed to solutions of  $\text{PdCl}_2$  in order to deposit a Pd precursor. Scanning Tunneling Microscopy (STM) combined with X-ray Photoelectron Spectroscopy (XPS) have been applied to track both morphological and chemical changes that come along with the transformation of the adsorbed Pd precursor into nanoparticles in the early stages of catalyst preparation. The chemical properties of the prepared Pd model catalyst have been investigated by Temperature Programmed Desorption (TPD) and Infrared Reflection Absorption Spectroscopy (IRAS).

For the supported Pd model catalyst prepared by impregnation of  $\text{Fe}_3\text{O}_4(111)$  films with acidic (pH 1.3)  $\text{PdCl}_2$  solution, STM and XPS results provide evidence for homogeneous nucleation of Pd particles out of a monolayer of adsorbed precursor, and an enhancement of the particle-support interaction with increasing annealing temperature. Chlorine, which remains on the model catalyst surface after vacuum annealing, could be removed by oxidation/reduction. However such a treatment leads to particle sintering. A Pd sample prepared through deposition-precipitation using a pH 10  $\text{PdCl}_2$  solution shows a different particle evolution behavior as compared to the pH 1.3 sample because of the different precursor speciation and chemical decomposition mechanism. A comparison of  $\text{Pd}/\text{Fe}_3\text{O}_4$  samples created via Pd evaporation under UHV conditions and that resulting from the solution deposition of Pd-hydroxo complexes reveals that changes in the interfacial functionalization of the support surface govern the differences in Pd nucleation behavior observed. The effect of solution pH on Pd loading and particle size during preparation has been studied. Homogeneously distributed Pd particles with narrow size distribution are formed on  $\text{Fe}_3\text{O}_4(111)$  from low and high pH  $\text{PdCl}_2$  solutions. Post-preparation treatment by oxidation and CO reduction leads to CO chemisorptive features characteristic of Pd nanoparticles.  $\text{H}_2$  reduction of a  $\text{Pd}/\text{Fe}_3\text{O}_4$  sample, however, induces the strong metal support interaction (SMSI) with Pd-Fe alloy formation.

## ZUSAMMENFASSUNG

Die vorliegende Arbeit hat Untersuchungen zur Präparation von oxidgeträgerten Metallkatalysatoren zum Thema, wobei als Ziel verfolgt wurde, die zur Herstellung technischer Katalysatoren üblichen Prozeduren auf einkristalline Oxidsubstrate anzuwenden und mit Hilfe des Einsatzes von aus der Oberflächenphysik und -chemie bekannten Analyseverfahren detaillierte Aussagen über die Katalysator-Vorstufen zu treffen. Als Modellsubstrat wurde ein dünner  $\text{Fe}_3\text{O}_4(111)$ -Film verwendet, auf dessen Oberfläche Pd-Präkursoren aus  $\text{PdCl}_2$ -Lösungen aufgebracht wurden. Die morphologischen und chemischen Änderungen während der Überführung der Pd-Präkursoren in Pd-Nanopartikel wurden mit der Raster-Tunnelmikroskopie (STM) und der Röntgen-Photoelektronenspektroskopie (XPS) verfolgt. Die chemischen Eigenschaften der aktivierten Modellkatalysatoren wurden zusätzlich mit Thermischer Desorptionsspektroskopie (TPD) und Infrarotspektroskopie (IRAS) untersucht.

Für die durch Imprägnation mit einer sauren (pH 1.3)  $\text{PdCl}_2$ -Lösung präparierten Pd Modellkatalysatoren liefern die STM- und XPS-Ergebnisse den Befund, daß die Pd-Partikel aus einer Monolage adsorbierter Pd-Komplexe über homogene Nukleation gebildet werden und die Partikel-Substrat-Wechselwirkung zunimmt, wenn die Probe bei höheren Temperaturen getempert wird. Das von der thermischen Zerlegung der Präkursoren auf der Oberfläche zurückbleibende Chlor kann durch Oxidation beseitigt werden. Diese Behandlung führt jedoch auch zu starkem Sintern der Partikel. Die Bildung eines Pd-Modellkatalysators unter Verwendung einer pH 10  $\text{PdCl}_2$ -Lösung („Deposition-Precipitation“) unterscheidet sich von der bei Verwendung einer pH 1.3 Lösung gefundenen aufgrund der unterschiedlichen Pd-Speziation in der Lösung und des daraus resultierenden chemischen Abbau-Mechanismus. Sowohl mit sauren als auch mit basischen  $\text{PdCl}_2$ -Lösungen als Präkursoren konnten Pd-Nanopartikel mit schmaler Partikelgrößenverteilung erhalten werden. Ein Vergleich von Pd/ $\text{Fe}_3\text{O}_4$  Proben, die entweder durch Verdampfen von Pd im Ultrahochvakuum, oder durch Deposition von Pd-hydroxo-Komplexen erzeugt wurden, zeigt, daß Unterschiede im Pd-Nukleationsverhalten der beiden Proben auf die Oberflächeneigenschaften des Oxidträgers zurückgeführt werden können. Die für Pd-Nanopartikel typischen CO-Chemisorptionseigenschaften konnten nach Aktivierung mit CO beobachtet werden, während eine Aktivierung mit  $\text{H}_2$  zu einer starken Metall-Substrat-Wechselwirkung (SMSI) führt, die die Bildung von PdFe-Legierungspartikel zur Folge hat.

# CONTENTS

<b>ACKNOWLEDGEMENTS</b> .....	<b>I</b>
<b>ABSTRACT</b> .....	<b>II</b>
<b>ZUSAMMENFASSUNG</b> .....	<b>III</b>
<b>LIST OF FIGURES</b> .....	<b>VI</b>
<b>LIST OF TABLES</b> .....	<b>XII</b>

## Chapter 1 Introduction

1.1 Catalysis and surface science .....	1
1.2 Supported catalyst preparation and characterization .....	3
1.3 Motivation of our work .....	8
1.4 Outline of this thesis .....	9

## Chapter 2 Experimental set-up and techniques

2.1 Set-up.....	12
2.1.1 UHV chamber and liquid-STM .....	12
2.1.2 UHV-to-liquid transfer system .....	13
2.1.3 Sample holder and liquid cell.....	14
2.2 Surface science techniques .....	16
2.2.1 Scanning Tunneling Microscopy (STM).....	16
2.2.2 X-ray Photoelectron Spectroscopy (XPS).....	21
2.2.3 Low Energy Electron Diffraction (LEED) .....	29
2.2.4 Temperature Programmed Desorption (TPD).....	30

## Chapter 3 The chemistry of Pd catalyst preparation

3.1 Introduction.....	34
3.2 The chemistry of PdCl <sub>2</sub> solution .....	34
3.3 The oxide surface .....	37
3.4 Overview of catalyst preparation methods .....	38
3.5 Wet chemical catalyst preparation procedures and surface science – restrictions.....	41

## Chapter 4 Single crystalline FeO(111)/Pt(111) and Fe<sub>3</sub>O<sub>4</sub>(111)/Pt(111) films

4.1 Introduction.....	43
4.2 Properties of FeO(111) and Fe <sub>3</sub> O <sub>4</sub> (111) .....	43
4.3 Stability and structure of FeO(111)/Pt(111) film in air and liquid water.....	48
4.3.1 STM characterization.....	48
4.3.2 Chemical characterization .....	51
4.3.3 Discussion .....	51
4.4 In situ STM study of FeO(111)/Pt(111) film in aqueous solution.....	53
4.5 Fe <sub>3</sub> O <sub>4</sub> (111)/Pt(111) film.....	54
4.6 Summary .....	57

## Chapter 5 Pd deposition on iron oxide films using wet chemical methods

5.1 Introduction.....	59
-----------------------	----

5.2 Experimental procedure for wet chemical deposition of Pd onto single-crystalline Fe <sub>3</sub> O <sub>4</sub> (111) thin film samples.....	60
5.3 Initial Pd deposition experiments on FeO(111)/Pt(111).....	61
5.4 Pd on Fe <sub>3</sub> O <sub>4</sub> (111) – wet impregnation (pH 1) .....	63
5.4.1 From wet deposition to UHV thermal reduction.....	63
5.4.2 Interaction of Pd particles with oxide support.....	67
5.5 Pd on Fe <sub>3</sub> O <sub>4</sub> (111) – modified deposition-precipitation (pH 10).....	69
5.6 Effect of solution pH.....	73
5.7 Morphological comparison with PVD Pd/Fe <sub>3</sub> O <sub>4</sub> (111) .....	77
5.8 Summary .....	80

## **Chapter 6 Activation of Pd/Fe<sub>3</sub>O<sub>4</sub> catalyst**

6.1 Introduction.....	83
6.2 Catalyst activation: oxidation and CO reduction .....	85
6.3 Effect of reduction atmosphere .....	88
6.3.1 Results.....	88
6.3.2 Discussion .....	92
6.4 CO oxidation .....	95
6.4.1 Non-catalytic test .....	96
6.4.2 Catalytic test.....	97
6.5 Summary .....	98

## **Chapter 7 Summary and outlook**

<b>Abbreviations.....</b>	<b>103</b>
<b>Curriculum Vitae.....</b>	<b>104</b>
<b>Publications and conference presentations.....</b>	<b>105</b>
<b>Bibliography.....</b>	<b>106</b>

---

## LIST OF FIGURES

Fig. 1.1. Surface topography and chemical composition of an industrial ammonia synthesis catalyst.

Fig. 1.2. Several possibilities for modeling catalysts exist between the industrial system with a high surface area, porous support (left) and the surface of a single crystal (right).

Fig. 1.3. General preparation scheme of supported catalysts.

Fig. 1.4. Interaction models between a transition metal ion (TMI) of a precursor complex and an oxide support.

Fig. 1.5. (a) Schematic illustration of model supported catalyst consists of supported metal particles and thin oxide film grown on conducting substrate; (b) STM images of Ag(001) single crystal, thin film of 8 ML MgO(001) supported on single crystal Ag(001), Au atoms deposited on MgO film at 5 K in UHV and 3D Au particles formed after annealing at 300 K.

Fig. 2.1. The picture of the liquid-STM including scanner head, tip adjusting device, aluminum chamber and damping stage.

Fig. 2.2. Schematic illustration of the UHV-to-liquid transfer system.

Fig. 2.3. Sample holder (top) and UHV sample transfer (bottom).

Fig. 2.4. Scheme of the liquid cell and its state in the liquid STM chamber.

Fig. 2.5. Potential energy diagram of the tunneling process. Tunneling from the filled states in tip into empty states in the sample occurs when a negative bias voltage is applied to the tip.

Fig. 2.6. Schematic illustration of the working principle of an STM instrument.

---

Fig. 2.7. The principle of X-ray photoelectron spectroscopy.

Fig. 2.8. The three-step model of photoemission process.

Fig. 2.9. Energy level diagram for the photoemission process.

Fig. 2.10 Universal curve for electron mean free path.

Fig. 2.11. Schematic illustration of the process for the creation of Auger electron.

Fig. 2.12. The relation between the vector of the real lattice ( $a$ ) and the vector of the reciprocal lattice ( $a^*$ ).  $\delta_{ij}$  is the Kronecker delta,  $\delta_{11}=\delta_{22}=1$ ,  $\delta_{12}=\delta_{21}=0$ .

Fig. 3.1. The upper row shows fresh solutions of 5 mM PdCl<sub>2</sub> with different pH, and the lower row shows the same series of solutions after 12 h aging.

Fig. 3.2. UV-vis Spectroscopy of 0.1 mM PdCl<sub>2</sub> solutions of different pH.

Fig. 4.1. (a) Model structure of single crystal FeO(111) with side view (left) and top view (right), (b) model structure, LEED pattern and STM image with atomic resolution of FeO(111)/Pt(111) thin film.

Fig. 4.2. (a) Model structure of single crystal Fe<sub>3</sub>O<sub>4</sub>(111) with side view (left) and top view (right); (b) LEED pattern and STM images of Fe<sub>3</sub>O<sub>4</sub>(111)/Pt(111) film.

Fig. 4.3. XPS spectra of evaporated elemental Fe film and iron oxide films grown on Pt(111). FeO(111) film (1-2 ML), and at least 10 nm thick Fe<sub>3</sub>O<sub>4</sub>(111) film and  $\alpha$ -Fe<sub>2</sub>O<sub>3</sub>(0001) films.

Fig. 4.4. STM images of FeO films taken in air at bias voltages of -0.3 V (a), -1.8 V (b) and 1.0 V (c). All images are 60 nm  $\times$  60 nm.

Fig. 4.5. STM images of FeO films taken in-situ in liquid water (a), in air after in liquid water (b). Both images are 60 nm  $\times$  60 nm.

Fig. 4.6. STM images of FeO films firstly contact with liquid water at RT, and then heated to 373 K, 800 K and 1000 K in UHV. All images are  $100 \text{ nm} \times 100 \text{ nm}$ .

Fig. 4.7. XPS and PM-IRAS spectra from clean FeO(111)/Pt(111) after contact with air and liquid water. (a) XPS O1s region, (b) XPS Fe 2p region, (c) PM-IRAS OH region.

Fig. 4.8. Energy profile for the oxidation of the FeO/Pt(111) film upon exposure to  $\text{O}_2$  at high oxygen coverage. Blue (Fe), red (O), yellow (C), gray (Pt)

Fig. 4.9. In-situ STM images of FeO films in pH 3 HCl solution (a), pH 10 NaOH solution (b), in 0.1 mM  $\text{PdCl}_2$  pH 3 solution (c) and in 2 mM  $\text{PdCl}_2$  pH 10 solution (d). All images are  $40 \text{ nm} \times 40 \text{ nm}$ .

Fig. 4.10. Large scale ( $365 \text{ nm} \times 365 \text{ nm}$ ) STM image and atomically resolved features on a terrace (inset image) ( $10 \text{ nm} \times 10 \text{ nm}$ ) of  $\text{Fe}_3\text{O}_4$  (111)/Pt (111) film taken in air.  $U_t = -0.05 \text{ V}$ ,  $I_t = 0.2 \text{ nA}$ . The image has not been corrected for instrumental drift and, therefore, the hexagonal lattice is slightly distorted.

Fig. 4.11. a) STM images of  $\text{Fe}_3\text{O}_4$  films taken in air after in contact with blank pH 1.3 solution for 1 h, after annealing to 600 K in UHV and additional oxidation and reduction treatment; b) STM images of  $\text{Fe}_3\text{O}_4$  films after in contact with blank pH 10 solution for 1 h, after annealing to 600 K in UHV.

Fig. 4.12. Fe 2p (a) and Cl 2p (b) of XPS for  $\text{Fe}_3\text{O}_4$  sample in contact with pH 1.3 solution and annealing to 390 K and 600 K in UHV.

Fig. 5.1. (a) STM images of Pd/FeO samples prepared by Pd deposition from  $\text{PdCl}_2$  solution (0.2 mM, pH 10) for 1 h and then heated to different temperature in UHV; (b) a characteristic AES of Pd sample. All images are  $100 \text{ nm} \times 100 \text{ nm}$ .

Fig. 5.2. STM images (a and b) with line profile (c) of Pd/FeO samples prepared using pH 10 solutions of 2 mM  $\text{PdCl}_2$  for 30 min deposition and then annealing sample at different temperatures in UHV. Both images are  $60 \text{ nm} \times 60 \text{ nm}$ .

---

Fig. 5.3. Series of STM images ( $100\text{ nm} \times 100\text{ nm}$ ) of  $\text{Fe}_3\text{O}_4(111)/\text{Pt}(111)$  films taken in air after contact with  $\text{PdCl}_2$  (15 mM, pH 1.3) solution (left) directly after removing the solution, (middle) after UHV-annealing at 390 K, and (right) after UHV-annealing at 600 K.

Fig. 5.4. a) Pd 3d, and b) Cl 2p photoemission spectra of  $\text{Fe}_3\text{O}_4(111)$  exposed to  $\text{PdCl}_2$ (pH 1.3). The spectra were recorded directly after exposure to  $\text{PdCl}_2$  solution at RT (top), after subsequent annealing to 390 K (middle), and 600 K (bottom). The Cl 2p spectra of a  $\text{Fe}_3\text{O}_4(111)$  sample that has been exposed to HCl (pH 1.3, blank experiment) are shown as gray traces in b).

Fig. 5.5. STM images ( $70\text{ nm} \times 70\text{ nm}$ ) showing the same area of  $\text{Fe}_3\text{O}_4(111)/\text{Pt}(111)$  exposed to  $\text{PdCl}_2$  (pH 1.3) and annealed to 390 K in subsequent STM scans. The majority of particles present in the left image are only weakly bound to the surface and easily removed by the STM tip.

Fig. 5.6. a) STM image ( $100\text{ nm} \times 100\text{ nm}$ ) of the  $\text{Fe}_3\text{O}_4(111)\text{-PdCl}_2$  (pH 1.3) sample after 600 K annealing (a) and additional oxidation and reduction treatment to remove chlorine (b).

Fig. 5.7. STM images of  $\text{Fe}_3\text{O}_4(111)$  films were taken after contacting with  $\text{PdCl}_2$  (pH 10) solution for 60 min at RT (a), after UHV-annealing at 390 K (b), after UHV-annealing at 600 K (c and d). All images are  $100\text{ nm} \times 100\text{ nm}$  except (c) which is  $300\text{ nm} \times 300\text{ nm}$ .

Fig. 5.8. Pd 3d photoemission spectra of  $\text{Fe}_3\text{O}_4(111)$  exposed to  $\text{PdCl}_2$  (pH 10). The spectra were recorded (top) directly after exposure to  $\text{PdCl}_2$  solution at RT, (middle) after subsequent annealing to 390 K in UHV, and (bottom) after further annealing to 600 K in UHV.

Fig. 5.9. Pd 3d XPS (a) and Cl 2p XPS (b) of  $\text{Fe}_3\text{O}_4$  samples just after Pd deposition from three different pH solutions, pH 1.6, pH 2.5 and pH 4.7.

Fig. 5.10. STM images ( $75\text{ nm} \times 75\text{ nm}$ ) (a-e) of  $\text{Pd}/\text{Fe}_3\text{O}_4$  samples prepared using different pH values of the precursor solution (5 mM  $\text{PdCl}_2$  solution, 0.016 M Cl<sup>-</sup>) followed by annealing at 600 K in UHV. f) The dependence of particle size on solution pH.

Fig. 5.11. STM images of Pd particles formed on  $\text{Fe}_3\text{O}_4(111)$  by PVD with coverage of a) 4 Å, b) 2 Å and c) 0.5 Å, and after contact with pH 10  $\text{Pd}^{2+}$  precursor solution for d) 60 min, e) 30 min, and f) 10 min. and subsequent thermal reduction at 600 K in UHV. All samples were annealed to 600 K prior to STM imaging. Image size: a), b), d), e): 100 nm x 100 nm, c), f): 60 nm x 60 nm.

Fig. 5.12. a) shows the particle density of Pd particles for the various preparations (black: PVD; red: precursor solution) and b), c) and d) represent the particle size distributions of samples (PVD 4 Å/precursor 60 min), (PVD 2 Å/precursor 30 min) and (PVD 0.5 Å/precursor 10 min), respectively as shown in Figure 5.11.

Figure 5.13. a) STM image ( $100 \times 100 \text{ nm}^2$ ) of PVD Pd on  $\text{Fe}_3\text{O}_4(111)$  chemically modified by exposure to pH 10 NaOH solution. The sample was heated to 600 K in UHV prior to STM imaging. b) Particle size distribution of Pd particles formed by PVD on clean  $\text{Fe}_3\text{O}_4(111)$  (black), interaction with Pd precursor solution for 60 min. (red), and PVD of Pd on a  $\text{Fe}_3\text{O}_4(111)$  surface that has been exposed to pH 10 NaOH solution (blue).

Fig 6.1. Pd 3d and Fe 2p XPS of Pd/ $\text{Fe}_3\text{O}_4$  sample (pH10) after preparation (annealing at 600 K), oxidation and CO reduction.

Fig. 6.2. TPD spectra of CO from Pd/ $\text{Fe}_3\text{O}_4$  (pH 10) sample were taken after oxidation and CO reduction, respectively. Prior to TPD 10 L CO was dosed at RT. Heating rate was 3 K/s.

Fig. 6.3. IRAS spectra taken at 80 K for CO saturation coverage on Pd/ $\text{Fe}_3\text{O}_4$  (pH 10) sample after oxidation and reduction, respectively.

Fig. 6.4. (a) TPD spectra of Pd/ $\text{Fe}_3\text{O}_4$  sample (pH 10) after taken after CO reduction,  $\text{H}_2$  reduction, reoxidation and CO reduction, respectively; (b) TPD spectra of Pd/ $\text{Fe}_3\text{O}_4$  sample prepared by PVD and after  $\text{H}_2$  reduction treatment.

Fig. 6.5. STM images ( $108 \text{ nm} \times 108 \text{ nm}$ ) of Pd/ $\text{Fe}_3\text{O}_4$  sample (pH10). (a) After annealing at 600 K, (b) after  $\text{H}_2$  reduction at 573 K for 30 min.

---

Fig. 6.6. Pd 3d and Fe 2p photoemission spectra of “wet” Pd/Fe<sub>3</sub>O<sub>4</sub>(111) (a), PVD Pd/Fe<sub>3</sub>O<sub>4</sub>(111) (b) and Fe<sub>3</sub>O<sub>4</sub>(111) after contact with pH 10 NaOH solution (c) samples after a series of treatments.

Fig. 6.7. IRAS of Pd/Fe<sub>3</sub>O<sub>4</sub> sample (pH 10) taken at 80 K after CO reduction, H<sub>2</sub> reduction, respectively.

Fig. 6.8. CO<sub>2</sub>-TPD spectra of Pd/Fe<sub>3</sub>O<sub>4</sub> sample (pH 10) reduced with CO or H<sub>2</sub> by dosing 10 L CO initially.

Fig. 6.9. CO<sub>2</sub>-TPD spectra of Pd/Fe<sub>3</sub>O<sub>4</sub> sample (pH 10) reduced with CO or H<sub>2</sub> by dosing 10 L O<sub>2</sub> initially followed by 10 L CO.

---

## LIST OF TABLES

Table 1 UV-vis Spectroscopy peak positions of solutions of different pH of 0.1 mM PdCl<sub>2</sub>.

Table 2 XPS data of Pd 3d and Cl 2p of Pd/Fe<sub>3</sub>O<sub>4</sub> samples prepared using solutions of different pH of PdCl<sub>2</sub>.

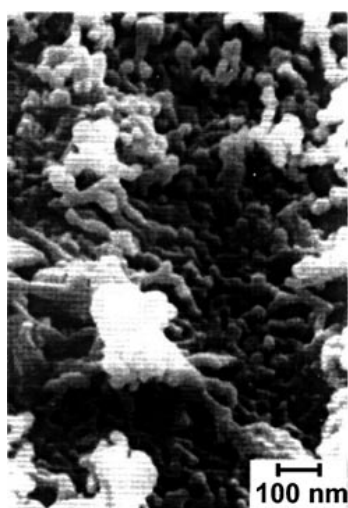
# **Chapter 1**

## **Introduction**

## 1.1 Catalysis and surface science

### Technical catalysis

Heterogeneous catalysis plays an important role in chemical industry. Notable examples are applications in chemicals synthesis, mobile emission control and energy storage and conversion. Although it has been the topic of extensive scientific research during the last decades, the microscopic-level understanding of catalytic processes in technical catalysis is still limited. This is partly because of the chemical and structural complexity of catalytic materials (catalysts), and of the reaction systems. The majority of catalysts applied in heterogeneous catalysis are composed of small mono- or bimetallic particles dispersed on a high surface area support. Often, promoters are added, which act to stabilize the catalytically active center or to enhance catalytic activity by influencing its electronic properties. The complexity can be clearly seen with the example of an industrial ammonia synthesis catalyst shown in Figure 1.1.[1]



Technical conditions:  $T \approx 400^\circ\text{C}$ ,  $p \approx 300$  bar  
promoted iron catalyst

#### BASF S6-10 catalyst [at. %]

	Fe	K	Al	Ca	O
Bulk composition	40.5	0.35	2.0	1.7	53.2
Surface –					
unreduced	8.6	36.2	10.7	4.7	40.0
reduced	11.0	27.0	17.0	4.0	41.0
cat. active spot	30.1	29.0	6.7	1.0	33.2

Fig. 1.1. Surface topography and chemical composition of an industrial ammonia synthesis catalyst.[1]

Surface topography displayed by electron microscopy shows the complex surface structure with iron oxide particles dispersed on a rough support. Under reaction conditions, the particles are reduced to metallic iron and are covered by submonolayer quantities of potassium (+O), which acts as an “electronic” promoter. The high particle dispersion is achieved and maintained during reaction by the oxide supports ( $\text{Al}_2\text{O}_3$  and  $\text{CaO}$ ), which act as “structural”

promoters. The catalytically active phase exposes different surface planes (facets) and exhibits various types of defects. Both structure and composition affect the performance of the catalyst and need to be optimized, most often on an empirical basis, to achieve high product yields and, at the same time, to maintain long-term operation.

The other type of complexity in technical catalysis arises from processes happening on the catalyst surfaces. Reaction processes include multiple reactants, different reaction pathways, many intermediates and complex products. In terms of reaction kinetics, they are related with activity, selectivity and stability. The complexity of catalytic materials and reaction systems makes correlations between activity and structure difficult to obtain.

### Model systems

In order to gain a comprehensive understanding of heterogeneous catalysis, different model systems have been designed (Figure 1.2) with the aim to capture the essential parts of the catalytic system, while being simple enough to allow for detailed conclusions.[2] The first simplification of complex technical catalyst materials is to exclude all promoters and apply only monometallic catalyst on a porous support. The next step towards a model system is to replace a porous support by a spherical one. With the objective to apply surface science techniques, flat supports, either single crystals or thin film, can be used. The simplest model is the unsupported single crystal.

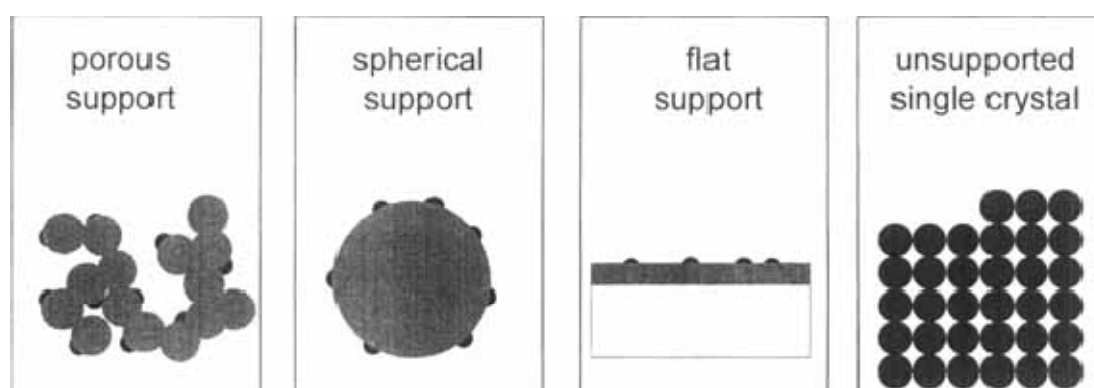


Fig. 1.2. Several possibilities for modeling catalysts exist between the industrial system with a high surface area, porous support (left) and the surface of a single crystal (right).[2]

Surface science investigations using atomically flat surfaces of metal single crystals in ultrahigh vacuum (UHV) have yielded valuable atomic scale information of elementary

processes occurring on a catalytic surface.[3, 4] Among them, the structure sensitivity of catalytic reactions and the role of surface defects in surface reactions have been extensively studied. The measurement of reaction rates has been conveniently made at a low pressure ( $10^7 - 10^{-4}$  Pa). In order to approach more realistic conditions, efforts have been taken in recent years to develop techniques that allow the single-crystalline surfaces to be investigated under more relevant pressure conditions (mbar range, “bridging the pressure gap”) [5-14]. These techniques include high pressure-STM, high pressure-XPS, high pressure-PMIRAS and high pressure-SFG.

In order to include the effect of particle size and support on the properties of supported catalyst in the real system, the surface science approach has been extended to model system consisting of small metal particles supported on planar oxide supports (“bridging the materials gap”) [2, 15-27]. Planar oxide supports used in surface science studies of supported metal catalysts include oxide bulk single-crystals (e.g.  $\text{TiO}_2$ ) [28], amorphous oxide films (e.g. a thin silica layer on a Si single crystal surface) [29] and single-crystalline thin oxide films supported on conductive metal substrates [30]. With conductive thin oxide films, UHV based surface science techniques, which use electrons or ions as information carriers, can be applied in a similar way as for single crystal metal systems.

Beside the pressure and materials gaps, a third gap regarding the preparation of supported metal catalysts appears to exist. While the deposition of metal particles onto flat oxide supports is typically achieved by physical vapor deposition (PVD) in UHV, almost all supported catalysts used in industry are prepared by wet chemical methods with the important processes occurring at the solid-liquid interface. The major difference between the two approaches is the nature of the precursor and the way it is transformed into a particle. Concerns may be raised over how well the properties of samples created via simplified UHV procedures represent those of samples produced via technically applied wet chemical procedures. A combination of surface science methodologies and realistic catalyst preparation procedures is, therefore, highly desirable, but has been implemented only by a few research groups in the past [29, 31-36].

## 1.2 Supported catalyst preparation and characterization

### Technical catalysts

Catalyst preparation is one of the most important steps in a catalysts life cycle and many different preparation methods have been developed according to the demands of the special

catalytic materials used for specific chemical reactions to be catalyzed. Generally, when applying wet chemical methods, the preparation procedure is composed of four steps (Figure 1.3: steps 1, 3, 4 and 5): (1) contact of a support with a solution containing the precursor complex, (3) drying at low temperatures (20-100 °C), (4) calcination at high temperatures (usually 300-600 °C), (5) activation in catalytic reactors by reduction in H<sub>2</sub> to produce metallic catalysts, or sulfidation in H<sub>2</sub>S to produce sulfided catalyst. For oxidic catalysts, the activation step (5) can be omitted.

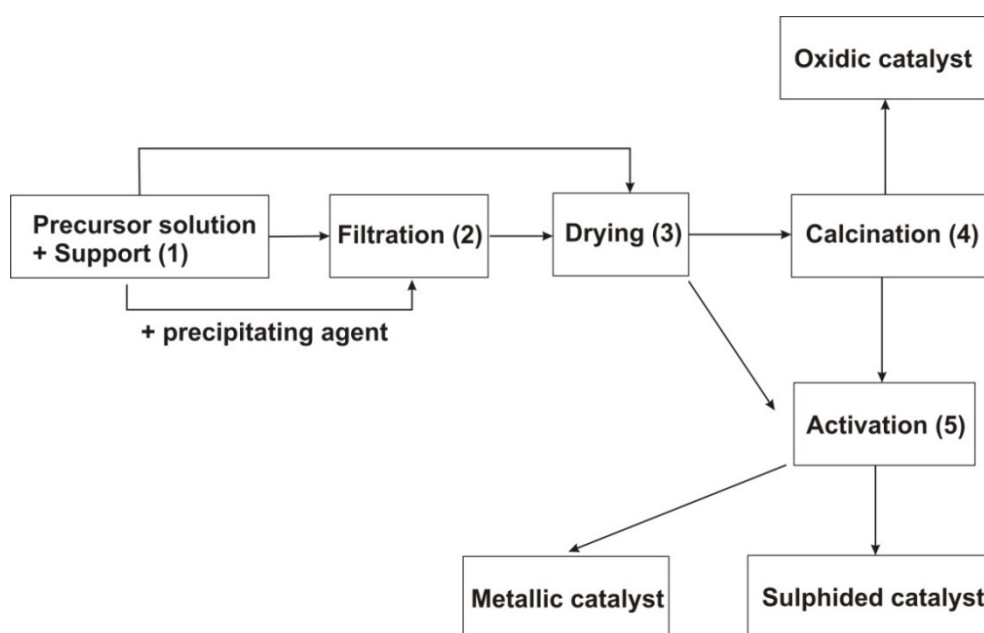


Fig. 1.3. General preparation scheme of supported catalysts. Modified from reference [37].

The introduction of precursor complexes onto the support can be achieved by several ways: (1) One commonly used method is impregnation, which involves the deposition of a precursor from aqueous solution onto a support. When the volume of the impregnating solution is equal to the pore volume of the support, the technique is called incipient wetness impregnation or dry impregnation. No washing step is included in the impregnation method. Impregnation is often used to prepare supported noble metal catalyst such as Pt and Pd. (2) In deposition-precipitation, a precursor is precipitated onto the support from a large volume of solution. A filtration step (step 2 in Figure 1.3) is followed to separate precipitates from solution. This preparation procedure was originally developed to obtain high loadings of catalyst precursor finely distributed on the support surface. (3) In coprecipitation, the catalyst precursor and the support are simultaneously precipitated from solution. (4) Ion-exchange involves the exchange of ions bound to the support surface by ionic precursor species. This method is

commonly used for the preparation of zeolite-supported catalysts. The first two methods mentioned here will be further discussed in Chapter 3.

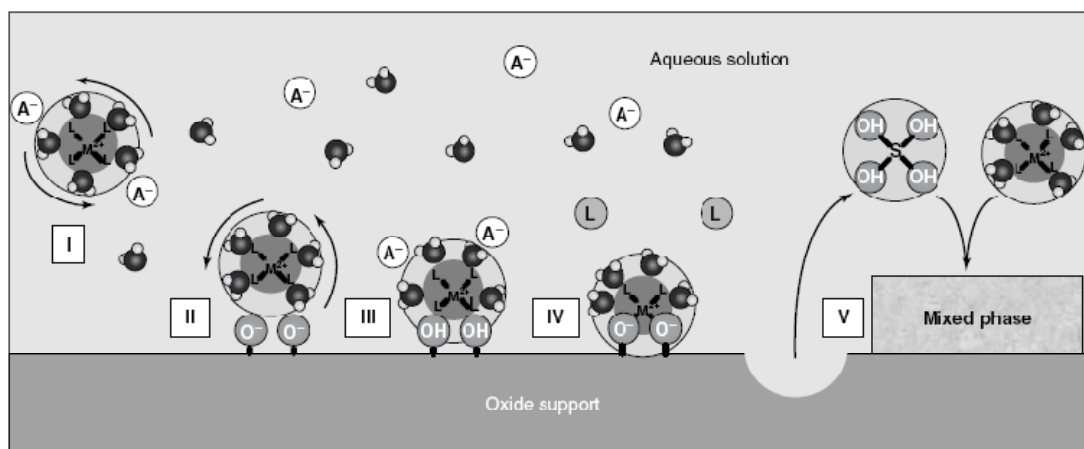


Fig. 1.4. Interaction models between a transition metal ion (TMI) of a precursor complex and an oxide support.[38]

Microscopically, different types of interaction between precursor complex and the support surface are possible. Figure 1.4 shows interaction models between a transition metal ion (TMI) of a precursor complex and an oxide support as proposed by M. Che et al.[38] After diffusion from the bulk of the solution to the interface, aqueous precursor complexes may maintain their original coordination sphere (model I) and interact with the surface just by weak electrostatic adsorption (model II). If some of the coordinated water molecules are lost during interaction, the ligands may directly interact with surface OH groups, leading to stronger interaction between precursor complex and surface (model III). A chemical bonding between precursor complex and support can be established when the ligands and surface OH groups are involved in condensation (model IV, the metal center directly forms chemical bonds with the support; this is usually called “grafting”). In particular cases, support dissolution may occur and dissolved support may interact with TMI to form a mixed phase (model V). The solution pH, type of ligands and the properties of the support strongly influence the adsorption mode and, consequently, the structure, composition and particle size of the final catalyst. For example, it was found that the final structure of a Pt catalysts prepared from chloroplatinic acid strongly depends on the nature of the initial interaction with the support. When the adsorption mechanism is electrostatic and / or outer sphere, such as on silica, self-reduction of the adsorbed chloroplatinic complex to metallic Pt occurs even under an oxidizing atmosphere and results in a low dispersion of Pt particles.[39] On the other hand, when the chloroplatinates are adsorbed by an inner sphere mechanism such as on  $\gamma$ -alumina, the grafted

[Al(OH)<sub>2</sub>Pt<sup>IV</sup>Cl<sub>4</sub>] species are inert to self-reduction. The adsorbed complex can only be reduced to metallic Pt by H<sub>2</sub> reduction and then Pt particles with high dispersion are produced.[39]

Because of the complexity of the materials involved, the development of industrial catalysts is in most cases based purely on technical know-how. However, increasing efforts were put in recent years into studies addressing the fundamental understanding of the early stages of the catalyst preparation process. Spectroscopic techniques such as Extended X-ray Absorption Fine Structure (EXAFS), Nuclear magnetic resonance (NMR) and UV-Visible have been applied to study the adsorption of transition metal precursor complexes from the liquid phase onto oxide surfaces, and the pH dependent speciation of metal precursors, various adsorption mechanisms and the local structure of adsorbed species, have been investigated.[40-42] Even less is known about the phenomena that occur during the later stages of catalyst preparation such as calcination and reduction. A very recent review has summarized the current state of studying kinetics and mechanisms of formation of supported nanoparticles from adsorbed precursor.[43] Although powerful in situ techniques like XAFS, total high-energy X-ray scattering plus PDF analysis, IR spectroscopy, or electron microscopy have been applied to characterize the supported-nanoparticles at the gas-solid interface, “rational, mechanistically guided synthesis of the desired size, structure and compositionally controlled supported-nanoparticle catalysts are generally still lacking”, as mentioned in that review [43].

### **Model catalyst in UHV**

Model studies of catalysis carried out in UHV environment take advantage of morphologically much simpler materials and the possibility of applying a wide range of analytical techniques that can provide atomic scale information of surface processes. One particular attractive surface science approach is the preparation of model catalysts consisting of metal nanoparticles deposited on a single-crystalline oxide film that is grown on a conductive metal substrate. Figure 1.5 shows the sequence of steps involved in the preparation of a thin film model catalyst system both in a schematic fashion (Figure 1.5a) as well as with the preparation of MgO-supported Au clusters as a practical example (Figure 1.5b).

A traditional approach for the preparation of thin oxide thin films is the oxidation of the native metal. One problem encountered with this method is that disordered (amorphous or polycrystalline) structures or films with high defect density are easily formed. In addition, the thickness of the film is difficult to control during various treatments because of diffusion of

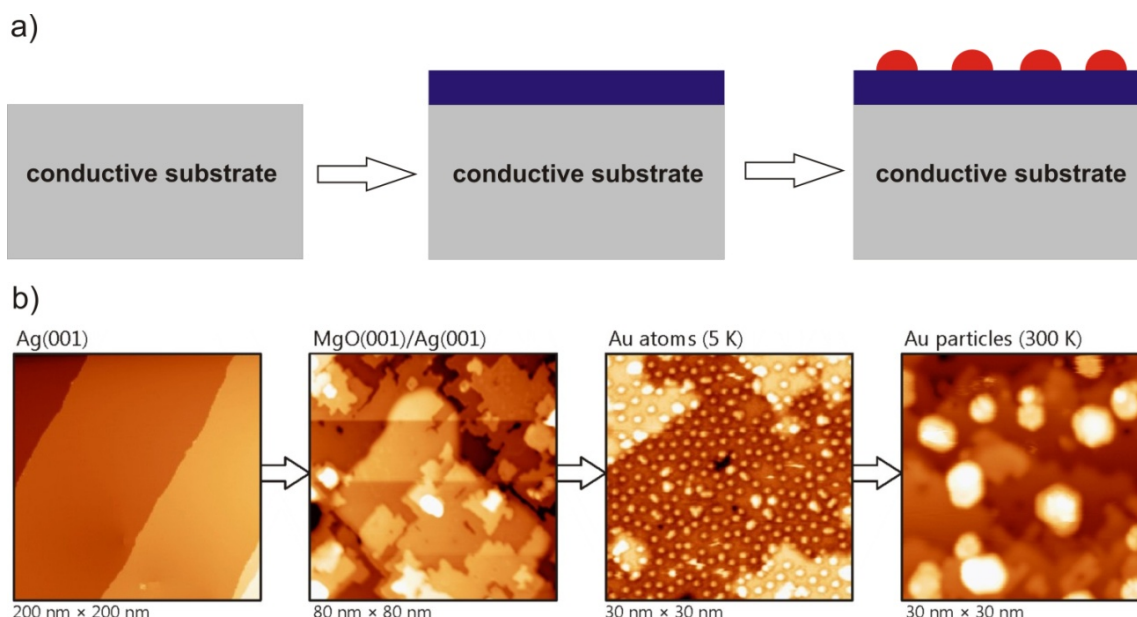


Fig. 1.5. (a) Schematic illustration of model supported catalyst consists of supported metal particles and thin oxide film grown on conducting substrate. (b) STM images of Ag(001) single crystal, thin film of 8 ML MgO(001) supported on single crystal Ag(001), Au atoms deposited on MgO film at 5 K in UHV and 3D Au particles formed after annealing at 300 K.[44]

reactive gases, for example oxygen or NO, into the bulk metal phase [45]. Another approach is the oxidation of a suitable alloy that contains the metal which should be oxidized. One most successful example is the thin alumina film preparation by oxidation of the NiAl(110) alloy [46, 47]. The most popular approach nowadays is the oxide film preparation by evaporation of the desired metal onto a suitable single-crystal metal in oxidizing atmosphere. This method has been successfully used to prepare many single crystalline oxide films such as SiO<sub>2</sub> [48-51], MgO [52-54], iron oxide [55], CeO<sub>2</sub> [56-58], vanadium oxide [59-61], CaO [62], or TiO<sub>2</sub> [63-65].

The most convenient and clean method for the creation of supported metal nanoparticles in UHV is physical vapor deposition. The processes during metal nanoparticle formation of single crystalline oxide substrates, including initial interaction of gas phase metal atoms with the surface, diffusion, nucleation (homogeneous or heterogeneous), and agglomeration and growth, have been studied in detail and are documented in many review papers [19-21, 66].

### Model approaches to catalyst preparation

Apart from PVD, many other methods have been developed to prepare model supported

catalyst, for example, chemical vapor deposition (CVD), deposition of mass-selected clusters, immobilization of colloidal nanoparticles, lithography, atomic layer deposition (ALD).[2] An alternative way to deposit metal onto flat model supports is to apply a catalyst precursor by wet chemical methods, followed by drying, calcinations and reduction to transform the adsorbed metal precursor complex into metal nanoparticles. This approach brings the model catalyst study very close to the industrial catalyst preparation practice. The earliest report about supported model catalyst preparation from liquid phase was given by Ertl and coworkers in 1989 [67]. This work was about the preparation of vanadia supported on a thin TiO<sub>2</sub> film via impregnation. The system was characterized by XPS and temperature programmed desorption (TPD). Later on, a lot of work related to noble metal deposition on carbon materials via wet chemical method has been done by the groups of Wolf [68, 69] and Baiker [70, 71]. Using TiO<sub>2</sub> single crystals and single-crystal fragments as supports, Haruta [35] and Goodman [72] studied Au deposition by deposition precipitation or solution-deposition of phosphine-stabilized gold clusters. Since 1991, Niemantsverdriet and coworkers [29, 31-33] have investigated supported catalyst preparation on silica and alumina thin films by impregnation and spin coating methods to mimic pore volume impregnation. Various surface science tools such as XPS, Auger Electron Spectroscopy (AES), secondary ion mass spectrometry (SIMS), low energy ion scattering (LEIS), atomic force microscopy (AFM) have been applied to characterize the resulting catalysts. It has to be mentioned that amorphous substrate material was used in the latter studies and that a combined morphological (microscopic) and chemical (spectroscopic) characterization of the catalyst preparation steps has not been reported in the previous attempts to prepare model catalyst by applying technically relevant preparation procedures.

### 1.3 Motivation of our work

In this work, we take advantage of the ability to prepare conductive, single crystalline thin oxide films on single-crystal metal substrates in UHV and utilize them as supports for studying metal deposition following wet chemical methods. This “Surface science approach to supported metal catalyst preparation” allows surface science techniques to be applied and both morphological and chemical information of the relevant steps of a realistic catalyst preparation procedure to be obtained. The aim of this work is to demonstrate that this surface science approach is capable of providing new insights into catalyst preparation and, in particular, to shed light onto the initial stages of catalyst preparation. In addition, comparison

of wet chemical methods and conventional UHV based methods of supported metal nanoparticle preparation promises to highlight the similarities and differences of the two methods with respect to the properties of the resulting nanoparticles.

As a prototype system, a  $\text{Fe}_3\text{O}_4(111)$  thin film grown on  $\text{Pt}(111)$  was chosen as substrate for Pd nanoparticles prepared by decomposition of precursor complexes adsorbed from aqueous solutions. In this thesis, scanning tunneling microscopy and X-ray photoelectron spectroscopy were applied to track the morphological and chemical changes that come along with the transformation of adsorbed Pd precursors into nanoparticles during thermal reduction. In addition, temperature programmed desorption and infrared spectroscopy were used to obtain relevant information concerning the chemisorption properties of the resulting Pd nanoparticles after different activation procedures.

## 1.4 Outline of this thesis

The present thesis is organized as follows.

- Chapter 2 presents the experimental part. The experimental set-up, in particular the UHV-to-liquid transfer system and the liquid cell, is described. The basic theory of the surface science techniques used in this thesis and the working principles of related instruments are introduced and the application of these techniques in catalyst studies is discussed.
- Chapter 3 is dedicated to details about catalyst preparation. In particular, the speciation of the  $\text{PdCl}_2$  precursor at different solution pH is discussed and the two frequently used catalyst preparation methods, impregnation and deposition-precipitation, are described in detail.
- Chapter 4 is concerned with the surface properties of the  $\text{FeO}(111)$  and  $\text{Fe}_3\text{O}_4(111)$  films under non-UHV conditions. The properties of  $\text{FeO}(111)$  and  $\text{Fe}_3\text{O}_4(111)$  are firstly reviewed. Results of STM investigations related to the stability of  $\text{FeO}(111)$  and  $\text{Fe}_3\text{O}_4(111)$  film in non-UHV conditions (air, water, acidic and basic solution, and after subsequent thermal treatment in UHV) are presented.
- Chapter 5 focuses on studying the early stages of Pd catalyst preparation, from adsorption of Pd precursor complex to thermal reduction of the precursor and creation of Pd nanoparticles. In particular, the different nucleation behavior of Pd nanoparticles prepared either by impregnation or by deposition-precipitation is explained and the

---

effect of chlorine residue is described. This chapter contains also a comparison of wet chemical and UHV-model approaches of supported catalyst preparation.

- Chapter 6 describes the chemical changes induced in the wet chemically prepared Pd/Fe<sub>3</sub>O<sub>4</sub> model catalyst induced by different activation procedures. Chemisorption of CO, O<sub>2</sub> and H<sub>2</sub> molecules on Pd is briefly reviewed. Then, CO chemisorption properties of the activated wet-prepared Pd catalyst are compared with physical vapor deposited Pd on the same Fe<sub>3</sub>O<sub>4</sub> support. H<sub>2</sub> reduction of the Pd/Fe<sub>3</sub>O<sub>4</sub> system is shown to induce strong metal support interaction (SMSI) and the mechanism of SMSI is discussed. Finally, results for CO oxidation on the prepared Pd catalyst are presented.
- Chapter 7 summarizes the most important results of this thesis. The future direction of the research is also suggested.

# **Chapter 2**

## **Experimental set-up and techniques**

## 2.1 Set-up

### 2.1.1 UHV chamber and liquid-STM

The experimental set-up consists of a UHV chamber equipped with a sputter gun, a metal evaporator, a low energy electron diffraction (LEED) apparatus and an X-ray photoelectron spectroscopy (XPS) system for single crystal cleaning, preparation and characterization, and a quadrupole mass spectrometer (QMS) for temperature-programmed desorption (TPD) experiments. Another UHV system with an infrared spectrometer was used for Infrared reflection absorption spectroscopy (IRAS) measurements. XPS spectra were acquired in UHV using an Al K $\alpha$  X-ray source and a hemispherical analyzer (SPECS Phoibos 150) with the pass energy set to 20 eV. For the TPD experiments, the sample surface was placed less than 1 mm in front of the nozzle of the shield to minimize the signal coming from the background. 10 L  $^{13}\text{CO}$  was dosed at 300 K before taking measurement. The sample was heated with a heating rate of 3 K/s. IRAS spectra were acquired with a UHV FT-IR spectrometer (Bruker IFS 66 v/s) and a MCT detector and the resolution was set to 4  $\text{cm}^{-1}$  resolution. The sample was held at 80 K during measurement.

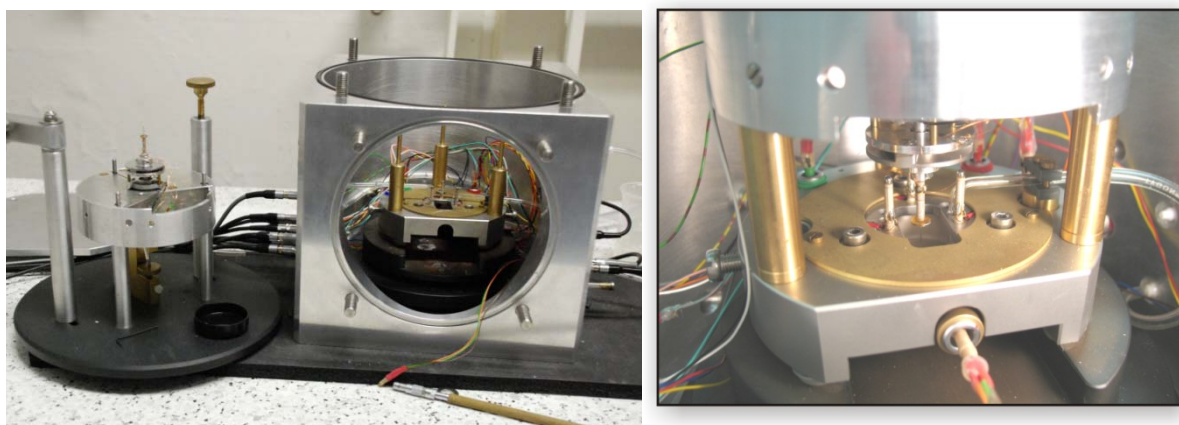


Fig. 2.1. The picture of the liquid-STM including scanner head, tip adjusting device, aluminum chamber and damping stage.

Scanning tunneling microscopy (STM) is a Wandelt-type electrochemical STM working in air and liquid conditions [73]. The STM chamber with scanner head, support and liquid cell inside sitting on a damping stage is shown in Figure 2.1. A Pt (90%)/Ir (10%) wire (0.25 mm diameter) was used as tip material and the STM tips were prepared by electrochemical etching. The etching solution is composed of 1 M KOH and 2 M KSCN. The etching is realized using

a square wave function with amplitude of 10 V supplied by a DDS Function Generator (VOLTcraft FG708S). When STM is operated in aqueous solution, the tip should be coated to avoid the influence of the faraday current. The tip was coated with PE materials which were heated to 150 Celsius degree. STM images were taken in the constant current mode controlled by a feedback loop.

### 2.1.2 UHV-to-liquid transfer system

To perform liquid study, a UHV-to-liquid transfer system has been designed. As shown in Figure 2.2, there are two transfer chambers which are separated by a gate valve. These two chambers are in vacuum condition before transfer. The sample prepared in the main UHV preparation chamber (above first transfer chamber) is firstly transferred to the sample holder on the transfer rod located in the first transfer chamber (the right one) by the main manipulator in the UHV chamber. Then the first transfer chamber is isolated from the preparation chamber and the two transfer chambers are vented with inert gas (e.g. Ar) to the same pressure of 1 bar. The sample is then transferred with the help of the transfer rod from the first transfer chamber into the second transfer chamber. The left image in Figure 2.2 shows details of the second transfer chamber (we can also call it liquid chamber). A liquid cell with a sample support underneath is located in the liquid chamber. The sample on the transfer rod is firstly placed in the sample support and then the liquid cell is fixed from the top. Then, the sample surface is pushed against the bottom of the liquid cell by moving the bottom

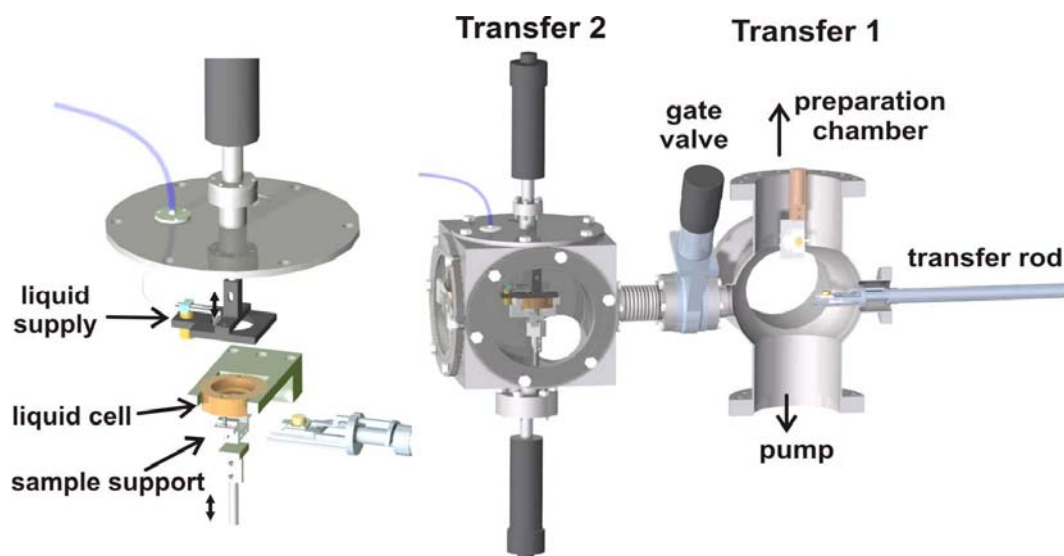


Fig. 2.2. Schematic illustration of the UHV-to-liquid transfer system.

support stage. Liquid can be introduced into the cell under the inert gas (e.g. Ar) protection through the liquid supply. Once the sample is in contact with the liquid, it is taken out of the chamber and transferred to the STM chamber through air.

### 2.1.3 Sample holder and liquid cell

The requirements for the sample holder are that sample needs to fit into the liquid cell for STM experiments and needs to have the capability of a fast transfer between UHV and liquid environment. The holder design is based on the Omicron standard sample plate. The structure of the sample holder is shown in Figure 2.3 (top). All the components are constructed on a molybdenum base plate with a big hole in the center and four small holes in the corners. A sapphire isolation plate is located between the sample and the Mo plate for electrical isolation. Thermocouple wires are twined on the isolation plate and then connected to the sample. The sample is fixed on the sample holder by two Mo foils. There are two Mo bars at the rear side of the holder, one for filament current connection and another one for high voltage connection. Sample heating is achieved by electron beam heating. The sample transfer in UHV between transfer head and manipulator is shown in Figure 2.2.

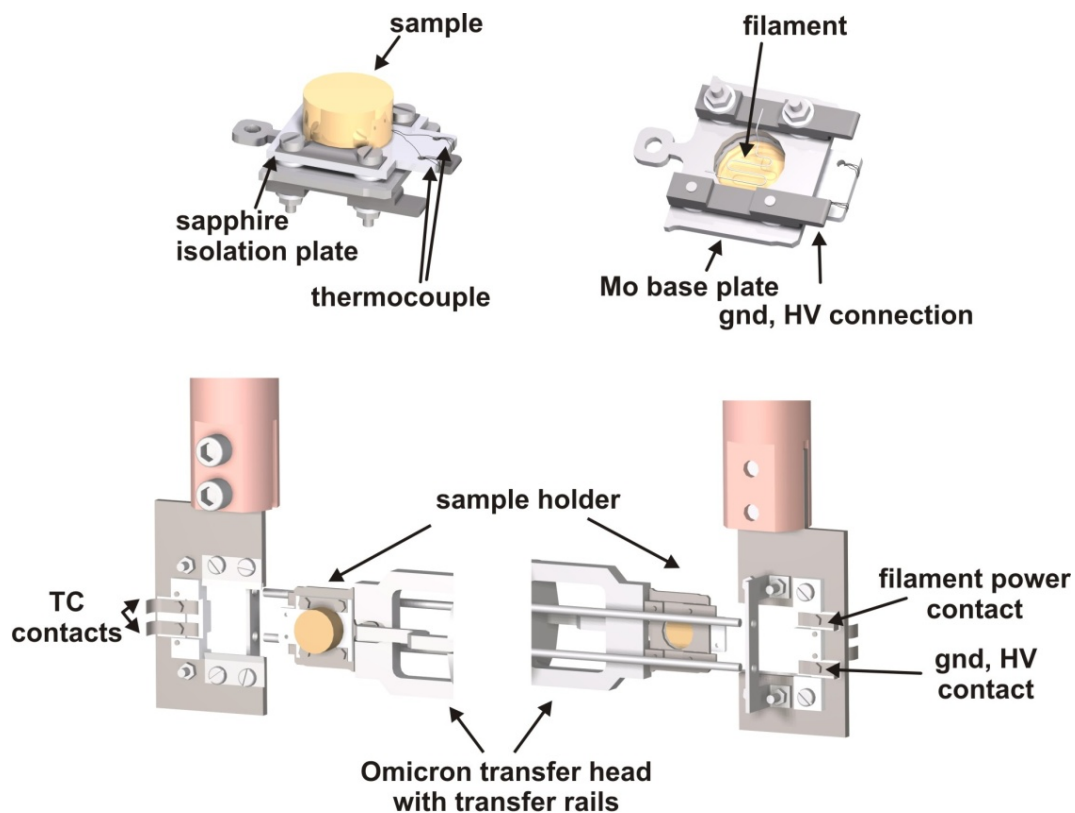


Fig.2.3 Sample holder (top) and UHV sample transfer (bottom).

The liquid cell is made of PEEK which is acid and basic resistant. The maximum volume is 4 ml. A scheme of the cell is shown in Figure 2.3. Two holes at the edge of cell are used for fixing the sample holder. The other three holes are for fixing the cell in the STM chamber. When the sample is mounted in the cell, a Kalrez® sealing O ring with 6 mm diameter is used to avoid leakage of liquid. The thickness of sample crystals is required to be 5 mm.

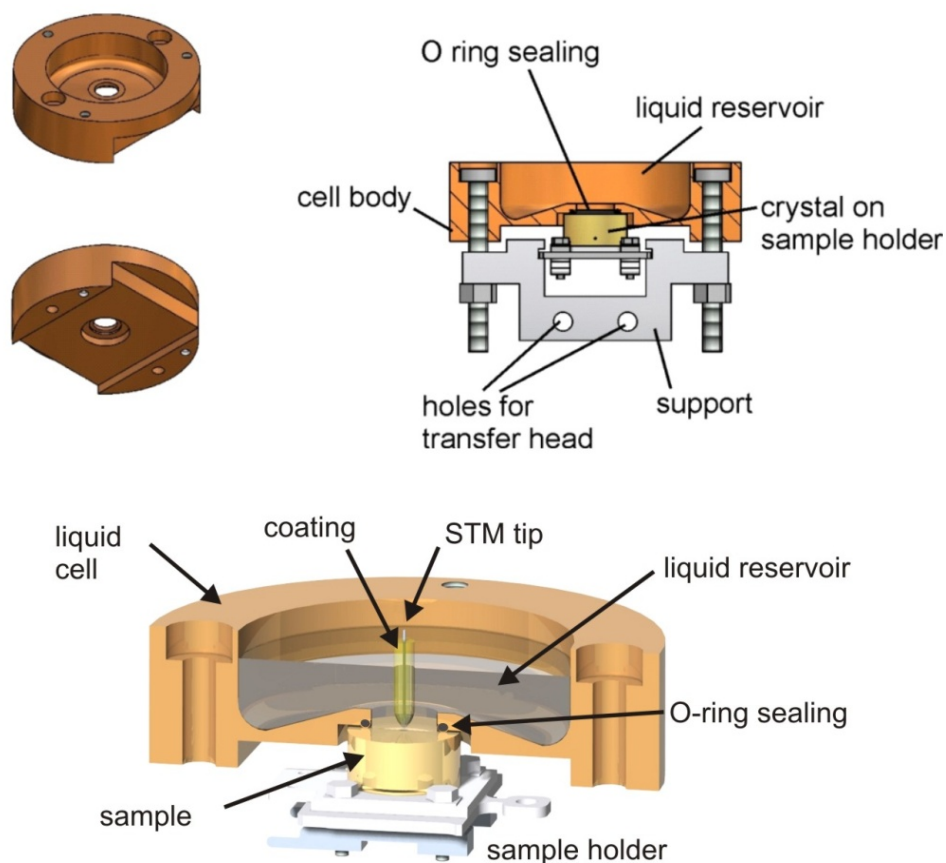


Fig. 2.4 Scheme of liquid cell and its state in liquid STM chamber.

## 2.2 Surface science techniques

### 2.2.1 Scanning Tunneling Microscopy (STM)

#### *Theoretical aspects*

The STM is based on the concept of quantum tunneling which is in the domain of quantum mechanics. A particle can tunnel through a barrier, which cannot happen in classic mechanics. The difference comes from that the small particle in quantum mechanics has the property of wave-particle duality. In the one-dimensional case, the elastic tunneling of an electron of energy  $E$  through a constant potential barrier  $U$  can be described by a stationary Schrödinger equation:

$$\left(\frac{-\hbar^2}{2m} \frac{\partial^2}{\partial z^2} + U\right) \cdot \psi(z) = E \cdot \psi(z) \quad (2.1)$$

The solution is

$$\psi(z) = \psi(0)e^{-kz} \quad (2.2)$$

where

$$k = \frac{\sqrt{2m(U-E)}}{\hbar} \quad (2.3)$$

$\psi(0)$  is the wave function of the surface state of the sample at  $z=0$ . As seen from equation (2.2), the wave function  $\psi(z)$  decays exponentially with the distance  $z$ . The tunneling probability is equal to the square of wave function after the barrier:

$$|\psi(z)|^2 = |\psi(0)|^2 \exp(-2kz) \quad (2.4)$$

Mathematically the tunneling current can be expressed as the sum of all participating states:

$$I \propto V \sum_{E_n = E_F - eV}^{E_F} |\psi(0)|^2 \exp(-2kz) \quad (2.5)$$

where  $V$  is the bias voltage applied between two electrodes. The sum over of all states is equal to local density of states in the sample, so the tunneling current can be expressed as:

$$I \propto V \rho_{sample}(E_F) \exp(-2kz) \quad (2.6)$$

The tunnel signal contains information about the barrier height (sample topography) and the local density of states (LDOS) in the sample. A schematic drawing of a one-dimensional Tip-Vacuum-Sample tunneling junction in STM is shown in Figure 2.5. Electron tunneling can occur from the metal tip to the sample surface, or vice versa, depending on the direction of the bias.

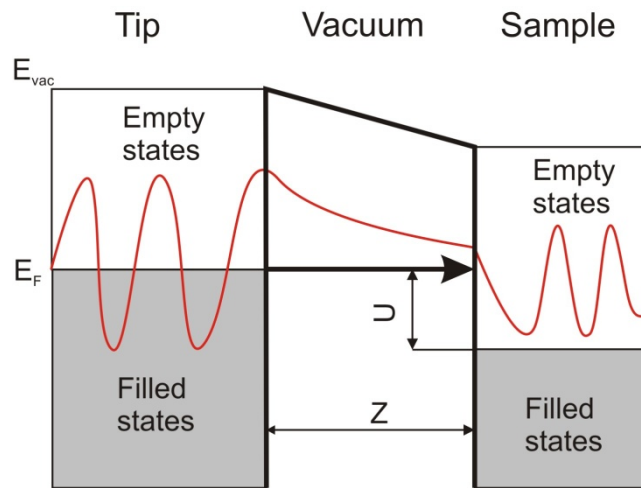


Fig. 2.5. Potential energy diagram of the tunneling process. Tunneling from the filled states in tip into empty states in the sample occurs when a negative bias voltage is applied to the tip.

The approach shown above, however, cannot adequately describe the real experimental situation because it considers only a one-dimensional case and does not include important parameters such as the electronic states in the tip and the sample, the geometry of the tip or the presence of inelastic tunnel processes. Several kinds of models have been developed to account for those parameters and one widely used approach is that described by Bardeen.[74] In his approach, the wave functions of the two separated electrodes are supposed to be independent. The transition probability from an initial state  $|i\rangle$  on one electrode to a final state  $|f\rangle$  on the other is calculated using time dependent perturbation theory. The transition probability obeys Fermi's golden rule:

$$W_{i,f} = \frac{2\pi}{\hbar} |M_{i,f}|^2 \delta(E_i - E_F) \quad (2.7)$$

where  $M_{i,f}$  is the transition matrix:

$$M_{i,f} = -\frac{\hbar^2}{2m} \int (\psi_f^* \nabla \psi_i - \psi_i \nabla \psi_f^*) dS \quad (2.8)$$

The integration is done over a surface  $S$  between the tip and the sample electrode.  $\psi_i$  and  $\psi_f$  are the wave functions of initial and final states in tip and sample. With the assumption of small voltages and a temperature of 0 K, where the Fermi-Dirac distribution  $f(E)$  is a step function, the tunnel current is expressed by:

$$I = \frac{2\pi}{\hbar} e^2 V \sum_{i,f} |M_{i,f}|^2 \delta(E_i - E_F) \delta(E_f - E_F) \quad (2.9)$$

with the bias voltage  $V$ , the energy of the initial state  $E_i$  and final state  $E_f$ , the Fermi energy  $E_F$  and the Dirac's delta function  $\delta(E)$ .

Tersoff and Hamann [75] have further developed the theory of STM based on the approach given by Bardeen. Here the three-dimensional case is treated by modeling the STM tip with a spherical potential with only  $s$ -like Eigenfunctions. The tunnel current is proportional to the convolution of the LDOS of the sample at the position of the tip. According to the Wentzel-Kramers-Brillouin (WKB)-approximation, the tunneling current  $I$  is then given by:

$$I \propto \int_{-\infty}^{\infty} \rho_s(E) \rho_t(E - eV) T(d, E, eV) [f(E - eV, T) - f(E, T)] dE \quad (2.10)$$

with  $\rho_s$  and  $\rho_t$  the density of states of sample and tip, and the transition probability  $T$  given by:

$$T = \exp \left( -2d \frac{\sqrt{2m}}{\hbar} \sqrt{\frac{\Phi_s + \Phi_t}{2} + \frac{eV}{2} - E} \right) \quad (2.11)$$

which depends on distance  $d$  between the tip and sample, the work functions of tip  $\Phi_t$  and sample  $\Phi_s$  and the bias voltage  $V$ . Following the same assumption mentioned above (small bias and 0 K), formular (2.10) can be simplified to:

$$I \propto \int_0^{eV} \rho_s(E) \rho_t(E - eV) T(d, E, eV) dE \quad (2.12)$$

It means that in the case of the constant current mode, the observed corrugation is the plane of constant integrated LDOS on the sample surface. This is the usual starting point for the interpretation of STM data and it should be noted that the observed topography is a convolution of geometric and electronic contributions. Despite of the success of the Tersoff-Haman model in many experimental situations it is sometimes necessary to take more complex tip wavefunctions into account such as  $P_z$  and  $D_{zz}$  states [76] to achieve an agreement with experimental data.

### *The operation principle*

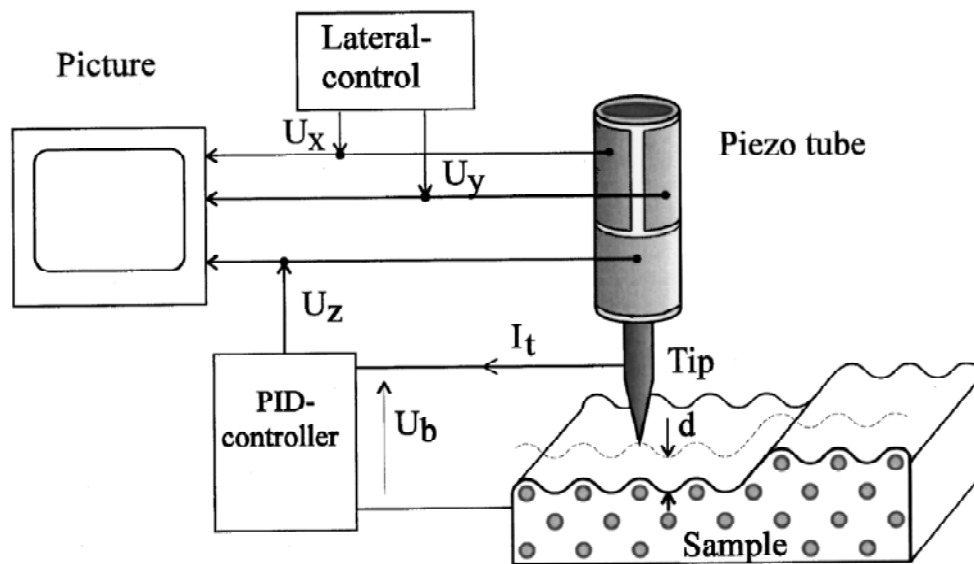


Fig. 2.6. Schematic illustration of the working principle of an STM instrument [77].

The working principle of STM instrument is shown in Figure 2.6 [77]. The heart of STM is a piezoceramic tube with a tip. The lower part of the tube is connected to the height ( $z$ ) signal  $U_z$ . By applying a voltage  $U_z$  between the inner and outer electrodes the piezotube can be lengthened or shortened depending on the sign of  $U_z$ ; this moves the tip along the axis. The upper part of the tube is surrounded by the remaining four equal electrodes. Applying a voltage to one of these makes the tube bend, the direction depending on the sign of the voltage. This effect can be doubled by applying the inverse voltage to the respective opposite electrode. Thus, with an appropriate combination of  $\pm U_z$ ,  $\pm U_x$ ,  $\pm U_y$  the tip can be moved in all possible spatial directions with a single piezotube. While the tip is scanned over the surface, a PID controller receives the tunneling current and controls the tip height  $d$  above the surface in such a way that  $I_t$  remains constant (constant current mode). Thus the signal  $U_z$

(while  $U_b$  is constant) contains information about the corrugation and the charge density of the surface. The computer creates a two or even a three dimensional picture of the scanned surface area in imaging  $U_z$  as a function of  $U_x$ ,  $U_y$ . For an STM, good resolution is considered to be 0.1 nm lateral resolution and 0.01 nm depth resolution.

### ***STM studying solid-liquid interface***

The STM can be used not only in ultra high vacuum but also in air, water, and various other liquid or gas ambient, and at temperatures ranging from near zero Kelvin to a few hundred degrees Celsius. STM in UHV is based on the tip-sample interaction whereas the use of STM in electrolyte solution demands to deal with the more complex tip-electrolyte-sample system. After the first atomic resolution STM study performed in a liquid [78] many problems had to be overcome. For example, by incorporation of an electrochemical cell into the STM setup one has to cope with larger thermal drift. If the volume of the cell is too small, there are many related problems such as the degassing of oxygen, diffusion and the evaporation [73]. However, the increase of the liquid level above the sample surface would require longer tunneling tips which are known to be more unstable. The bias voltage between tip and sample in an electrochemical STM (ECSTM) is restricted to a certain range to avoid large Faraday currents. During last two decades, much progress has been made on ECSTM design and a lot of exciting results have been obtained from the solid-liquid interface by several groups [79-82].

### ***Application in catalysis***

STM is also applied to study processes related to heterogeneous catalysis. It has been applied to resolve adsorbate structures and individual adsorbate signatures in certain cases and to monitor the atomic and molecular dynamics [83]. In addition, adsorbate-induced restructuring and chemical reactions on surfaces have been studied by STM. It has also shown its ability to obtain information about catalytic active sites. Various kinds of STM, especially High Pressure-STM, have been designed to study surface phenomenon occurring under more practical conditions (high pressure, high temperature) in order to approach real-world catalysis. STM is playing a more and more important role in the field of catalysis [84].

### 2.2.2 X-ray Photoelectron Spectroscopy (XPS)

During the mid 1960's Dr. Siegbahn and his research group developed the XPS technique. In 1981, Dr. Siegbahn was awarded the Nobel Prize in Physics for the development of the XPS technique. XPS is also called electron spectroscopy for chemical analysis (ESCA). XPS can provide valuable surface information about elemental identity, chemical state, and surface composition. XPS has many industrial applications including polymer surface modification, catalysis, corrosion, adhesion, thin film coatings, semiconductor and dielectric materials, and electronics packaging.

XPS is based on Einstein's idea about the photoelectric effect which was developed around 1905. Photoelectric effect means that an atom absorbs a photon of energy,  $h\nu$ , and then an electron with binding energy  $E_b$  is emitted with kinetic energy  $E_k$ ,

$$E_k = h\nu - E_b - \phi \quad (2.13)$$

where  $\phi$  is the work function of the spectrometer.

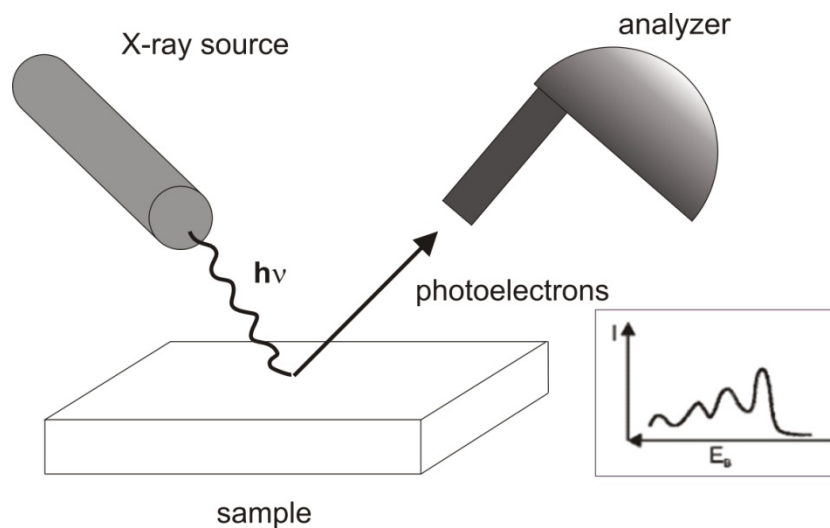


Fig. 2.7. The principle of X-ray photoelectron spectroscopy.

For XPS, soft X-rays are used as photon sources and photoelectrons (core electrons) are detected by an electron energy analyzer (as shown in Figure 2.7). An XPS spectrum is usually a plot of intensities of photoelectrons  $N(E)$  versus  $E_k$ , or more often versus  $E_b$ .

To interpret the experiment, different kinds of theories about photoemission have been developed. Among of them, sudden approximation is widely used. In this theory, it is assumed that the response of the system to the creation of the photohole is instantaneous and there is no interaction between the escaping photoelectron and the remaining system. The photoemission process is also treated by the so-called three-step model which was developed by Berglund and Spicer [85]. In this model, the photoemission process is divided into three steps as shown in Figure 2.8: (1) Photoexcitation of an electron in the solid, (2) transport of the photoelectron to the surface, (3) escape of the photoelectron from the surface to the vacuum. The detailed discussion of photoemission theories can be found in the book written by Hüfner [86] and articles by Hedin [87].

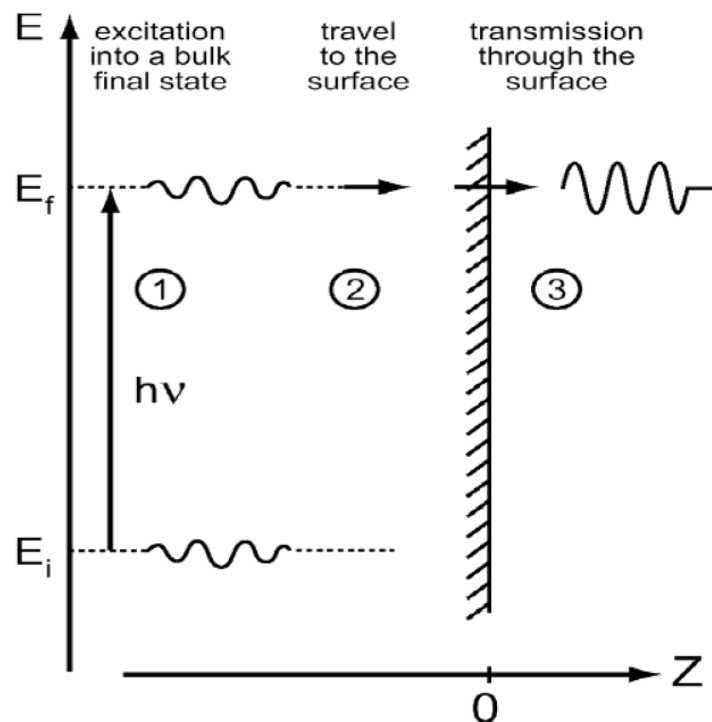


Fig. 2.8. The three-step model of photoemission process [86].

### ***Binding energy***

Binding energies are not only element-specific but also contain chemical information. If the energy of initial state of the atom is changed, for example, change of oxidation state or by formation of chemical bonds with other atoms, then the  $E_B$  of electrons in that atom will change. The change in  $E_B$ , is called the chemical shift. Chemical shifts are typically in the range of 0-3 eV. It is usually assumed that the initial state effects are responsible for the

chemical shift. In general, the binding energy increases with increasing oxidation state, because the attractive force between ionized core and electrons increases.

The  $E_B$  of an emitted photoelectron is simply the energy difference between the  $(n - 1)$ -electron final state and the  $n$ -electron initial state,

$$E_B = E_f(n - 1) - E_i(n) \quad (2.14)$$

The simplest approach to the binding energy calculation comes from Koopmans' theorem [88], i.e. electron orbitals remain frozen during the photoemission process. Then the observed  $E_B$  would be just the negative orbital energy,  $-\varepsilon_k$  for the ejected photoelectron.

$$E_B = -\varepsilon_k \quad (2.15)$$

In reality, during the photoemission process, other electrons in the core-hole containing atom and in the surrounding atoms will try to screen the creation of the core hole by rearrangement to minimize the energy of the ionized atom. Such relaxation effects can have a significant impact on the measured  $E_B$ . In all cases the electron rearrangements that occur during photoemission result in the lowering of  $E_B$ . Other types of final state effects such as shake-up, shake-off, satellites, multiplet splitting and Plasmon loss can also contribute to  $E_B$ . Shake-up and Shake-off arise from the outgoing photoelectron losing part of its kinetic energy to excite a valence electron into an unoccupied orbital (empty state) and unbound state, respectively. The XPS peaks of metals such as Rh and Pt are asymmetrically broadened towards higher binding energies because of shake-up. As the probability of valence band shake-up depends on the density of states at or just above the Fermi level, the effect is most pronounced in d-metals, but is hardly of any significance for s-metals such as Cu, Ag, and Au, all of which give sharp symmetric peaks [89]. Multiplet splitting arises from interaction of the core hole with unpaired electrons in the outer shell orbitals. A well-known example is the splitting of the N 1s and O 1s peaks (normally single lines) in the spectrum of gas phase NO, due to an unpaired spin in the 2p level of the NO molecule [89].

When conducting samples are placed in electrical contact with the spectrometer as shown in the Figure 2.10, the Fermi level of the sample is aligned with that of the spectrometer. The emitted photoelectron from the sample is measured by the spectrometer with kinetic energy equal to  $(h\nu - E_b - \phi_{\text{spec}})$  not  $(h\nu - E_b - \phi_{\text{sample}})$  because the vacuum level of the spectrometer is

different from that of the sample. The spectrometer work function can be calibrated by placing a clean Au standard in the spectrometer and adjusting the instrumental settings such that the known  $E_B$  values for Au are obtained [90]. When working with insulating samples, new problems arise. The Fermi level could be anywhere within the bandgap. Furthermore, photoemission can result in the build-up of positive charge near the surface, resulting in a Volta potential which leads to an apparent shift of binding energies and Auger kinetic energies to higher and lower values, respectively. It is noted also that if the charging is not homogeneous over the surface, peak broadening or the appearance of spurious peaks may also occur. Binding energies measured relative to the Fermi level of the spectrometer then lack validity.

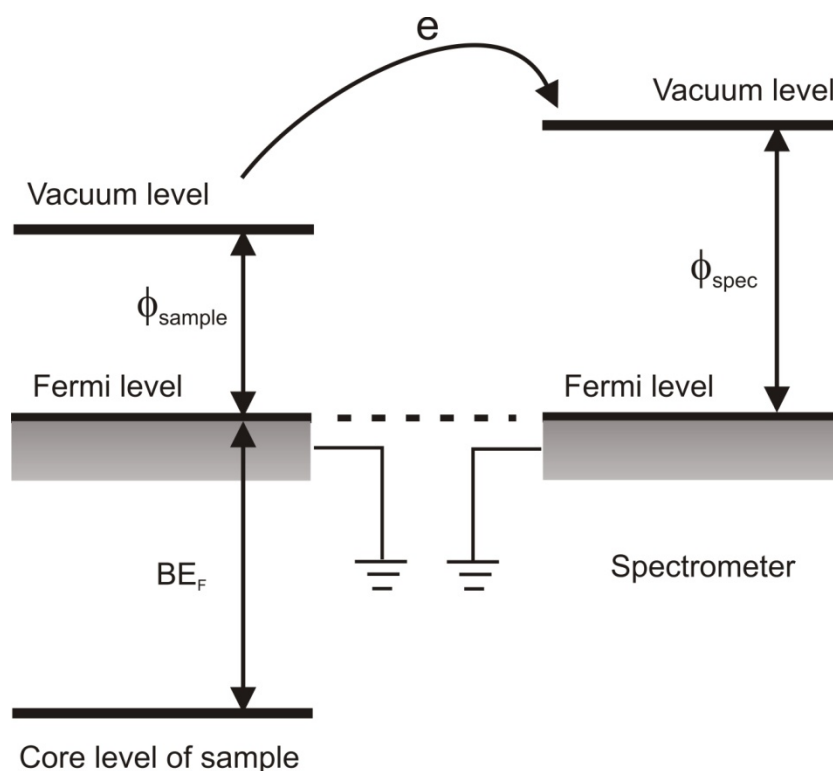


Fig. 2.9. Energy level diagram for the photoemission process.

### *XPS intensity*

The XPS peak intensities (or area under the peaks) are related to the amount of each element present. So, by measuring the peak areas and correcting them for the appropriate instrumental factors, the percentage of each element detected can be determined and finally the sample

composition can be determined. The general expression for the intensity of an XPS peak is [89]:

$$I = F_x S(E_k) \sigma(E_k) \int_0^{\infty} n(z) e^{-z/\lambda(E_k) \cos \theta} dz \quad (2.16)$$

where  $I$  is the intensity of the XPS peak (area),  $F_x$  is the x-ray flux on the sample,  $S(E_k)$  is the transmission function of the spectrometer,  $\sigma(E_k)$  is the cross photoemission,  $n(z)$  is the concentration in number of atoms per unit volume,  $z$  is the depth under the surface,  $\lambda$  is the inelastic mean free path of the photoelectron and  $\theta$  is the take-off angle of the photoelectron. As seen from the above equation, the quantitative analysis of XPS data is complicated. The following parameters need to be known. (1) electron inelastic mean free path, (2) cross section for photoemission, (3) The transmission function of the spectrometer, (4) X-ray flux on the sample, (5) take-off angle. Electron mean free path values are often approximated by calculating them from a general formula. When doing quantitative analysis, the dependence of probing depth on the nature of element must be accounted for. For example, the Al 2p peak in the spectrum of the Rh/Al<sub>2</sub>O<sub>3</sub> catalyst probes deeper into the sample than the O 1s peak [89]. The cross-section  $\sigma$  for photoemission is the probability that the incident X-ray will create a photoelectron from the core level of the atom. The transition obeys the Fermi's golden rule. The emission rate is proportional to the square of the matrix element  $\langle \Psi_f | H' | \Psi_i \rangle$  where  $\langle \Psi_f |$  and  $|\Psi_i \rangle$  are the wave functions of the final and initial states respectively, and  $H'$  is the perturbation Hamiltonian. The cross section can be written as:

$$\sigma \propto |\langle \psi_f | H' | \psi_i \rangle|^2 \delta(E_f^{N-1} + E_k - E_i^N - h\nu) \quad (2.17)$$

Values for  $\sigma$  are typically taken from the calculations of Scofield. As a rule of thumb, the cross section for a given initial state, e.g. the 1s electron, increases very rapidly with the atomic number of the element. This means it is easier to see a contamination of oxygen than a contamination of carbon when looking at a conventional XPS spectrum from a surface [90].

### ***XPS peak width and broadening***

The shape of XPS peak can be affected by different sources, the most important contributions being the natural lifetime and the Gaussian broadening (instrumental resolution and

satellite features, i.e. the vibrational and inhomogeneous broadening.).

### *Life time broadening*

The peak width due to the core-hole lifetime (intrinsic width) is determined by Heisenberg's uncertainty relationship. The lifetime of the core hole ( $\tau$ ) is of the order of some femto seconds, yielding a natural width of 100-200 meV. This broadening, always present in any photoemission spectrum, is described with a Lorentzian distribution. For a given element the value of  $\Delta E$  is typically larger for inner shell orbitals than for outer shell orbitals. This is because an inner shell core hole can be filled by electrons from the outer shells. Therefore, the deeper the orbital, the shorter the core hole lifetime and the larger the intrinsic peak width. Similarly, the value of  $\Delta E$  for a given orbital (e.g. 1s) increases as the atomic number of the element increases, since the valence electron density, and therefore the probability of filling the core hole, increases with increasing atomic number.

### *Gaussian broadening*

The Gaussian broadening of a core level photoemission peak is mainly given by three contributions namely, the inhomogeneous broadening, the vibrational broadening and the experimental energy resolution. The inhomogeneous broadening is due to the superposition of lines with different chemical or structural shifts. The vibrational broadening, in molecules or solids, is given by the excitation of low energy vibrational modes in the final state. For solids, while multiple phononic losses end up in the low kinetic energy region of the so-called true secondary electrons, the intrinsic phonons induce a broadening of the photoemission peaks which can, in most cases, be described by a Gaussian distribution [91]. Instrumental effects include the line width of the incident X-rays and the resolution of the analyzer. The former can be reduced to better than about 0.3 eV with the use of a monochromator, and the latter can be improved by using low pass energy.

### *Surface sensitivity*

XPS is a surface sensitive technique. The surface sensitivity is determined by the electron inelastic mean free path ( $\lambda$ ), emission angle and nature of materials. The attenuation of photoelectron from the sample can be expressed by Beer's law:

$$I = I_0 \exp(-d/\lambda \cos \theta) \quad (2.18)$$

The inelastic mean free path  $\lambda$  is determined by the kinetic energy of photoelectron and the nature of the material. Figure 2.11 shows the universal curve for electron mean free path. To improve the surface sensitivity, one way is to use synchrotron radiation which can provide energy-variable X-rays. A high surface sensitivity can be achieved by choosing the right photon energy to create photoelectrons with a kinetic energy in the range of 50-100 eV. In this energy range, the probability that electrons emerge from the sample without having been inelastically scattered is high only for electrons from the first few atomic layers. Another way is to carry out angle dependent XPS since the escape depth of electrons is dependent on the emission angle as shown by equation (18). Consequently, a higher surface sensitivity is achieved for a grazing detection angle. But this method is limited to flat surfaces.

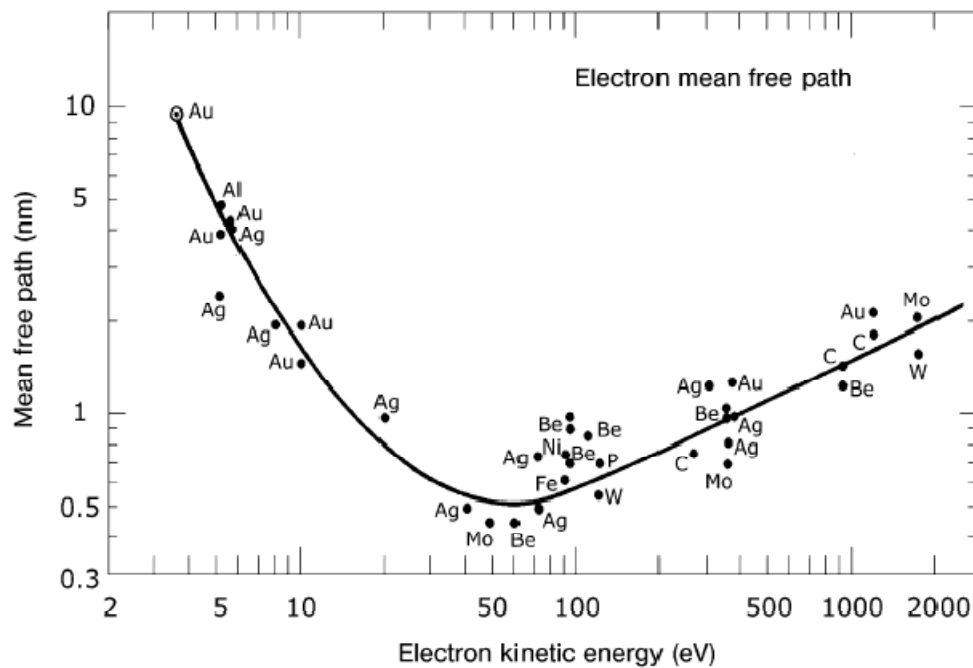


Fig. 2.10 Universal curve for electron mean free path.[92]

### ***Instrument***

An XPS spectrometer contains an X-ray source – usually Mg K $\alpha$  (1253.6 eV) or Al K $\alpha$  (1486.3 eV) –and an analyzer. One application of the dual X-ray sources is to identify Auger peaks. The X-rays penetrate the sample to a depth on the order of a micrometer. The analyzer is usually a hemispherical geometry design. It consists of three components: the collection lens, the energy analyzer, and the detector. In addition to collecting the photoelectrons, the

lens system on most spectrometers also retards their KE's down to the pass energy of the energy analyzer, at which they travel through the hemispherical filter. The lower the pass energy, the smaller the number of electrons that reach the detector, but the more precisely is their energy determined. Behind the energy filter is the actual detector, which consists of an electron multiplier or a channeltron, which amplifies the incoming photoelectrons to measurable currents. Advanced hemispherical analyzers contain up to five multipliers.

### *Auger electron spectroscopy (AES)*

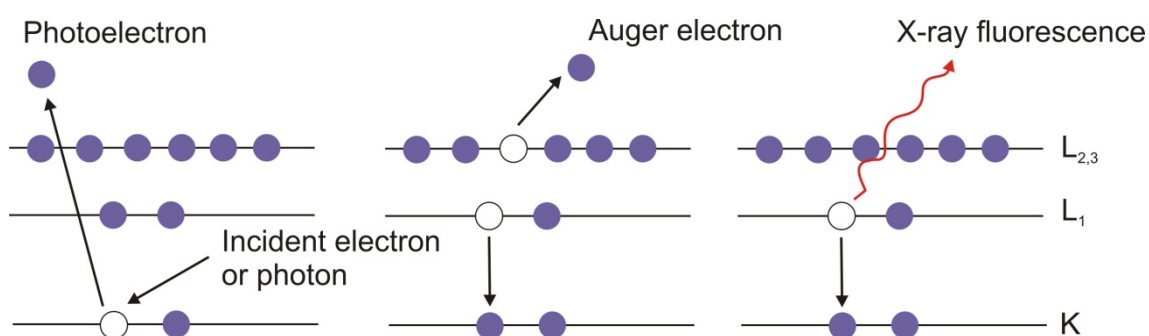


Fig. 2.11. Schematic illustration of the process for the creation of Auger electron.

The Auger effect was discovered in 1923 by P. Auger using X-rays to ionize a gas. However, Auger electrons are not simply a byproduct of XPS. They have been developed as important surface analysis tools, namely Auger electron spectroscopy. Nowadays AES is carried out by exciting the sample with a beam of primary electrons with kinetic energy between 1 and 10 keV. The principle of Auger effect is shown in Figure 2.11. Incident electrons create core holes in the atoms of the sample (e.g. at K level), whereupon the excited atom relaxes by filling the core hole with an electron from a higher shell (e.g. L1). The energy is either liberated as X-ray fluorescence or in an Auger transition by the emission of a second electron (e.g. L2, 3), the Auger electron. The kinetic energy of the Auger electron is entirely determined by the electron levels involved in the Auger process and not by the energy of the primary electrons.

In AES spectra, Auger electrons are seen as small peaks on an intense background of secondary electrons originating from the primary beam. In order to enhance the visibility of the small Auger peaks, spectra are often presented in the derivative mode.[89] Auger energies are as element-specific as binding energies in XPS. However, chemical information such as

oxidation states is much more difficult to abstract. A quantitative analysis of Auger spectra is easily possible, but less straightforward than in XPS. The main reason for this is that the effective intensity of primary electrons in the sample may be higher than that of the primary beam, due to backscattering effects.

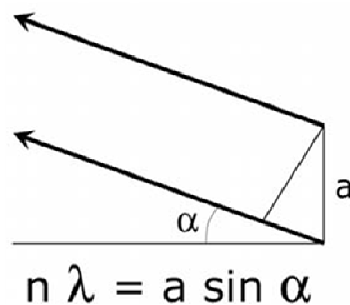
### 2.2.3 Low Energy Electron Diffraction (LEED)

The theoretical possibility of the occurrence of electron diffraction first emerged in 1924 when Louis de Broglie introduced wave mechanics and proposed the wavelike nature of all particles. The de Broglie hypothesis was confirmed experimentally in 1927. The observations were consistent with the diffraction theory for X-rays developed by Bragg and Laue earlier. The wavelength of the electrons is given by the de Broglie relation:

$$\lambda = \frac{h}{p} = \frac{h}{\sqrt{2m_e E_k}} \quad (2.19)$$

For electrons with low energy 20-200 eV, the wavelength is 2.7 Å - 0.87 Å, which is compatible with atomic spacings.

By the principles of wave-particle duality, the beam of electrons may be equally regarded as a succession of electron waves incident normally on the sample. These waves will be scattered by regions of high localized electron density, i.e. the surface atoms, which can therefore be considered to act as point scatterers. Due to the periodic order of the surface atoms, electrons show constructive interference in directions for which the path lengths of the electrons differ by an integral number times the electron wavelength.



Because of the inverse relationship between interatomic distances and the directions in which constructive interference between the scattered electrons occurs, the separation

between LEED spots is large when interatomic distances are small, and vice versa. The LEED pattern has the same form as the so-called “reciprocal lattice”. The relationship between vector of the real lattice and the vectors of the reciprocal lattice (corresponding to the LEED pattern) is shown in Figure 2.12.

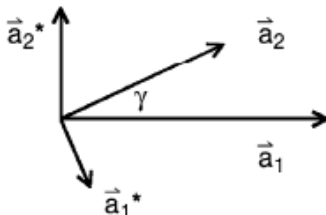
Definition:	$\vec{a}_i \cdot \vec{a}_j^* = \delta_{ij}$	
Directions:	$\vec{a}_1^* \perp \vec{a}_2; \vec{a}_2^* \perp \vec{a}_1$	
Length:	$ \vec{a}_i^*  = \frac{1}{ \vec{a}_i  \cdot \sin \gamma}$	
Angle:	$\angle(\vec{a}_1^*, \vec{a}_2^*) = 180^\circ - \gamma$	
Area unit cell:	$A^* =  \vec{a}_1^* \times \vec{a}_2^* $ $= \frac{1}{ \vec{a}_1 \times \vec{a}_2 } = \frac{1}{A}$	

Fig. 2.12. The relation between the vector of the real lattice ( $\vec{a}$ ) and the vector of the reciprocal lattice ( $\vec{a}^*$ ).  $\delta_{ij}$  is the Kronecker delta,  $\delta_{11}=\delta_{22}=1$ ,  $\delta_{12}=\delta_{21}=0$ . [89]

### 2.2.4 Temperature Programmed Desorption (TPD)

The TPD technique can be used on technical catalysts, but it is particularly useful in surface science. From TPD data the following information can be obtained. Firstly, the area under a peak is proportional to the amount originally adsorbed, i.e. proportional to the surface coverage. Secondly, the position of the peak (the *peak temperature*) is related to the enthalpy of adsorption, i.e. to the strength of binding to the surface. Thirdly, the kinetics of desorption (obtained from the peak profile and the coverage dependence of the desorption characteristics) give information on the state of aggregation of the adsorbed species e.g. molecular vs. dissociative. Finally, if there is more than one binding state for a molecule on a surface (and these have significantly different adsorption enthalpies) then this will give rise to multiple peaks in the TPD spectrum.

Experimental procedures include the adsorption of one or more molecular species onto the sample surface at low temperature and heating of the sample in a controlled manner

(preferably so as to give a linear temperature ramp) whilst monitoring the evolution of species from the surface back into the gas phase usually by quadrupole mass spectrometer.

If the pumping rate is high enough and readsorption is ignored, the rate of desorption can be given by the Polanyi-Wigner equation:

$$r = -\frac{d\theta}{dt} = \nu_n(\theta) \exp\left(-\frac{E_{des}(\theta)}{RT}\right) \theta^n \quad (2.20)$$

where  $r$  is the rate of desorption,  $\theta$  is the coverage in monolayers,  $t$  is the time,  $\nu$  is the pre-exponential frequency factor,  $n$  is the order of desorption,  $E_{des}$  is the activation energy of desorption and  $T$  is the temperature. Attractive or repulsive interactions between the adsorbate molecules make desorption parameters  $E_{des}$  and  $\nu$  dependent on coverage.

The analysis of TPD spectra is complicated. The task is to evaluate activation energies, prefactors and orders of desorption from a series of spectra. The problem is rather complex because both  $E_{des}$  and  $\nu$  (and also sometimes  $n$ ) depend on coverage,  $\theta$ . Thus, we need to determine  $E_{des}$  and  $\nu$  for every coverage separately. Many authors use simplified methods, which make use of easily accessible spectral features such as the temperature of the peak maximum,  $T_{max}$ . In addition, a linear heating is applied,  $T = T_0 + \beta \cdot t$ . By assuming the desorption rate maximum occurs when  $dr/dT = 0$ , the activation energy of desorption can be expressed as:

$$\frac{E_{des}}{RT_{max}^2} = \frac{1}{\beta} \nu_n n \theta^{n-1} \exp\left(-\frac{E_{des}}{RT_{max}}\right) \quad (2.21)$$

For  $n=1$ , equation (2.21) produces:

$$\frac{E_{des}}{RT_{max}^2} = \frac{1}{\beta} \nu_1 \exp\left(-\frac{E_{des}}{RT_{max}}\right) \quad (2.22)$$

Based on the Redhead method [93], the relation between activation energy  $E_{des}$  and  $T_{max}$  can be shown as:

$$E_{des} = RT_{max} \left[ \ln\left(\frac{\nu_1 T_{max}}{\beta}\right) - 3.46 \right] \quad (2.23)$$

Equation (2.23) is very often applied to determine  $E_{des}$  from a single TPD spectrum. The critical point, however, is that one must choose a value for  $\nu$ , the general choice being  $10^{13} \text{ s}^{-1}$ , independent of coverage.

For  $n=0$ , the equation (2.20) becomes:

$$-\frac{d\theta}{dt} = \nu_0 \exp\left(-\frac{E_{des}(\theta)}{RT}\right) \quad (2.24)$$

If it is assumed that the ion current  $I_{ion}$  recorded by the mass spectrometer is proportional to the desorption rate, equation (2.24) can be expressed as:

$$I_{ion} = k\nu_0 \exp\left(-\frac{E_{des}(\theta)}{RT}\right) \quad (2.25)$$

where  $k$  is a constant.

Another way to show equation (2.25) is:

$$\ln I_{ion} = -\frac{E_{des}}{RT} + \ln(k\nu_0) \quad (2.26)$$

Then, when plotting  $\ln(I_{ion})$  with respect to  $1/T$ , one can get  $E_{des}$  from the slope of the line.

# **Chapter 3**

## **The chemistry of Pd catalyst preparation**

### 3.1 Introduction

The preparation of oxide-supported Pd catalysts frequently uses adsorption of Pd precursor complexes from aqueous solutions on the oxide support. Both, the pH dependent charge and speciation of the precursor complex and protonation state of the oxide surface have strong impact on the final properties of the catalyst, such as metal dispersion and distribution.[94] In this chapter, the pH dependent Pd speciation in PdCl<sub>2</sub> containing aqueous solutions will be discussed, followed by a general introduction into the role of the oxide support, and the most frequently employed preparation procedures for oxide supported Pd catalysts.

### 3.2 The chemistry of PdCl<sub>2</sub> solution

The speciation of Pd in PdCl<sub>2</sub> solutions depends on the pH and also on the concentration of Pd and chloride ions. At very low pH (lower than 1), the main solution species is PdCl<sub>4</sub><sup>2-</sup>. With increasing pH, this complex starts to hydrolyze and Cl ligands are replaced by water or hydroxyls. Complexes such as [PdCl<sub>3</sub>(H<sub>2</sub>O)]<sup>-</sup>, PdCl<sub>2</sub>(H<sub>2</sub>O)<sub>2</sub>, [PdCl<sub>2</sub>(OH)<sub>2</sub>]<sup>2-</sup>, [PdCl(OH)<sub>3</sub>]<sup>2-</sup>, Pd(H<sub>2</sub>O)<sub>2</sub>(OH)<sub>2</sub>, Pd(OH)<sub>2</sub> form in solution with increasing pH and coexist according to their hydrolysis constants. In strongly basic solutions, Pd(OH)<sub>4</sub><sup>2-</sup> is the main solution species. At pH values above 4, and depending on the Pd and chloride concentration, the formation of colloidal particles or direct precipitation of Pd(OH)<sub>2</sub> is observed.[95, 96] Without a stabilizing agent, colloidal particles precipitate after some aging time.

PdCl<sub>2</sub> solutions of different pH used in this work as precursor were investigated with UV-Vis spectroscopy. The solutions were prepared from a concentrated acidic PdCl<sub>2</sub> (50 mM) solution that has been adjusted to different pH and a final concentration of 5 mM Pd<sup>2+</sup> by adding NaOH and/or water. For the strongly basic solutions the balance NaOH was added as rapidly as possible to avoid precipitation. Figure 3.1 shows a photograph of the freshly prepared PdCl<sub>2</sub> solutions (top row). In the low pH range (pH 1-2.5) the solutions are light-yellow colored. A significant change in color, to red-brown, is observed for pH 4.7 and higher. The freshly prepared solutions with pH 4.7, 5.3 and 10 are clear, while in the neutral pH range (pH 6.5 and pH 8) immediate precipitation of Pd(OH)<sub>2</sub> occurs. The solutions were allowed to age for 12 hours. After this period, precipitates were also observed for pH 5.3 and pH 10 solution. The flocculent nature of the precipitate in the pH 10 solution points to formation of Pd(OH)<sub>2</sub>, while at pH 5.3 the precipitate is black and finely grained, which could be due to the formation of a PdO(xH<sub>2</sub>O) precipitate. The acidic solutions are stable.

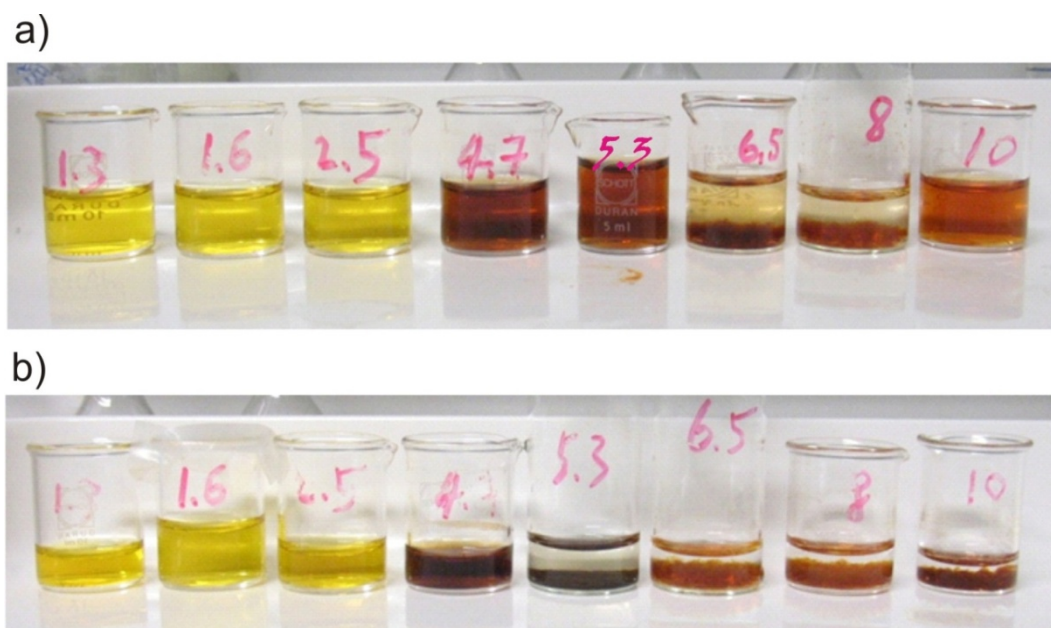


Fig. 3.1. The upper row shows fresh solutions of 5 mM  $\text{PdCl}_2$  with different pH, and the lower row shows the same series of solutions after 12 h aging.

Figure 3.2 shows UV-Vis spectra of a series of  $\text{PdCl}_2$  solutions adjusted to different pH. The observed peak positions are summarized in Table 1. For pH 1.3, a multitude of transitions is observed pointing to the presence of various Pd species. According to literature, the observed transitions can be categorized as ligand-to-metal (LMCT) and metal-to-ligand (MLCT) charge transfer transitions and  $d-d$  transitions ( $d-d$ ), respectively, and at pH 1.3 originate mainly from two Pd species: The transitions at 207 nm and 236 nm (LMCT), 310 nm (MLCT), and 426 nm ( $d-d$ ) are due to the aqua-chloro complex  $[\text{PdCl}_3(\text{H}_2\text{O})]^-$ . Additional transitions at 280 nm (MLCT) and 475 nm ( $d-d$ ) can be assigned to  $[\text{PdCl}_4]^{2-}$ .<sup>[97-101]</sup> The hydrolysis equilibrium shifts towards aqua-chloro complexes with increasing pH, which explains the disappearance of the  $[\text{PdCl}_4]^{2-}$  related spectral transitions upon pH increase to 2.5. At this pH,  $[\text{PdCl}_3(\text{H}_2\text{O})]^-$  is the predominant solution species. At a pH of 4.7, the transitions (LMCT) related to  $[\text{PdCl}_3(\text{H}_2\text{O})]^-$  have lost half of their initial intensity at lower pH as a consequence of proceeding hydrolysis. However, instead of new transitions according to the hydrolysis products, strongly increased background absorption, starting at 500 nm and extending down to 200 nm, is observed. Likewise, for pH 10 and pH 12 solutions, spectra exhibit similar increased background absorption and a rise at short wavelengths with a feature centered at 270 nm. (Because of the rapid precipitation, no UV-Vis spectra were taken from pH 6 and pH 8.5 solutions.) Comparison with Figure 3.1 shows that the changes in the UV-Vis spectra correlate with the color change from light yellow at low pH to red-brown at higher pH.

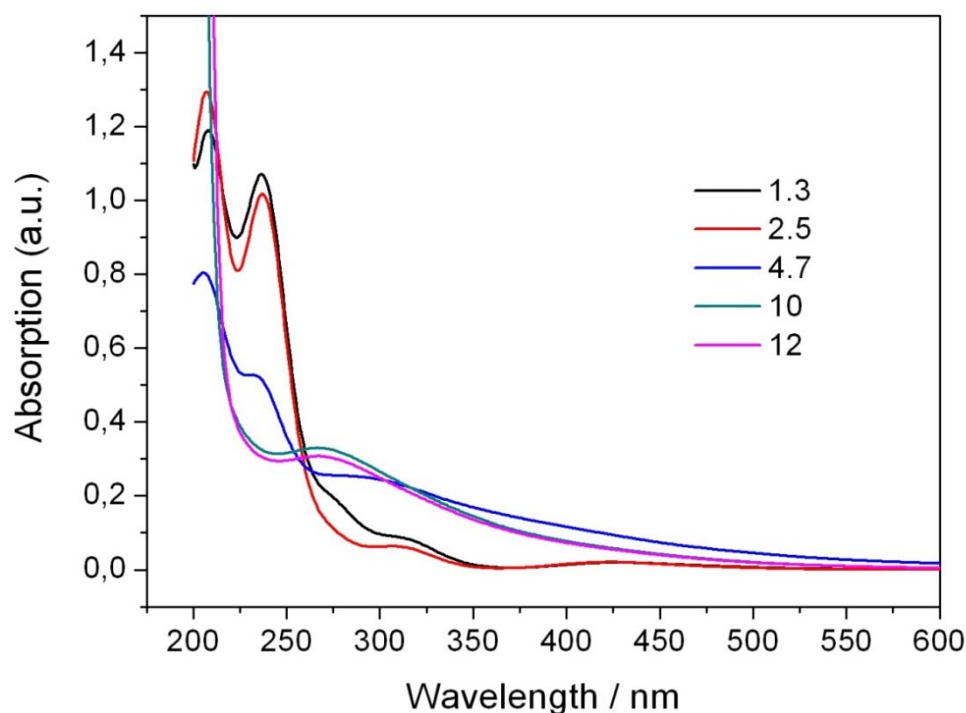


Fig. 3.2. UV-vis Spectroscopy of 0.1 mM PdCl<sub>2</sub> solutions of different pH.

Table 1. UV-vis Spectroscopy peak positions of 0.1 mM PdCl<sub>2</sub> solutions with different pH.

pH	$\lambda$ / nm
1.3	207, 236, 280, 310, 426, 475
2.5	207, 236, 310, 426
4.7	207, 236, 300
10, 12	266

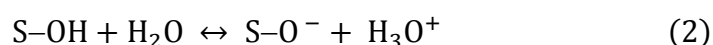
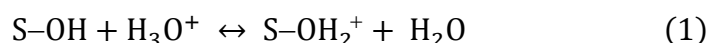
The increased background absorption and rise at short wavelengths is characteristic for the formation of colloidal particles commonly observed upon hydrolysis of Pd complexes.[100, 102] The possible origin of the colloidal particles is the formation of neutral aqua-chloro complexes [PdCl<sub>2</sub>(H<sub>2</sub>O)<sub>2</sub>], which tend to polymerize very rapidly, during hydrolysis. The nature of the colloids has been the subject of several studies and it is generally agreed that they are polynuclear Pd<sub>n</sub>-hydroxo complexes (with n = 3-100), which, depending on the chlorine concentration in the starting solution, might also contain chlorine ligands.[103] While spectra like the ones shown for pH 4.7, 10, and 12 indicate the formation of colloidal particles, the assignment of the absorption at 270 nm is debated. Klasovsky et al. assigned this feature to Plasmon excitation in the colloidal particles,[100] while Boily argues that this energy is also compatible with a charge-transfer transition of Pd chloro-hydroxo complexes, PdCl<sub>x</sub>(OH)<sub>y</sub><sup>n-</sup>, which, according to the hydrolysis equilibrium, are stable solution species

under the present experimental conditions (pH 10).[103] In addition to polynuclear complexes, monomeric  $\text{Pd}(\text{OH})_4^{2-}$  should be present at high pH values. However, this species cannot be unambiguously identified with UV-Vis.

In conclusion, the experimental results presented above provide some ideas about the speciation of Pd in the respective precursor solutions. In the low pH range, Pd exists predominantly as chloro and aqua-chloro complexes, while at a pH of 4.7 both, monomeric aqua-chloro and polynuclear Pd complexes, most probably containing a mixture of chloro and aqua ligands, are present in solution. pH adjustment to strongly basic conditions results in the formation of both monomeric  $\text{Pd}(\text{OH})_4^{2-}$  and polynuclear Pd-hydroxo complexes.

### 3.3 The oxide surface

The solution pH at which metal precursor adsorption is carried out is an important parameter in catalyst preparation and can significantly affect the final properties of a catalyst. As shown above, pH determines the speciation of the solution complexes and, therefore, the chemical nature of the adsorbing species. In addition, the solution pH affects also the support, that is, the charge of the support surface. When the oxide is in contact with an aqueous solution, the hydroxyls groups on the oxide surface behave as Brønsted bases or acids according to the following reactions.



The resulting surface charge arising from an excess of either cations or anions is a function of the pH. At a specific pH, the amount of positive charges exactly balances the amount of negative charges resulting in a zero net charge. This pH is called the *point of zero charge* (PZC). Thus, when the pH is lower than the PZC, the oxide surface is positively charged and adsorbs preferentially anions; when the pH is higher than the PZC, the oxide surface is negatively charged and cation adsorption is favored. Apart from surface charge changes, dissolution of the support may also occur when the support reacts with the solution at some pH value. Thirdly, pH affects the interaction between metal complexes and the support. There are different types of interaction such as electrostatic interaction, grafting and chemical

bonding. For example, if the precursor complex is an anion in solution, at a pH value below the PZC, the main interaction between the precursor and the support is electrostatic interaction. As a result of the above three kinds of effects, the pH affects the loading, the size and distribution of metal particles, the composition of metal species during preparation and finally the performance of the catalyst.[40, 101, 104-107]

### 3.4 Overview of catalyst preparation methods

Various wet chemical methods such as coprecipitation, deposition precipitation, deposition-reduction, photo-reduction, ion-exchange and impregnation, have been developed to prepare supported Pd catalysts. In the following paragraphs, a short overview of the two most frequently applied methods, impregnation and deposition precipitation, which were also used in the present study, will be given.

#### **Impregnation**

Among wet chemical methods, impregnation is the conventional technical method to prepare supported noble metal catalyst such as Pt and Pd. In impregnation, the support, which is usually applied in the form of a porous powder, is contacted with a solution containing a precursor of the active component. When the pore space of the support is filled with ambient air before introduction of the precursor solution, the procedure is called capillary impregnation. When the support is already filled by the solvent of the impregnation solution or by another solvent, it is named diffusion impregnation [38]. Impregnation can also be classified as wet or dry impregnation depending on whether the volume of the impregnating solution is in excess or equal to the pore volume of the support. Dry impregnation, in which the amount of metal-loaded solution is added to a porous oxide in just the amount needed to fill the pore volume, is alternatively termed “incipient wetness impregnation” or “pore filling.” [108] The chemistry of impregnation involves the adsorption and interaction of the precursor with the support. It is usually dominated by electrostatic interactions when the support surface and precursor exhibit opposite charge signs. The counter ion is also retained on the support by electrostatic interactions and may affect the composition and morphology of the support. When the precursor support interaction is strong, a grafting reaction (chemical bonding) between precursor and support may occur.

In conventional impregnation a washing step is avoided in order to retain the full amount of the expensive precious metal on the support surface. However, several recent studies have shown that a washing step can be useful to adjust the properties of the catalyst [109-111]. The washing step may have the following consequences: Firstly, it can eliminate the weakly adsorbed ions from the surface of the support. For example, chloride, which can influence the surface properties by chemical reaction with the support surface during the calcinations step and, can be eliminated by washing. Secondly, the local pH at the support surface is altered by washing leading to different interactions of the adsorbed precursor complexes with the support. And finally, washing can also cause hydrolysis of precursors complexes and thus change the speciation of the precursor.

$\text{PdCl}_2$  and  $\text{Pd}(\text{NO}_3)_2$  are the most widely used precursors in Pd catalyst preparation by impregnation. In particular, the effect of using chlorine-containing precursors has received considerable attention in catalysis because chlorine residues from the precursor can have either a positive or negative effect on the catalytic activity, depending on the catalyst system and the catalytic reaction under study. On the one hand, chlorine has been reported to act as a poison in catalysis because it blocks the active surface sites and leads, therefore, to a decrease of reactivity and catalyst lifetime [112, 113]. On the other hand, residual chlorine exhibits a positive effect for particular reactions because it helps maintaining high dispersion of metal particles during reaction [114]. Some authors reported that Cl is responsible for the formation of larger sized particles [113, 115], but this conclusion does not always hold. For example, in another study, Pd catalysts impregnated with a  $\text{PdCl}_2$  precursor were found to exhibit smaller particle size than those that were prepared using  $\text{Pd}(\text{NO}_3)_2$  as a precursor [116]. Cl also affects the vibrational spectra of probe molecules. It weakens the adsorption of molecules on metal surfaces (lineally bound CO peak intensity is stronger than bridged ones) and might affect the crystallite morphology [117, 118].

In addition to chlorine residues from the precursor complexes, a possible effect of chloride in solution, for example when the precursor solution was acidified with hydrochloric acid, cannot be neglected. It has been reported the competitive adsorption of Cl acts to favor uniform distribution of the metals on the support [101]. Cl may coordinate to the surface of metal particles, adsorb on the support or stay at the metal support interface. The interaction of Cl with the support depends on the type of oxide. In some cases, for example with ceria, there is a strong interaction of Cl with the support surface resulting in the formation of a Cl containing oxygenate complex [119, 120]. The strong adsorption of Cl on the support may also change the morphology of the support [119, 120]. For other supports, e.g. silica, Cl

interaction with the support was found to be very weakly [121]. It is often difficult to completely remove the Cl from the surface. Methods that are usually applied for Cl removal, for example, ligand exchange by hydrolysis, washing, or long-term oxidation, lead to unwanted side effects such as particle coarsening.

### **Deposition precipitation**

Deposition-precipitation is another important wet chemical method to prepare supported catalysts [108, 122, 123]. In this technique, a catalyst precursor is applied to a support by precipitation. It was originally developed to obtain high loadings of non-precious metals such as Ni, Co and Fe, finely distributed over the support surface.

Deposition precipitation starts with a suspension of the support in a solution containing a highly soluble metal precursor complex. The soluble metal complex is then chemically transformed into a compound with low solubility. It is important to maintain the concentration of the newly formed compound in a range between the solubility and supersolubility points. Because of the interaction of the precursor with the support, the supersolubility point is shifted to lower concentration at the support-solution interface compared to the bulk solution phase. Therefore, precipitation of the precursor occurs exclusively at the support and not in solution. There are several ways to bring about precipitation: pH increase, reduction and ligand removal. Among them, pH increase is most often applied. The precipitants used for pH adjustment are usually alkaline solutions (e.g. NaOH and Na<sub>2</sub>CO<sub>3</sub>) or compounds that lead to slow pH increase by releasing OH upon temperature increase (e.g. urea). Slow increase of pH is important to avoid a rise of the precursor concentration above the supersolubility point in solution, which would lead to unwanted precipitation in solution.

More recently, a modification of the DP method [124-126] was found efficient to obtain low loadings of very small precious metal particles (Au and Pd) on support surfaces. In recent years, a modified deposition-precipitation method, where the precursor solution is being adjusted to the desired pH with alkaline precipitants before contact with the support has also been developed. This method has become famous because highly active gold catalysts could be obtained in that way.[124]

---

### 3.5 Wet chemical catalyst preparation procedures and surface science – restrictions

The flat substrate that was applied in this work to study wet chemical catalyst preparation with surface science techniques imposes several restrictions as to the applicability of the various preparation methods. Related to impregnation, the absence of pores excludes the application of incipient wetness impregnation. Instead, an excess of precursor solution is used here (wet impregnation). As to deposition precipitation, vigorous stirring of the support-precursor suspension is not possible with a single-crystalline support. Homogeneous deposition precipitation, which relies on slow pH increase and stirring, is, therefore, not possible. As an alternative, a modified DP method is used where the support is left in contact with the precursor solution for a given period of time at constant (basic) pH.

# Chapter 4

## Single crystalline FeO(111)/Pt(111) and Fe<sub>3</sub>O<sub>4</sub>(111)/Pt(111) films

Parts of the results presented in this chapter have been published in:

F. Ringleb, Y. Fujimori, H.-F. Wang, H. Ariga, E. Carrasco, M. Sterrer, H.-J. Freund, L. Giordano, G. Pacchioni, J. Goniakowski

**Interaction of water with FeO(111)/Pt(111) thin films - Environmental effects and influence of oxygen.**

*The Journal of Physical Chemistry C*, 2011, **115**, 19328.

## 4.1 Introduction

Iron oxides are important oxide materials and applied in many fields such as environmental science, catalysis, electrochemistry and biology. In nature, iron oxides occur in four different phases: wüstite (FeO), magnetite (Fe<sub>3</sub>O<sub>4</sub>), hematite ( $\alpha$ -Fe<sub>2</sub>O<sub>3</sub>) and maghemite ( $\gamma$ -Fe<sub>2</sub>O<sub>3</sub>). In addition, there are also other kinds of iron oxides such as oxide-hydroxides (e.g. FeOOH) and hydroxides (e.g. Fe(OH)<sub>3</sub>). Iron oxides are environmentally important minerals and have been investigated with respect to dissolution and metal uptake from solution.[127] For fundamental understanding of the surface properties of iron oxides, both bulk single crystal samples and thin films deposited on metallic substrates have been investigated under ultrahigh vacuum conditions with surface science techniques.[55, 128-135]. In this thesis, FeO(111) and Fe<sub>3</sub>O<sub>4</sub>(111) are used as supports for Pd nanoparticles, which are deposited from a solution that contains Pd precursor complexes. The deposition process and the properties of the resulting Pd nanoparticles will be discussed in the following chapters (Chapter 5 and Chapter 6). In this chapter, a short review about the properties of FeO(111) and Fe<sub>3</sub>O<sub>4</sub>(111) will be given. Because the stability of the oxide supports in contact with the catalyst precursor solution is essential for their application in catalyst preparation studies, the review part is followed by experimental results concerning the properties of these oxides upon exposure to aqueous solutions.

## 4.2 Properties of FeO(111) and Fe<sub>3</sub>O<sub>4</sub>(111)

### FeO(111)

FeO crystallizes in the NaCl structure. The large oxygen anions in the crystal form a cubic closed packed (ccp) lattice with small iron cations located in octahedral sites (Figure 4.1a). The unit cell contains four formula units and has a lattice constant of 4.3 Å. Planes of oxygen alternate planes of iron. Naturally occurring FeO is nonstoichiometric (Fe-deficient) by forming Fe<sub>1-x</sub>O, which is caused by partial oxidation of Fe<sup>2+</sup> to Fe<sup>3+</sup>. [127, 136]

For a FeO(111)/Pt(111) film less than 1 ML thick, UHV-STM studies (Figure 4.1b) show that the in-plane lattice parameter is 3.1 Å, which is slightly larger than the corresponding bulk value of 3.0 Å.[137] The atomic periodicity is modulated by a larger periodicity of about

25 Å, which creates the Moiré superstructure, seen also in the LEED pattern shown in Figure 4.1b.

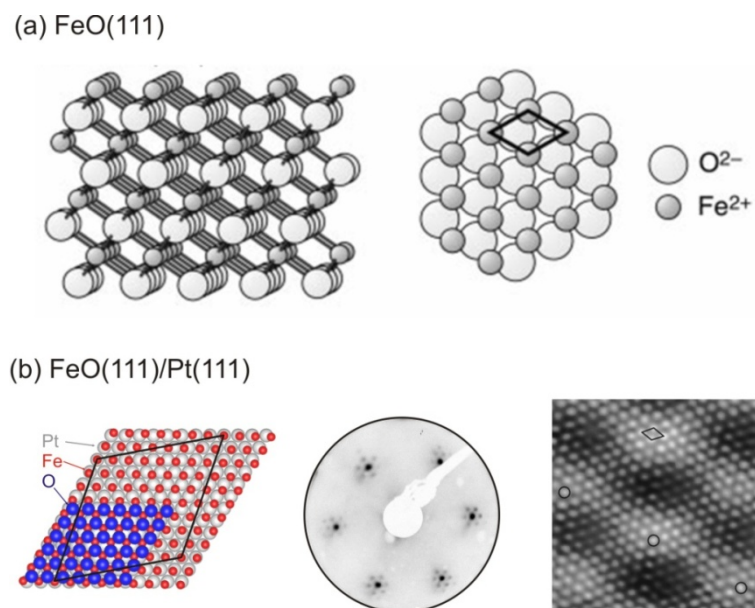


Fig. 4.1. (a) Model structure of single crystal FeO(111) with side view (left) and top view (right) [136], (b) model structure, LEED pattern and STM image [137] with atomic resolution of FeO(111)/Pt(111) thin film.

The Moiré structure is caused by the 11% in-plane lattice mismatch between the oxide layer and the Pt substrate lattice. A model structure of this film is shown in Figure 4.1b. It consists of a laterally expanded oxygen terminated FeO(111) bilayer on top of the Pt(111) surface. The coincidence overlayer structure has a large unit cell size and is rotated by about  $10.9^\circ$  with respect to the unit cell of the Pt(111) surface. The bulk FeO(111) surface is unstable because of the dipole moment normal to the surface. However, the polar instability of FeO film can be compensated by a structural transformation driven by the metal substrate underneath the film [138]. Combined photoelectron diffraction, STM and theoretical calculations found that the lattice expansion is additionally accompanied by reduction of the Fe-O interplane distance from 1.26 Å in bulk FeO to 0.68 Å for 1 ML FeO [139], corresponding to a reduction of the Fe-O bond length from 2.16 Å to 1.8 Å [140].

### Fe<sub>3</sub>O<sub>4</sub>(111)

Fe<sub>3</sub>O<sub>4</sub> is ferromagnetic and crystallizes in the inverse spinel structure. The crystal consists of a cubic closed packed fcc oxygen lattice with Fe<sup>2+</sup> located in octahedral sites and Fe<sup>3+</sup> in

both octahedral and tetrahedral sites. The unit cell has a lattice constant of 8.39 Å and contains eight formula units. Figure 4.2a shows a model structure of Fe<sub>3</sub>O<sub>4</sub>. Fe<sub>3</sub>O<sub>4</sub> exhibits high electrical conductivity at room temperature because of electron hopping between Fe<sup>2+</sup> and Fe<sup>3+</sup> ions.

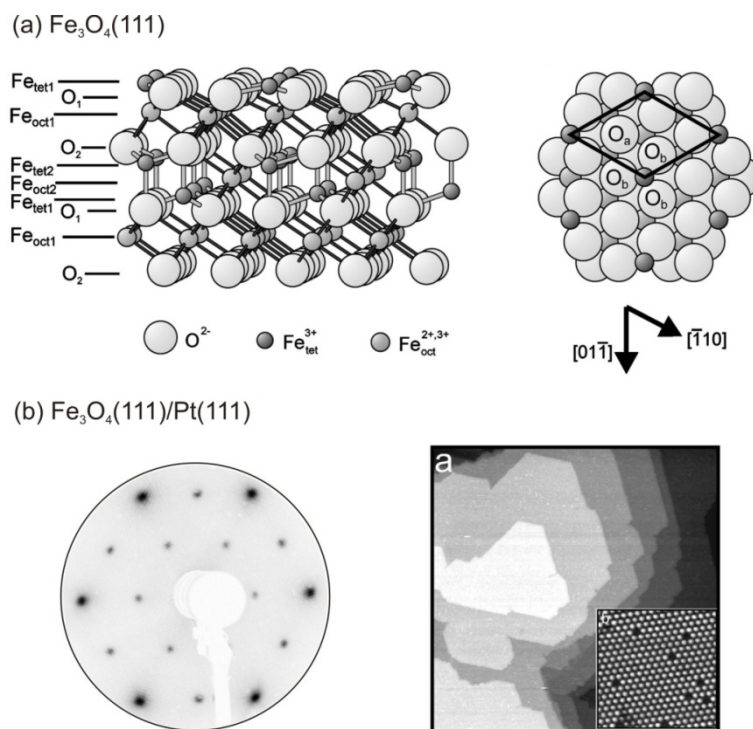


Fig. 4.2. (a) Model structure of single crystal Fe<sub>3</sub>O<sub>4</sub>(111) with side view (left) and top view (right) [141], (b) LEED pattern and STM images [141] of Fe<sub>3</sub>O<sub>4</sub>(111)/Pt(111) film.

The LEED pattern of an Fe<sub>3</sub>O<sub>4</sub>(111)/Pt(111) film (Figure 4.2b) shows a quasi p(2×2)-Fe<sub>3</sub>O<sub>4</sub>(111) diffraction pattern, which is identical to the bulk Fe<sub>3</sub>O<sub>4</sub>(111) surface. Figure 4.2b also shows large scale and atomically resolved STM images of a 10 nm thin Fe<sub>3</sub>O<sub>4</sub>(111) film. The surface termination of Fe<sub>3</sub>O<sub>4</sub>(111) is still debated [55, 142]. From STM and LEED studies it was concluded that the oxide film is terminated by 1/4 ML of Fe: Fe<sup>3+</sup><sub>tet</sub> on top of a closed-packed oxygen layer, while combined TDS and infrared studies of adsorbed CO suggest that the surface layer consists of Fe<sup>2+</sup><sub>oct2</sub> (see Figure 4.2a).

The growth of iron oxide films on Pt(111) has been studied by STM and LEED and follows a Stranski-Krastnov growth mode [138]. Initially, the thin FeO film grows layer by layer and Fe<sub>3</sub>O<sub>4</sub> islands appear with increasing amount of the deposited iron. The FeO film is limited to a maximal thickness of 2.5 ML because of the high surface energy that builds up in thicker

films. The  $\text{Fe}_3\text{O}_4$  islands grow in the  $\text{Fe}_3\text{O}_4$  bulk structure laterally much faster than vertically, forming flat platelets with heights up to 100 Å and hexagonal and triangular basal planes 1000–5000 Å in diameter. The growth of islands can be described by an Ostwald ripening mechanism that occurs during each oxidation cycle. Eventually the islands coalesce and form smooth  $\text{Fe}_3\text{O}_4(111)$  films. Pt(111) was chosen as the support for the growth of iron oxide films because it has a lattice constant of 2.77 Å which is similar to FeO (3.04 Å) and a hexagonal surface unit cell same as FeO(111). In addition, there is also a high adhesion energy and good epitaxial relationship between iron oxides and Pt.

### XPS of iron oxides

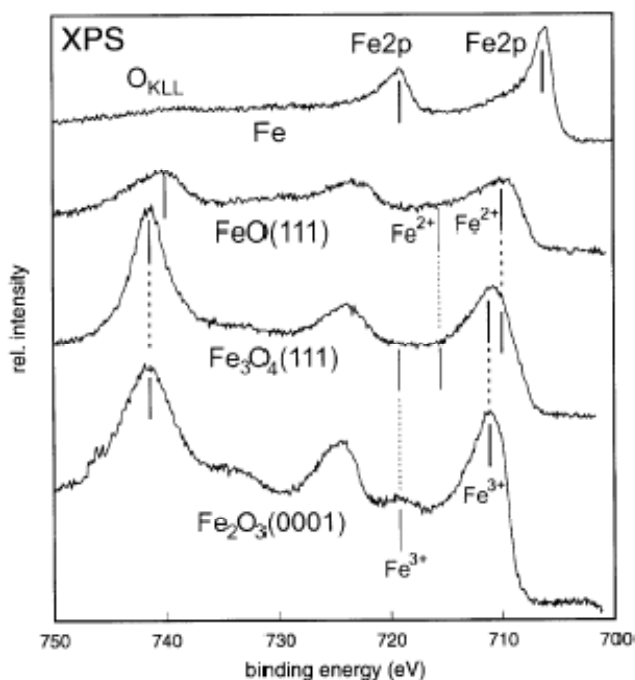


Fig. 4.3. XPS spectra of evaporated elemental Fe film and iron oxide films grown on Pt(111). FeO(111) film (1-2 ML), and at least 10 nm thick  $\text{Fe}_3\text{O}_4(111)$  film and  $\alpha\text{-Fe}_2\text{O}_3(0001)$  films.[55]

XPS can be applied to distinguish between the different iron oxides. Figure 4.3 shows the Fe 2p XP spectra of metallic Fe and three iron oxide films. The Fe  $2p_{3/2}$  peak positions of Fe, FeO and  $\text{Fe}_2\text{O}_3$  are found at binding energies of 706.3 eV, 710.0 eV and 711.3 eV, respectively. Clearly, these values correspond to the binding energy of  $\text{Fe}^0$ ,  $\text{Fe}^{2+}$  and  $\text{Fe}^{3+}$  species. Characteristic  $\text{Fe}^{2+}$  and  $\text{Fe}^{3+}$  satellites can be observed in the spectra of FeO and

$\text{Fe}_2\text{O}_3$  as shown in the Figure 4.3.  $\text{Fe}_3\text{O}_4$  contains both  $\text{Fe}^{2+}$  and  $\text{Fe}^{3+}$ , which causes a broadening of the Fe 2p emission compared to  $\text{Fe}_2\text{O}_3$ .

### **Water adsorption on iron oxides**

Meaningful results have been obtained about water adsorption at low pressures on the surfaces of iron oxides [143-151]. The main conclusion is that FeO surface is inert to water with only weakly adsorbed water molecules on the surface. A dissociative adsorption of water resulting in hydroxyl groups has been observed on  $\text{Fe}_3\text{O}_4$  surfaces. The adsorption sites are assigned to  $\frac{1}{4}$  ML of Fe sites on the regular  $\text{Fe}_3\text{O}_4$  surface. Recently, it is found that the FeO(111)/Pt(111) thin film exposed to elevated  $\text{O}_2$  pressure can form an ordered trilayer structure (Pt-O-Fe-O) [152, 153]. The adsorption of high pressure water or liquid water on FeO has not been investigated. The interaction of high pressure water vapor and liquid water with single crystal  $\text{Fe}_3\text{O}_4$  have already been studied by XPS and STM.[144, 148] The results show that the  $\text{Fe}_3\text{O}_4$  surfaces react with water more extensively at higher water pressure with hydroxylation extending several layers deep into the bulk. In addition, it was found that the oxidation state of iron does not change after immersing oxides in liquid water.

### **Iron oxides as catalyst support**

Iron oxides themselves are catalysts, for example, applied in the dehydrogenation of ethylbenzene to styrene. They are also often used as supports for metal catalysis. Traditionally  $\text{Fe}_2\text{O}_3$  was used as catalyst support. In recent years, people started to find interesting catalytic properties for  $\text{FeO}_x$  ( $x < 1.5$ ) supported Pd catalysts such as high activity for low temperature CO oxidation and reforming of ethylene glycol to hydrogen because of its redox properties and oxygen storage capability [154, 155].

### **Preparation of Pt(111)-supported FeO(111) and $\text{Fe}_3\text{O}_4$ (111) films**

The preparation of FeO(111) and  $\text{Fe}_3\text{O}_4$ (111) films used in this study follows recipes described in the literature [55]. First, the Pt(111) film is cleaned by repeated  $\text{Ar}^+$  sputtering (RT), oxidation (600 K), and annealing (1200 K) cycles until a sharp hexagonal LEED pattern characteristic for Pt(111), and removal of all carbon contamination as detected with XPS is achieved. A monolayer equivalent (MLE) of Fe is then evaporated on the clean Pt(111)

surface at room temperature. Oxidation of the Fe layer in  $1 \times 10^{-6}$  mbar  $O_2$  at 1000 K for 2 min. resulted in the FeO(111) film exhibiting the characteristic Moiré pattern in LEED.

The FeO(111) film served as substrate for a  $\sim 10$  nm thin  $Fe_3O_4(111)$  film, which was prepared by repeated (5x) cycles of Fe deposition (8 ML) and oxidation ( $1 \times 10^{-6}$  mbar) at 900 K. A final oxidation step at 1000 K yielded the  $Fe_3O_4(111)$  film with the characteristic  $p(2 \times 2)$  diffraction spots in LEED.

### 4.3 Stability and structure of FeO(111)/Pt(111) film in air and liquid water

FeO(111) films were prepared in UHV according to the procedure described above and characterized with LEED and XPS. Subsequently, the films were transferred into air and contacted with various solutions. The sample surfaces were characterized in air with STM or, alternatively, with XPS and IRAS after back-transfer into the UHV chamber.

#### 4.3.1 STM characterization

The STM image taken in air (Figure 4.4a) shows a periodic structure that is similar to the Moiré superstructure observed for FeO(111)/Pt(111) in UHV [137]. It is observed that the STM image contrast of FeO films in air changed with increasing bias voltage. As seen from the images in Figure 4.4b and 4.4c, the surface appears rougher with bright protrusions distributed over the whole sample surface when the bias is at more negative (e.g. -1.80 V) or more positive (e.g. 1.00 V) values. This effect cannot be attributed to STM tip changes because both structures are reversibly imaged by slowly changing the bias. Variations in STM image contrast have been reported for FeO(111)/Pt(111) in UHV as being due to field emission resonances, which typically occur at bias voltages  $> 3V$ . [134] Because the change in image contrast was observed here at much lower bias voltage, it can be excluded that field emission resonances are the reason for this observation. It is more likely that impurities, which accumulated on the surface during air exposure, give rise to these features. In fact, similar features were observed during long-time STM measurements on  $Fe_3O_4(111)$  in UHV, and have been attributed to adsorbed water [156]. Therefore, we ascribe the bias dependent features to adsorbed molecules such as  $H_2O$  and  $CO_2$ .

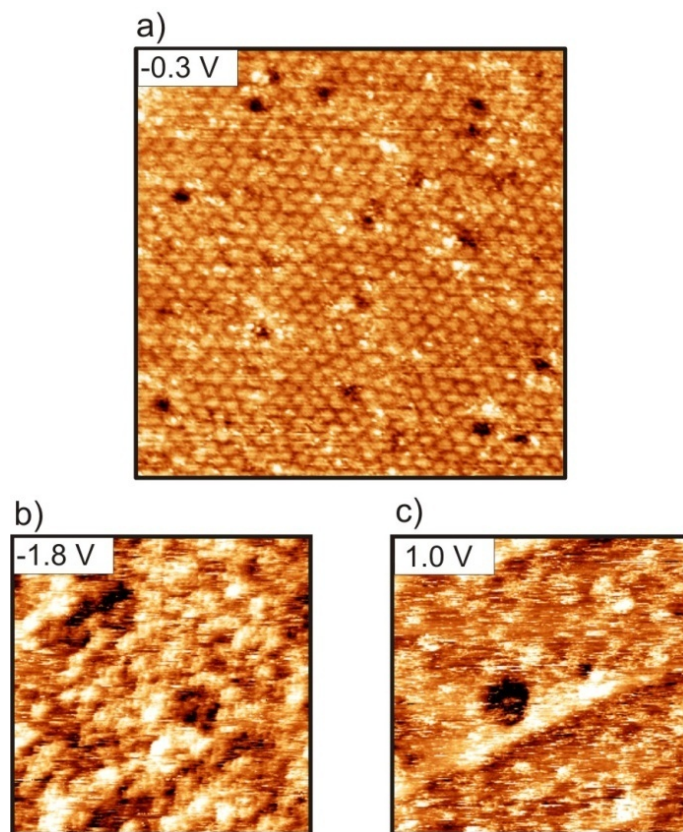


Fig. 4.4. STM images of FeO films taken in air at bias voltages of -0.3 V (a), -1.8 V (b) and 1.0 V (c). All images are  $60 \text{ nm} \times 60 \text{ nm}$ .

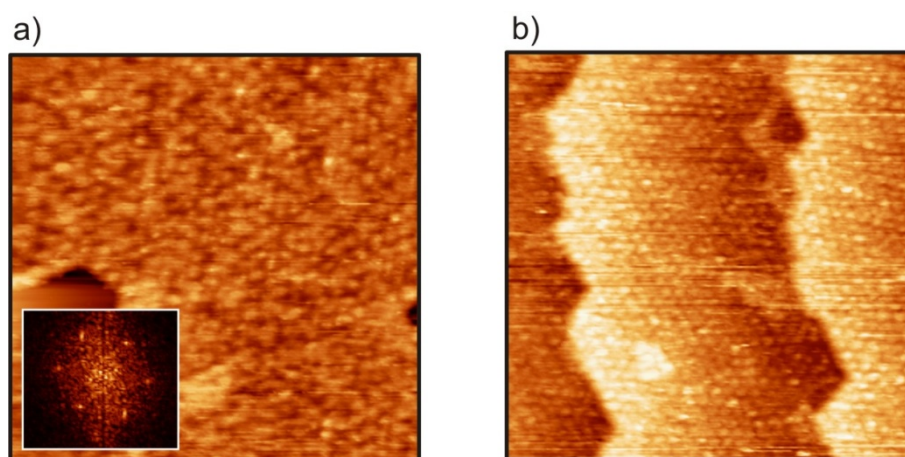


Fig. 4.5. STM images of FeO films taken in-situ in liquid water (a), in air after in liquid water (b). Both images are  $60 \text{ nm} \times 60 \text{ nm}$ .

In Figure 4.5, STM images of FeO(111)/Pt(111) taken in liquid water (a), and in air after removing liquid water and subsequent drying at RT (b) are shown. The in-situ STM image

taken of the FeO(111) in contact with liquid water (Figure 4.5a) reveals more structural disorder as compared to Figure 4.4a. However, the fast Fourier transformation (FFT) of this image (see inset in Figure 4.5a) provides evidence for remaining hexagonal symmetry of the structures observed in Figure 4.5a. Most notably, after removing liquid water, the film is similarly well ordered as the film before water treatment (Figure 4.5b), providing evidence for high stability of the FeO layer, even in aqueous environment.

After contacting the FeO film with liquid water, the thermal stability of such a film was examined by STM as shown in Figure 4.6. The RT image shows a flat surface with sharp steps. When the sample was annealed to 373 K in UHV, the surface becomes rough but steps are still apparent. Upon increasing the annealing temperature to 800 K, some protrusions appeared on the terraces. Protrusions may correspond to iron oxide particles because of dewetting or partial reduction of the film. Further annealing to 1000 K leads to dewetting.

In summary, FeO films are stable in air and liquid water and break only after heating in UHV. STM results suggest the inert nature of FeO film surfaces.

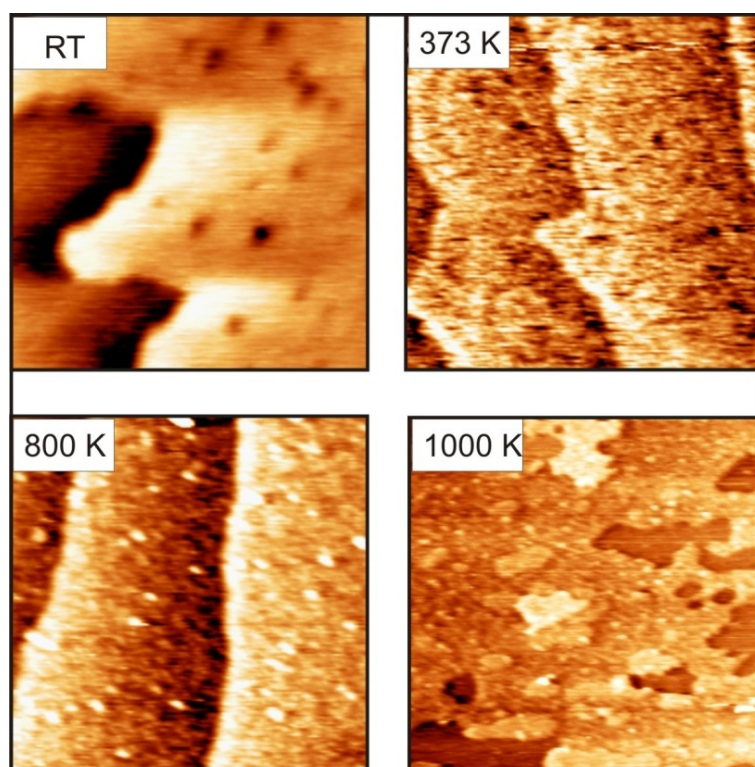


Fig. 4.6. STM images of FeO films firstly contact with liquid water at RT, and then heated to 373 K, 800 K and 1000 K in UHV. All images are  $100 \text{ nm} \times 100 \text{ nm}$ .

### 4.3.2 Chemical characterization

The chemical state and surface termination of the FeO(111) films after various treatments were determined by XPS and infrared spectroscopy. Figure 4.7a shows the O 1s XP spectrum of the clean FeO(111) film, and after exposure to air and liquid water. The clean film exhibits a single O 1s component at 529.5 eV [55, 157]. Upon exposure to air, the shoulder appearing on the high binding energy side of this peak can be fitted with a second component with a binding energy of 531.2 eV, consistent with the O 1s of hydroxyls [158, 159]. After liquid water treatment the O 1s region only slightly changed as compared to air exposure, with more intensity in the hydroxyl peak and slightly less in the oxide peak (Figure 4.7a). Changes upon exposure to air and water are also observed in the Fe 2p region, with a shift of the peak from 710.0 eV for exclusively Fe<sup>2+</sup> in the clean FeO(111) film, to 711.0 eV after exposure to water, indicating oxidation of Fe<sup>2+</sup> to Fe<sup>3+</sup> (Figure 4.7b) [158, 159]. Finally, PM-IRAS spectra measured after air and liquid water exposure of FeO(111) indicate the formation of surface hydroxyl groups exhibiting stretching frequencies in the range 3620–3650 cm<sup>-1</sup> (Figure 4.7c).

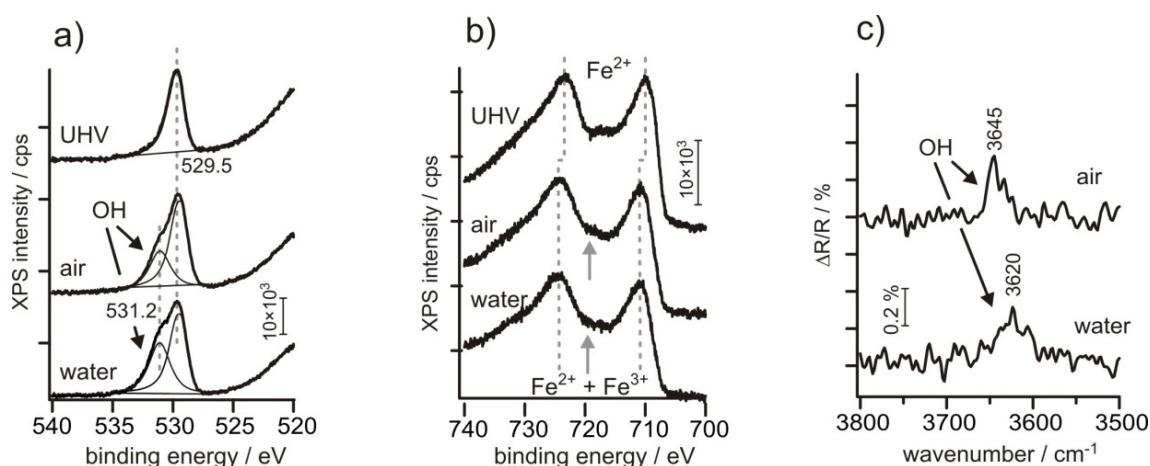


Fig. 4.7. XPS and PM-IRAS spectra from clean FeO(111)/Pt(111) and after contact with air and liquid water. (a) XPS O 1s region, (b) XPS Fe 2p region, (c) PM-IRAS OH region. (Provided by E. Carrasco)

### 4.3.3 Discussion

The STM images presented in Figure 4.4 and Figure 4.5 provide strong evidence for the stability of the monolayer iron oxide film on Pt(111) in various environments with no sign of de-wetting, even in liquid water. Spectroscopic characterization, however, gives clear

indication of chemical modification of the film, with significant enrichment with oxygen, oxidation of  $\text{Fe}^{2+}$  to  $\text{Fe}^{3+}$ , and hydroxyl termination. Based on integration of the O 1s peak components of the clean and modified films (Figure 4.7a), a hydroxyl coverage of, respectively, 0.48 ML in air, and 0.63 ML after water treatment, is estimated (where 1 ML is defined with respect to the full oxygen monolayer in the clean  $\text{FeO}(111)$  film). The results are compatible with the transformation of the (Pt)–Fe–O bilayer film into a trilayer film under the action of high oxygen chemical potential [153]. However, unlike for oxygen termination, (Pt)–O–Fe–O, such as observed previously after mbar  $\text{O}_2$  treatment of  $\text{FeO}(111)$  at 450 K, in the present case the surface is terminated by hydroxyl groups, calling for a structure similar to (Pt)–O–Fe–OH. This observation consequently requires that molecular water was dissociatively adsorbed on the surface. Control experiments, where the  $\text{FeO}(111)$  film was exposed to a controlled atmosphere of water vapor (up to 10 mbar) in the absence of oxygen, have shown that water vapor alone does not lead to formation of hydroxyls in significant amounts.[160] Therefore, oxygen (in the present case delivered by air) is necessary for hydroxyl formation on  $\text{FeO}(111)$  thin films.

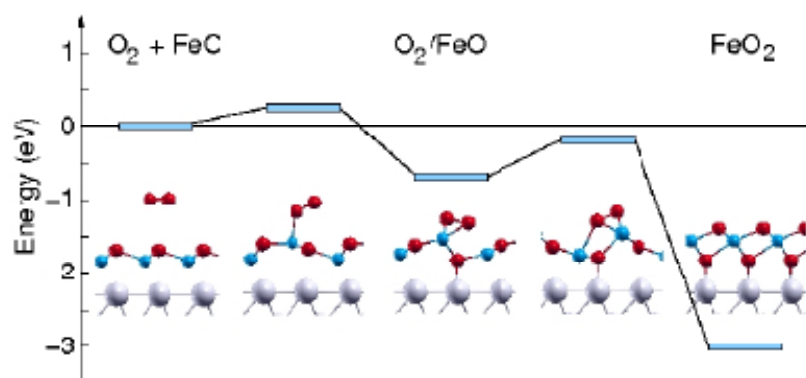


Fig. 4.8. Energy profile for the oxidation of the  $\text{FeO}/\text{Pt}(111)$  film upon exposure to  $\text{O}_2$  at high oxygen coverage. Blue (Fe), red (O), yellow (C), gray (Pt).[153]

The formation of a  $\text{FeO}_2(111)$  trilayer upon exposure of  $\text{FeO}(111)$  to high pressures (mbar range) of oxygen at high temperature has been suggested in a previous study on the basis of TPD and AES measurements [152]. Density functional calculations subsequently provided a mechanism for this transformation. Figure 4.8 shows the individual steps of interaction of  $\text{FeO}(111)$  with  $\text{O}_2$  that leads to formation of the  $\text{FeO}_2$  trilayer [153]. These include the outward movement of Fe during interaction with  $\text{O}_2$ , a charge transfer from the substrate to  $\text{O}_2$ ,

and finally the dissociation of the superoxo ion. The final trilayer film is very stable and interaction of water with this oxygen terminated structure is unlikely. It is suggested that molecular water is dissociated in one of the previous step, either by attack of Fe or by reaction with dissociated oxygen.

The hydroxyl terminated FeO(OH) film is stable under environmental conditions (air and liquid water), however it breaks after heating to 1000 K in UHV. In contrast, the clean FeO film remains stable in UHV after annealing up to 1000 K [153]. For the non-hydroxylated trilayer Pt-O-Fe-O film, TPD results show that a new desorption peak appears at lower temperature (840 K) in comparison with double layer FeO film, which exhibits a single desorption peak at 1170 K [153]. Similarly, it is expected that OH groups on the hydroxylated trilayer Pt-O-Fe-OH desorb at lower temperature and cause the strong morphology change of the film.

#### 4.4 In situ STM study of FeO(111)/Pt(111) film in aqueous solution

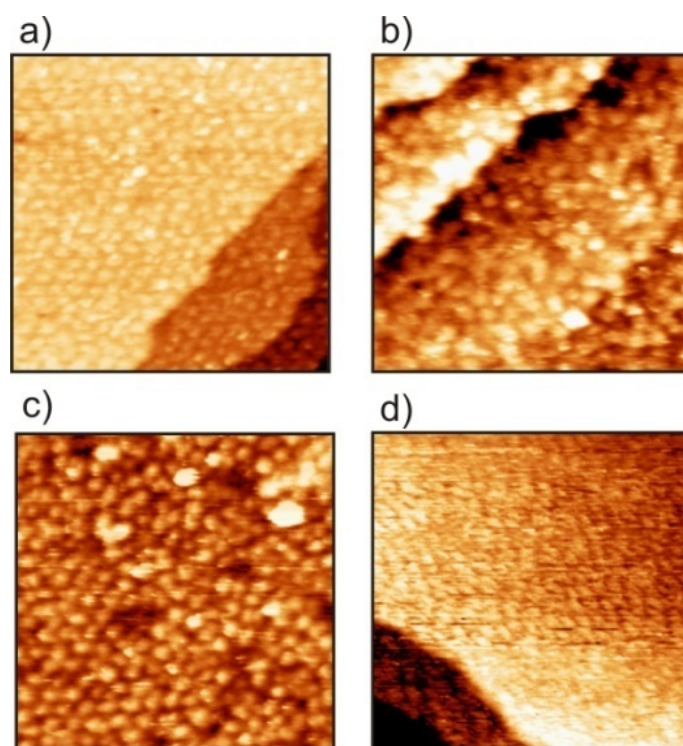


Fig. 4.9. In-situ STM images of FeO films in pH 3 HCl solution (a), pH 10 NaOH solution (b), in 0.1 mM PdCl<sub>2</sub> pH 3 solution (c) and in 2 mM PdCl<sub>2</sub> pH 10 solution (d). All images are 40 nm × 40 nm.

In addition to the studies related to the stability of FeO(111) in air and water, a number of experiments concerning its properties in acidic and basic solutions, as well as in-situ studies

with precursor solutions containing  $\text{PdCl}_2$  were carried out.

Figure 4.9 shows STM images of  $\text{FeO}(\text{OH})$  thin films in different liquids. In pH 3 HCl solution (Figure 4.9a), the STM image displays an ordered surface structure similar to FeO in UHV and FeO(OH) in air. The image of the FeO film in pH 10 NaOH solution (Figure 4.9b) shows less ordered structure similar to that of the FeO film in liquid water. When the FeO film was exposed to pH 3 solution containing 0.1 mM  $\text{PdCl}_2$ , it is still ordered (Figure 4.9c). The pH 3 solution contains  $\text{PdCl}_x(\text{OH})_y^{n-}$  anions, which can adsorb on the FeO surface, which is positively charged at pH 3. However, the structure obtained is found to be similar to the structure of the film in the pH 3 HCl solution as shown in Figure 4.9a. Therefore, unambiguous identification of adsorbed precursor complexes is not possible at this stage. For the film in pH 10 solution containing 2 mM  $\text{PdCl}_2$ , a different image contrast was observed in comparison with the film in blank pH 10 solution. Colloidal nanoparticles of  $\text{Pd}(\text{OH})_n$  are formed at pH 10, which are most probably deposited on the oxide support (see Chapter 5). It is likely that the image contrast seen in Figure 4.9d results from adsorbed colloidal particles. Clearly, further work needs to be done to unambiguously identify adsorbed catalyst precursor by in-situ STM.

#### 4.5 $\text{Fe}_3\text{O}_4(111)/\text{Pt}(111)$ film

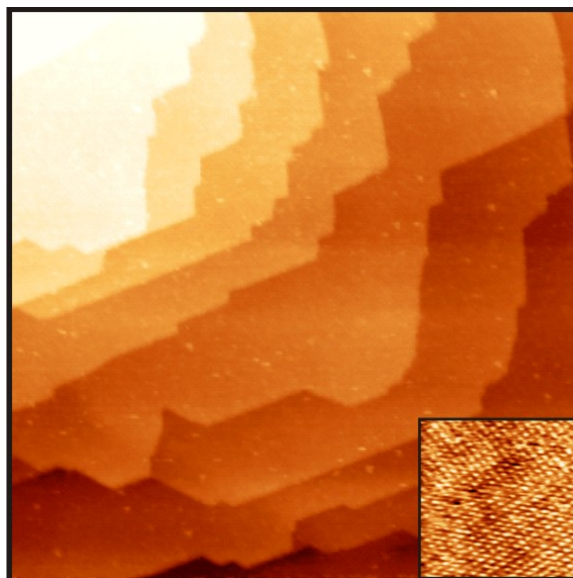


Fig. 4.10. Large scale ( $365 \text{ nm} \times 365 \text{ nm}$ ) STM image and atomically resolved features on a terrace (inset image) ( $10 \text{ nm} \times 10 \text{ nm}$ ) of  $\text{Fe}_3\text{O}_4(111)/\text{Pt}(111)$  film taken in air.  $U_t = -0.05 \text{ V}$ ,  $I_t = 0.2 \text{ nA}$ . The image has not been corrected for instrumental drift and, therefore, the hexagonal lattice is slightly distorted.

STM images taken in air at room temperature of a  $\sim 10$  nm thin  $\text{Fe}_3\text{O}_4(111)$  film grown on Pt(111) are shown in Figure 4.10. The surface morphology displayed in the large scale STM image shows similar features as observed in previous UHV-STM studies with large terraces separated by well-defined step edges [141]. Zooming in on a terrace allows atomic features with a periodicity of 0.5 nm originating from the iron sublattice to be resolved (inset image).

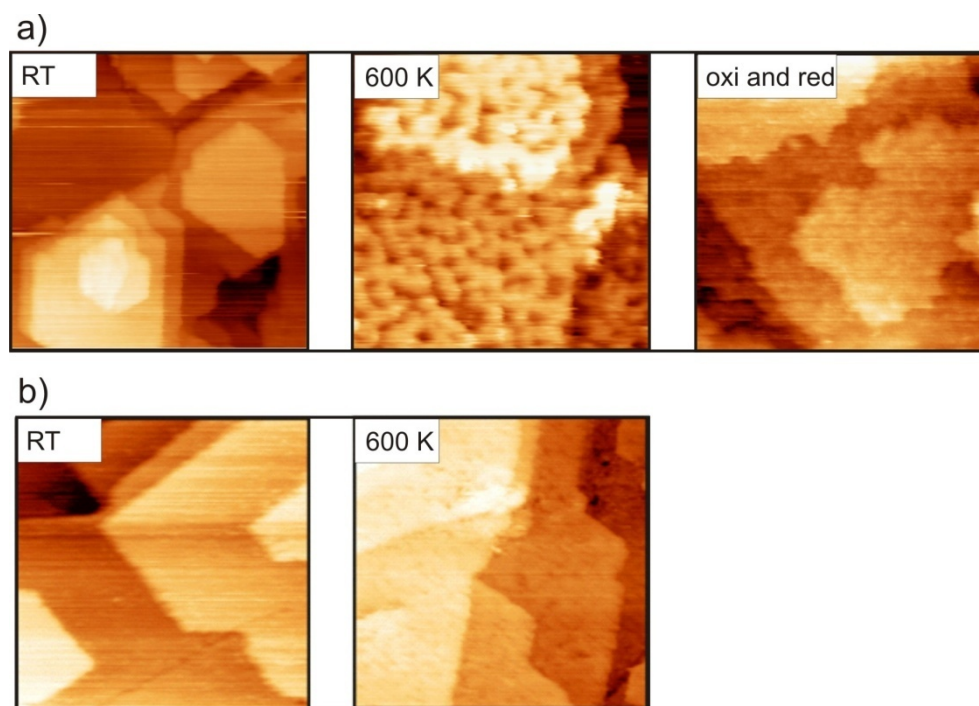


Fig. 4.11. a) STM images of  $\text{Fe}_3\text{O}_4$  films taken in air after in contact with blank pH 1.3 solution for 1 h, after annealing to 600 K in UHV and additional oxidation and reduction treatment, b) STM images of  $\text{Fe}_3\text{O}_4$  films after in contact with blank pH 10 solution for 1 h, after annealing to 600 K in UHV.

Changes in surface morphology of  $\text{Fe}_3\text{O}_4(111)$  films after exposure to different aqueous environments was analyzed with STM. Figure 4.11 shows STM images of the  $\text{Fe}_3\text{O}_4$  surface just after the solution treatment (RT) and after subsequent heating in UHV (600 K). Comparison with Figure 4.10 shows that the surface morphology remains unchanged after exposing the sample to HCl (pH 1.3) or NaOH solution (pH 10) for 60 minutes. Then the sample was heated up to 600 K in UHV, which is the temperature used in the following (see Chapter 5) to decompose the adsorbed Pd complex in vacuum. For the sample exposed to pH 1.3 (HCl) solution, a strong surface modification, interpreted as partial etching, was observed (Figure 4.11a). The surface becomes flat again by oxidation ( $1 \times 10^{-6}$  mbar  $\text{O}_2$ , 600 K, 2 hours) and reduction ( $1 \times 10^{-6}$  mbar CO, 500 K, 1 hour) treatment (Figure 4.11a). The increased

roughness of the  $\text{Fe}_3\text{O}_4(111)$  surface exposed to pH10 (NaOH) solution points also to attack by the solution, albeit to a much lesser extent than the acid solution does (Figure 4.11b).

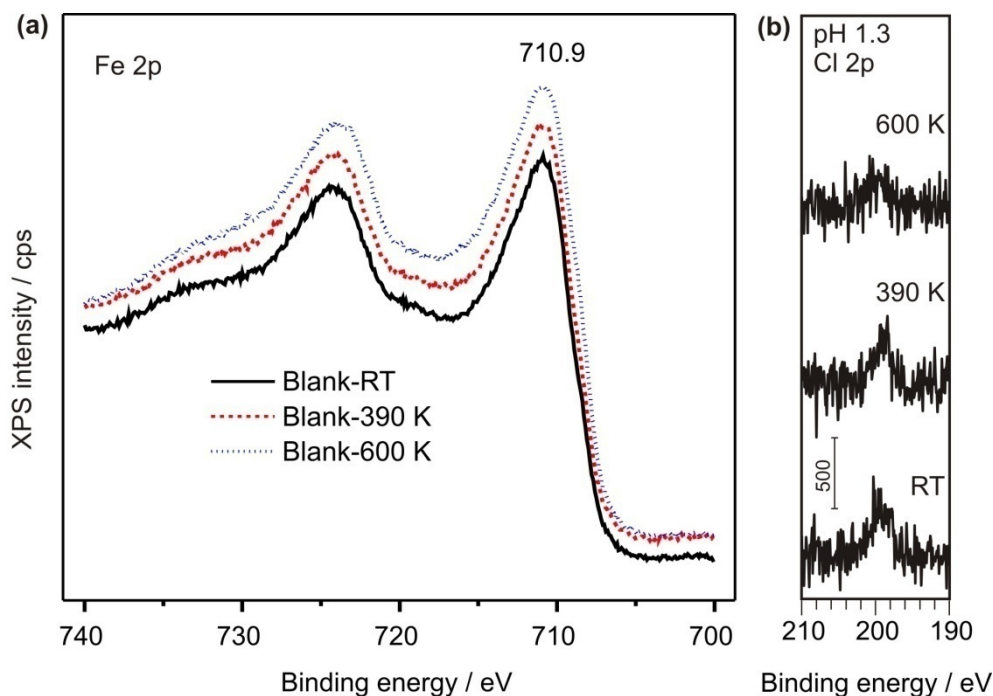


Fig. 4.12. Fe 2p (a) and Cl 2p (b) of XPS for  $\text{Fe}_3\text{O}_4$  sample in contact with pH 1.3 solution and annealing to 390 K and 600 K in UHV.

For the pH 1.3 sample, Fe 2p XPS spectra shown in Figure 4.12a reveal that the oxidation state of Fe does not change during heating to 390 K. However, a slight reduction of  $\text{Fe}_3\text{O}_4$ , characterized by the appearance of a weak shoulder at the lower binding energy side of the main Fe 2p peak, is noted for the sample annealed to 600 K. In addition, XPS shows that chlorine remains adsorbed on the surface after contacting the  $\text{Fe}_3\text{O}_4(111)$  sample with HCl. Heating in UHV results in an almost complete removal of chlorine (Figure 4.12b). It is proposed that the strong surface modification observed after treatment of the  $\text{Fe}_3\text{O}_4(111)$  surface with HCl solution and subsequent heating in UHV results from reactive desorption of adsorbed water and chlorine, leading to partial etching/surface reconstruction. The fact that the surface can be “repaired” by oxidation supports this idea.

For the sample exposed to pH 10 (NaOH) solution, no chlorine was detected on the surface and heating to 600 K leads to only slight surface roughing induced by desorption of water.

Strong adsorption of chlorine with formation of chloride or oxychloride species on the surface of supported catalysts, and its effect on catalytic activity is a topic of considerable

interest in catalysis. For example, formation of chlorides and oxychlorides has been reported for  $\text{Al}_2\text{O}_3$  and  $\text{CeO}_2$  supports when chlorine containing precursors are used [119] [120]. By contrast, interaction of chlorine with  $\text{TiO}_2$  and  $\text{SiO}_2$  has been reported to be rather weak [121]. The XPS results presented above for the interaction of HCl solution with  $\text{Fe}_3\text{O}_4(111)$  suggest that, similar to  $\text{SiO}_2$ , chlorine is only weakly bound to  $\text{Fe}_3\text{O}_4$  and that no oxychloride species are formed.

Finally, it should be mentioned that  $\text{Fe}_3\text{O}_4$  is reported to dissolve in acidic environment, especially in chloride containing solutions [161, 162]. From the observations made in this work, this cannot be directly confirmed. The STM images reported in Figure 4.11 show that flat terraces with well-defined step edges are present after treatment with acidic solution. In addition, no significant decrease of the Fe or O XPS signals, and no concomitant increase of the substrate Pt XPS signals, that would be indicative for reduction of film thickness (by dissolution) was observed. Therefore, it is concluded that the thin  $\text{Fe}_3\text{O}_4(111)$  film used in this work is extremely stable, both in air and under extreme pH conditions.

## 4.6 Summary

The stability and chemical modification of single crystalline  $\text{FeO}(111)$  and  $\text{Fe}_3\text{O}_4(111)$  films grown on  $\text{Pt}(111)$  for different environmental conditions, ranging from exposure to air, to contact with acidic and basic solutions, has been studied. STM, XPS and IRAS results have shown that the  $\text{FeO}$  film transforms into a O-Fe-OH trilayer film upon exposure to air, which is ordered and wets the Pt surface completely. This transformation is driven by the high oxygen pressure. The trilayer film formed in air is stable in water as well as acidic and basic solutions. The film dewets during heating to 1000 K as a result of water desorption.

Similar to  $\text{FeO}(111)$ , the  $\text{Fe}_3\text{O}_4$  film is stable both in acid and basic environment with no sign of morphological transformation. However, partial surface etching was observed after UHV heating, which is caused by reactive desorption of chlorine and water.

# Chapter 5

## Pd deposition on iron oxide films using wet chemical methods

Parts of the results presented in this chapter have been published in:

H.-F. Wang, H. Ariga, R. Dowler, M. Sterrer, H.-J. Freund  
**Surface science approach to catalyst preparation – Deposition of Pd onto Fe<sub>3</sub>O<sub>4</sub>(111) films from PdCl<sub>2</sub> precursor.**  
*Journal of Catalysis*, **2012**, 286, 1.

and

H.-F. Wang, W. E. Kaden, R. Dowler, M. Sterrer, H.-J. Freund  
**Model oxide-supported metal catalysts – Comparison of ultrahigh vacuum and solution based preparation of Pd nanoparticles on a single-crystalline oxide substrate.**  
*Phys.Chem.Chem.Phys.*, **2012**, 14, 11525.

## 5.1 Introduction

Pd catalysts in the form of Pd nanoparticles supported on oxides have a wide range of applications in industrial processes such as hydrogenation reactions for the synthesis of fine chemicals and bulk chemicals, and the oxidation of CO and hydrocarbons in the automobile exhaust. As such, they have attracted a lot of interest in the catalysis community and motivated a huge amount of studies related both, to the elucidation of reaction mechanisms over the catalyst surface, and to the “synthesis” aspect, which deals with finding preparation conditions that finally yield an active, selective and stable catalyst.

Traditionally, supported Pd powder catalysts are prepared using “inert” non-transition metal oxides such as  $\text{SiO}_2$  and  $\text{Al}_2\text{O}_3$  as supports, and with relatively cheap precursor salts ( $\text{PdCl}_2$  and  $\text{Pd}(\text{NO}_3)_2$ ). More recently, these studies have been extended to transition metal oxides such as  $\text{CeO}_2$ ,  $\text{TiO}_2$  and  $\text{Fe}_2\text{O}_3$  to study the influence of metal-support interaction.[119, 163-167] Different precursors have in some studies been used (e.g.  $[\text{Pd}(\text{NH}_3)_4](\text{NO}_3)_2$ ,  $\text{Pd}(\text{azide})$ ,  $\text{Pd}(\text{acac})_2$ ) to elucidate molecular details of the preparation process or to study the influence of the anion.[117, 168]

Model studies on the low Miller index surface planes of Pd single crystals have been reported already in the early days of surface science and are still subject of active research. For example, the adsorption and oxidation of carbon monoxide, decomposition of methanol, or the hydrogenation of alkenes, as well as formation and reactivity of Pd-oxide, have extensively been investigated from UHV to mbar pressure conditions.[169-173] To include metal support interaction, UHV model studies have been extended to Pd nanoparticles supported on flat substrates. Single-crystalline bulk oxide supports such as  $\text{MgO}(001)$  and  $\text{TiO}_2(110)$  were used to study nucleation and growth of Pd nanoparticles and metal-support interaction.[174, 175] Adsorption of gases and catalytic activity over supported Pd has been studied in the groups of Freund and Goodman using thin, single crystalline oxide films as substrates.[47, 176]

The choice to use  $\text{Fe}_3\text{O}_4(111)$  thin films as support for Pd nanoparticles in the present study stems from the rich experience with this system within the group. The surface properties of  $\text{Fe}_3\text{O}_4(111)$  films, the nucleation and growth of Pd particles over the films, as well as particle size effects in adsorption and reactivity of simple gases have in detail been studied over the last years.[177-184] The Pd nanoparticles were prepared in these previous studies by physical vapor deposition and the size of the particles was controlled by the amount of Pd deposited. It is assumed that the structural and electronic properties of the model catalyst prepared

exclusively in UHV are comparable to those exhibited by a technical catalyst prepared by wet chemical methods.

In this chapter, an alternative way to prepare a Pd/Fe<sub>3</sub>O<sub>4</sub> model catalyst system, that uses single-crystalline Fe<sub>3</sub>O<sub>4</sub>(111) films as substrate and wet chemical procedures to apply Pd onto the substrate, will be described. This chapter starts with a short overview of the experimental procedures used for wet chemical deposition of Pd precursors onto single-crystalline oxide substrates. A short section that follows describes initial deposition experiments carried out on FeO(111)/Pt(111) films, and the main part of this chapter is reserved for the Pd/Fe<sub>3</sub>O<sub>4</sub> system, which has been studied in more detail.

## 5.2 Experimental procedure for wet chemical deposition of Pd onto single-crystalline Fe<sub>3</sub>O<sub>4</sub>(111) thin film samples

It has already been mentioned in Sec. 3.5 that preparation procedures developed for porous powder supports cannot straightforwardly be applied to the model oxide surfaces studied here. The main restrictions are the non-porous nature of the flat, single-crystalline oxide films, and the impossibility of vigorous stirring of the precursor-support suspension required in some preparation methods. For this reason, slightly modified preparation procedures that are, however, still closely related to technical applied methods, have been used here. These are:

a) Wet impregnation method, where, by definition, the amount of precursor solution exceeds the pore volume of the support. For the present work, this means that the single-crystalline oxide support is contacted with a precursor solution exhibiting a pH typical for impregnation (in the present case this is pH 1.3) for a certain amount of time.

b) Modified deposition precipitation method. This method is similar to the wet impregnation method under a), except for the different pH of the precursor solution used (pH 10 instead of pH 1.3).

Results for these two preparation methods will in detail be described in Sec. 5.4 and Sec. 5.5. In addition, several experiments with precursor solutions exhibiting pH values between these two extremes are summarized and discussed in Sec. 5.6.

The following experimental steps were carried out: For impregnation with precursor solution the freshly prepared Fe<sub>3</sub>O<sub>4</sub>(111)/Pt(111) sample was transferred via a load lock out of

the UHV chamber. Then, the  $\text{Fe}_3\text{O}_4(111)$  surface was contacted with  $\text{PdCl}_2$  solution at RT for the desired time. The solution was removed and the surface rinsed 4 times with small quantities (3 ml) of ultra-pure water. Rinsing with water was necessary to remove residual precursor solution from the single crystal surface, which could lead to unwanted precipitation of  $\text{PdCl}_2$  in the subsequent drying step. Drying was carried out at RT under a stream of He gas. The sample was inspected with STM in air and subsequently transferred back to the UHV chamber for subsequent treatments and XPS spectra acquisition. Initial treatments in UHV consisted of simple sample heating to elevated temperatures in order to decompose the precursor. After each annealing step, the sample was transferred out of the UHV chamber for STM imaging in air.

In addition, oxidation ( $1 \times 10^{-6}$  mbar  $\text{O}_2$ , 600 K) and reduction ( $1 \times 10^{-6}$  mbar  $\text{CO}$  or  $\text{H}_2$ , 500 K) treatments, representing activation steps typical of technical catalyst preparations, were performed. Results for different reduction procedures will be presented in Chapter 6. It should be noted here that a gas atmosphere of  $1 \times 10^{-6}$  mbar during oxidation (reduction) was sufficient to induce the desired chemical changes of the supported Pd particles, and low enough to avoid transformation of  $\text{Fe}_3\text{O}_4$  into  $\text{Fe}_2\text{O}_3$ , which could occur at elevated temperature under more realistic oxygen partial pressures in the mbar range [138].

For comparison,  $\text{Pd/Fe}_3\text{O}_4$  samples have also been prepared exclusively in UHV by physical vapor deposition.

### 5.3 Initial Pd deposition experiments on $\text{FeO}(111)/\text{Pt}(111)$

$\text{FeO}(111)/\text{Pt}(111)$  was selected for initial experiments regarding Pd deposition from aqueous solution because of its known surface structure and simple preparation. Figure 5.1a shows STM images of  $\text{Pd/FeO}$  samples prepared by exposure of FeO (more precisely to  $\text{FeO}(\text{OH})$ ) to  $\text{PdCl}_2$  solution (0.2 mM, pH 10) directly after removing the solution (RT), and after subsequent heating in UHV to 450 K and 600 K, respectively. After Pd deposition, a low density of randomly distributed particles is imaged (RT). The particle size is 2.4-3.8 nm. With heating to 450 K, more particles appear on the surface and the particle size (2.5-4.5 nm) does not change much. After further heating to 600 K, the particle size increases. In addition, it is noted that the majority of particles is flat and only a few of them appear to be three-dimensional (see also below). At this stage of the thesis, AES was used to obtain chemical information from the samples. The AES spectrum shown in Figure 5.1b was taken from the

sample shown in Figure 5.1a after heating to 600 K and the appearance of the Pd MNN line directly confirms the successful deposition of Pd onto the FeO sample.

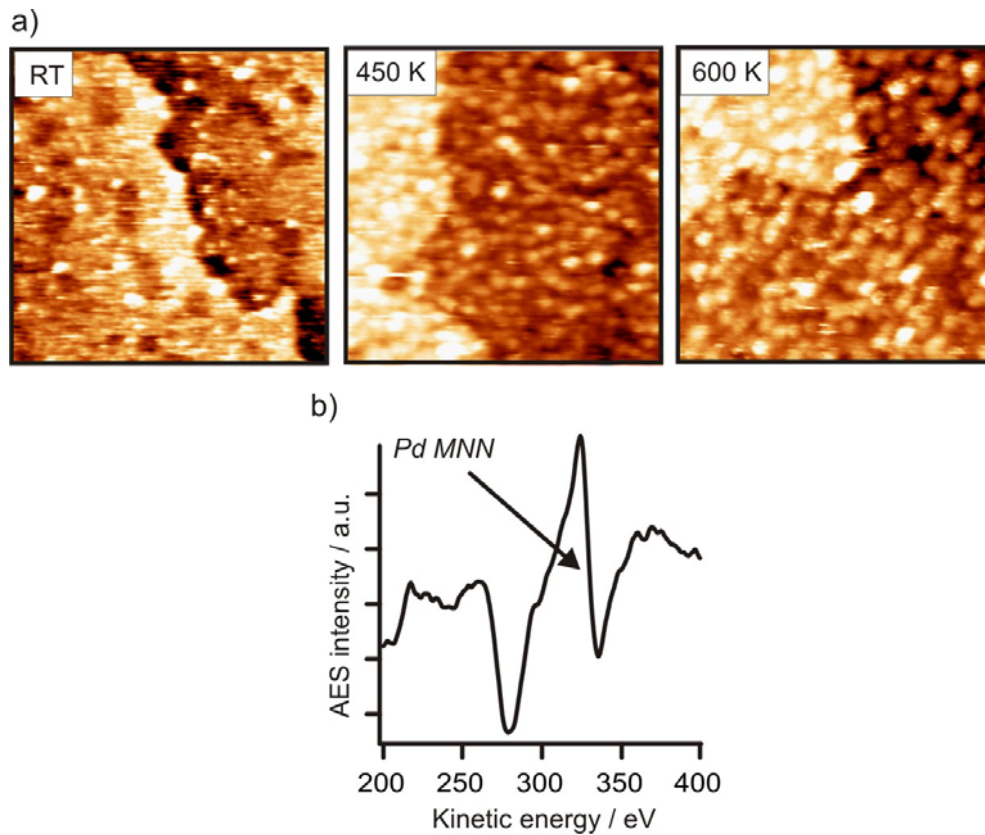


Fig. 5.1. (a) STM images of Pd/FeO samples prepared by Pd deposition from PdCl<sub>2</sub> solution (0.2 mM, pH 10) for 1 h and then heated to different temperature in UHV, (b) a characteristic AES of Pd sample. All images are 100 nm × 100 nm.

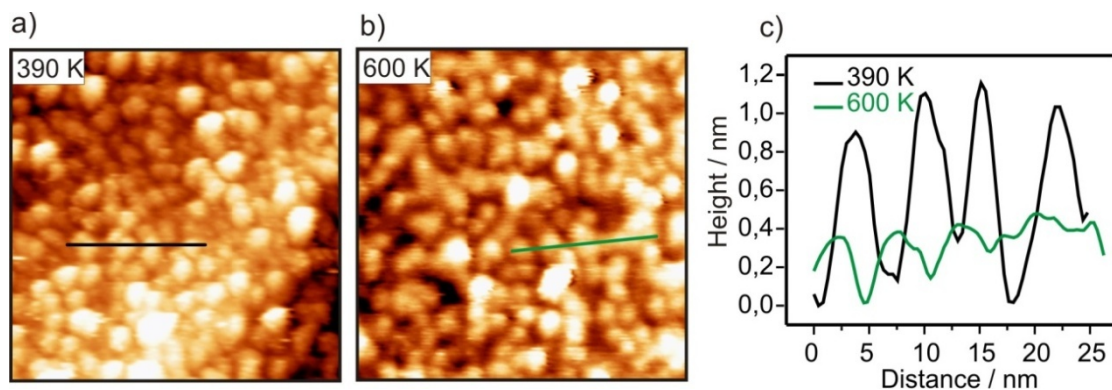


Fig. 5.2. STM images (a and b) with line profile (c) of Pd/FeO samples prepared using pH 10 solutions of 2 mM PdCl<sub>2</sub> for 30 min deposition and then annealing sample at different temperatures in UHV. Both images are 60 nm × 60 nm.

A more obvious change of particle morphology during heating is seen in the STM images taken of FeO that has been exposed to a higher concentrated PdCl<sub>2</sub> solution (Figure 5.2, 2mM PdCl<sub>2</sub>, pH 10). Whereas individual particles can be distinguished after heating to 390 K (Figure 5.2a), the higher annealing temperature (600 K, Figure 5.2b) leads to interconnected particles. As seen from the line scans in Figure 5.2c, the particle size drops significantly during heating from 390 K to 600 K.

The morphology change observed after heating to 600 K indicates a strong interaction of Pd particles with the support. This observation is consistent with a report in the literature that confirmed, using TPD, angle-resolved XPS and STM, that Pd migrates through the FeO film at elevated temperature [185].

These initial deposition experiments with FeO have shown that Pd particles can be obtained via interaction of aqueous phase precursors with a single crystalline oxide substrate and subsequent annealing in UHV. The FeO film is, however, only of limited use in these studies because of the strong influence of the Pt substrate, especially if higher temperatures need to be applied. For this reason, a thick Fe<sub>3</sub>O<sub>4</sub>(111) film is used in the following as substrate and more detailed chemical information will be obtained by XPS instead of AES.

## 5.4 Pd on Fe<sub>3</sub>O<sub>4</sub>(111) – wet impregnation (pH 1)

### 5.4.1 From wet deposition to UHV thermal reduction

For wet impregnation, Pd was deposited onto the Fe<sub>3</sub>O<sub>4</sub>(111) surface by exposing the sample to PdCl<sub>2</sub> solution (15 mM, pH 1.3) for 60 min at room temperature. STM images obtained after removing the solution, washing with water, and drying with Helium at RT show a low density of particles randomly distributed on a flat surface (Figure 5.3, left). Atomic resolution imaging, which can be frequently achieved on terraces of the clean Fe<sub>3</sub>O<sub>4</sub>(111) surface even in ambient air as shown in Figure 3.7, was not possible on a surface exposed to precursor solution. This indicates chemical changes of the surface induced by exposure to the precursor solution, which can intuitively be related to the presence of adsorbed molecular precursor. In real-world catalyst preparation, the adsorbed precursor is transformed into the active metallic compound by drying, followed by calcination in air and subsequent reduction, for example with H<sub>2</sub>. Physically there is sintering during heating and formation of a crystalline solid from the amorphous precursor. Chemically, the precursor is

decomposed. Here we apply heating in a UHV chamber after deposition to decompose the precursor complexes. When the sample was dried at 390 K in UHV, the particle density increased (Figure 5.3, middle). Finally, after heating to 600 K in UHV, particles covered the entire oxide surface (Figure 5.3, right).

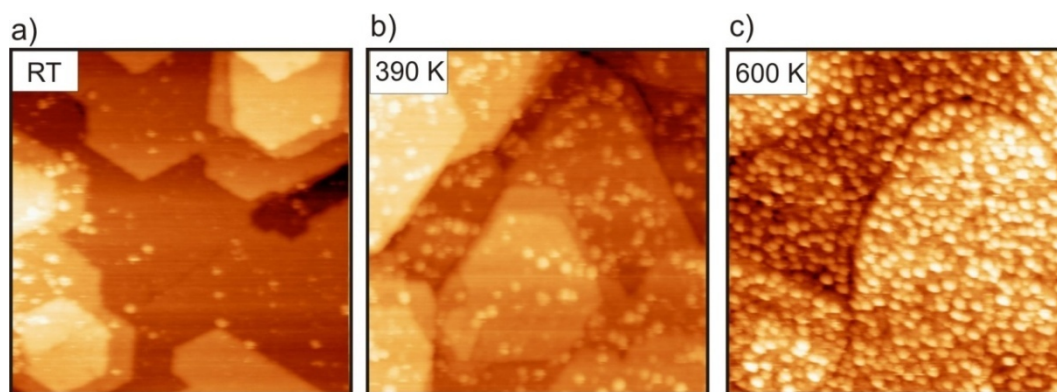


Fig. 5.3. Series of STM images ( $100 \text{ nm} \times 100 \text{ nm}$ ) of  $\text{Fe}_3\text{O}_4(111)/\text{Pt}(111)$  films taken in air after contact with  $\text{PdCl}_2$  (15 mM, pH 1.3) solution (left) directly after removing the solution, (middle) after UHV-annealing at 390 K, and (right) after UHV-annealing at 600 K.

Comparison of Figure 5.3 (left) with the STM image of the  $\text{Fe}_3\text{O}_4(111)$  surface exposed to HCl solution shown in Figure 3.8a, where only flat terraces without any adsorbate are imaged, allows the particles observed at this stage to be attributed to Pd species and not to impurities such as carbon that accumulates on the surface during air exposure. Meanwhile, additional information regarding the nucleation behavior can be deduced from Figure 5.3: STM images obtained directly after impregnation as well as after drying at 390 K show randomly distributed particles on the oxide surface, while they uniformly cover the surface after heating to 600 K. Note that there is no preferential nucleation at surface irregularities such as step edges. This observation provides strong evidence for homogeneous nucleation of Pd particles from a monolayer of adsorbed precursor. The diameter of the particles observed in Figure 5.3 is  $\sim 2 \text{ nm}$  regardless of the pretreatment temperature used in this study showing that 600 K is well below the onset of Ostwald ripening.

The chemical nature of the surface species present at the various stages of sample pretreatment was studied with XPS (Figure 5.4). The spectra obtained directly after removing the solution contain a dominant Pd  $3d_{5/2}$  component at a binding energy (BE) of 337.8 eV, and a second Pd  $3d_{5/2}$  component at 336.2 eV. With increasing temperature a gradual transformation of the high BE component into the low BE component and a shift to lower BE is evident (Figure 5.4a). Upon heating to 390 and 600 K the BE of the first signal shifts from

337.8 to 337.1 eV which is most probably related to partial decomposition of the complex. The second Pd 3d<sub>5/2</sub> signal shifts to 335.7 eV upon heating to 600 K (Figure 5.4a). Furthermore it is observed that the surface chlorine concentration does not change much with thermal treatment as shown in Figure 5.4b (black curve). It is very difficult to eliminate the chlorine only by heating.

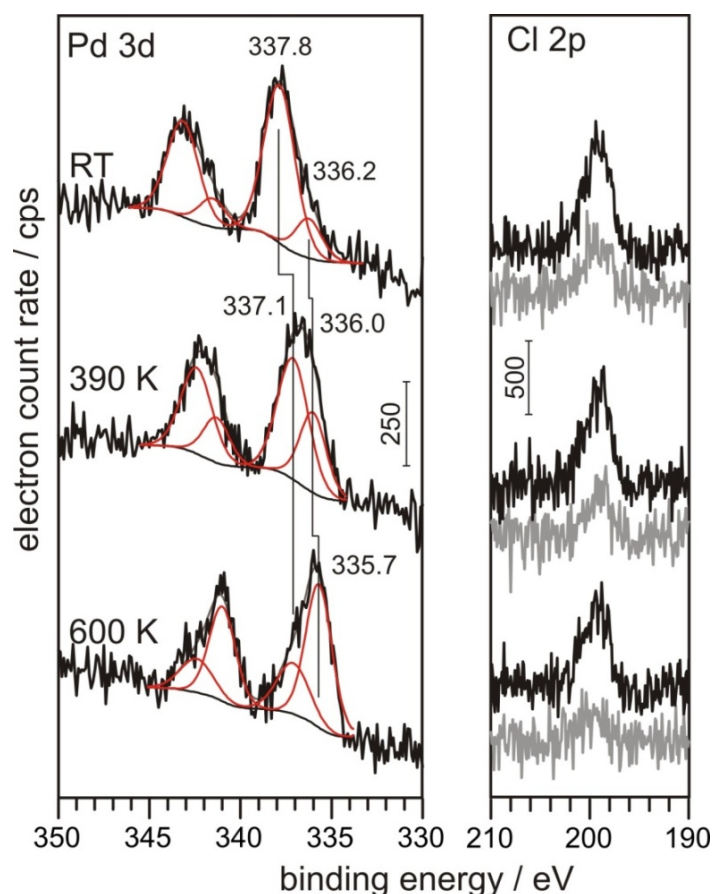


Fig. 5.4. a) Pd 3d, and b) Cl 2p photoemission spectra of  $\text{Fe}_3\text{O}_4(111)$  exposed to  $\text{PdCl}_2(\text{pH } 1.3)$ . The spectra were recorded directly after exposure to  $\text{PdCl}_2$  solution at RT (top), after subsequent annealing to 390 K (middle), and 600 K (bottom). The Cl 2p spectra of a  $\text{Fe}_3\text{O}_4(111)$  sample that has been exposed to HCl (pH 1.3, blank experiment) are shown as gray traces in b).

Comparison with STM images in Figure 5.3 allows the emergence of the low BE peak in XPS to be directly correlated with the abundance of nucleated particles (seen in STM), which increases with pretreatment temperature. Similarly, the loss of the high BE peak reflects the thermal decomposition of the Pd precursor complex. Analysis of the Fe 2p (not shown) and Pd 3d XPS peak intensities shows a clear increase of the Fe/Pd ratio with increasing annealing temperature. This expected trend can be rationalized in terms of weaker attenuation of the Fe

2p emission once Pd particles have been formed after high temperature treatment. This leads to a higher fraction of  $\text{Fe}_3\text{O}_4$  surface exposed to vacuum as compared to the state directly after precursor deposition, where the  $\text{Fe}_3\text{O}_4$  surface is homogeneously covered by Pd precursor complexes. Apart from this qualitative correlation, the measured BE may further be analyzed to determine the chemical identity of the surface species. For the species relevant in this study the Pd  $3d_{5/2}$  BE increases in the order:  $\text{Pd}^0$  (335.2 eV) <  $\text{Pd}^{\delta+}\text{Cl}^-$  <  $\text{Pd}(\text{H}_2\text{O})_x\text{Cl}_y^{n+(-)}$  (336-338 eV)  $\leq$   $\text{PdCl}_2$  (337.8 eV) <  $\text{PdCl}_4^{2-}$  (338.1 eV) [186, 187]. It is well documented that  $\text{PdCl}_4^{2-}$  ions exclusively adsorb during impregnation with acidic  $\text{PdCl}_2$  solution. The high BE component at 337.8 eV observed after impregnation, washing and drying at RT is well below the Pd  $3d_{5/2}$  BE in  $\text{PdCl}_4^{2-}$  and is instead assigned to adsorbed aquochloro complexes,  $\text{Pd}(\text{H}_2\text{O})_x\text{Cl}_y^{n+(-)}$ . In fact, a rough estimate of the elemental distribution from the Pd 3d (Figure 5.4a) and Cl 2p (Figure 5.4b) peak areas gives a Pd:Cl atomic ratio of  $\sim 1:1$ , clearly below the value expected for  $\text{PdCl}_4^{2-}$ . The change of the nature of the adsorbed precursor may be explained by respeciation of  $\text{PdCl}_4^{2-}$  upon adsorption because of the increase of the local pH above the support surface. Such a phenomenon has been observed for the interaction of  $\text{PdCl}_4^{2-}$  with alumina supports when precursor solutions with  $\text{pH} > 3$  were used [95]. Since the pH of the precursor solution (pH 1.3) used in the present experiment is well below this threshold pH (and similar behavior of alumina and iron oxide supports may be expected because of the similar point of zero charge,  $\text{pzc} \approx 8$ , of the two oxides), we exclude the possibility of respeciation because of variation of the local pH, and rather attribute the change of the nature of the adsorbed precursor to ligand exchange during the washing step. Ligand exchange results in particular in the formation of neutral or singly charged aquochloro complexes for which the lateral repulsive interaction on the surface is significantly reduced as compared to adsorbed  $\text{PdCl}_4^{2-}$ . Hence, the possibility to form agglomerates is enhanced and this may account for the observation of the small number of Pd particles on the sample dried at room temperature after the washing step (Figure 5.3a, left).

Binding energy values for the second Pd  $3d_{5/2}$  signal are higher than expected for metallic Pd particles, but considerably lower than in  $\text{PdCl}_2$ . Two effects may contribute in the present study to the observed positive BE shift with respect to bulk Pd: (i) Particle size-dependent screening of the Pd core hole created in the photoemission process, resulting in higher BE's for small particles as compared to bulk Pd [188-191]. (ii) Formation of  $\text{Pd}^{\delta+}$  species by charge transfer to Cl which remains adsorbed on the surface of the particles. While a rigorous separation of the two contributions is not possible, the Cl 2p XP spectra reported in Figure 5.4b provide strong evidence for remaining Cl on the Pd particles. We find that, whereas the

chlorine-containing precursor is gradually transformed into Pd nanoparticles, the surface chlorine concentration is not affected by thermal treatment (Figure 5.4b, black traces). Furthermore, in a blank experiment with the  $\text{Fe}_3\text{O}_4$  surface exposed to HCl (pH 1.3) solution without Pd precursor, the amount of chlorine is considerably less and it could almost completely be removed by heating to 600 K (grey traces in Figure 5.4b). The chlorine detected after heating the Pd-containing sample to 600 K can, therefore, unambiguously be related to the Pd particles. This result is in line with the high desorption temperature ( $\sim 1000$  K) that has been reported for chlorine on Pd surfaces [192].

#### 5.4.2 Interaction of Pd particles with oxide support

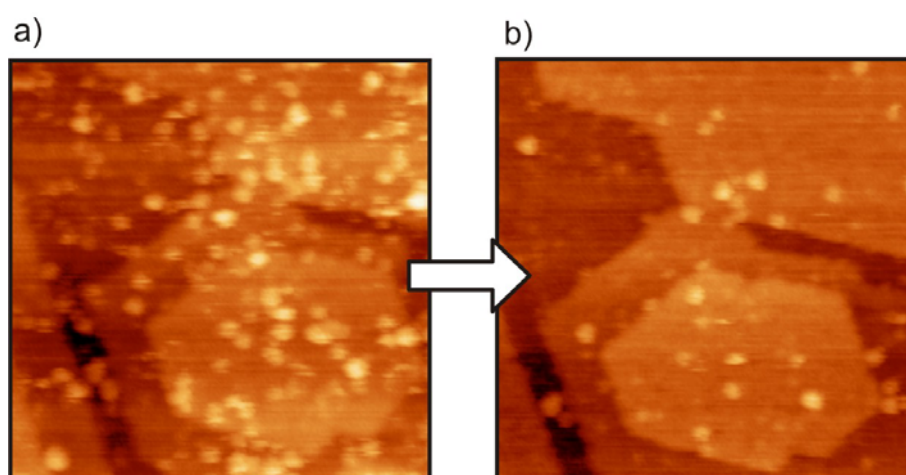


Fig. 5.5. STM images ( $70 \text{ nm} \times 70 \text{ nm}$ ) showing the same area of  $\text{Fe}_3\text{O}_4(111)/\text{Pt}(111)$  exposed to  $\text{PdCl}_2$  (pH 1.3) and annealed to 390 K in subsequent STM scans. The majority of particles present in the left image are only weakly bound to the surface and easily removed by the STM tip.

Interestingly, we observed a strong dependence of the particle-substrate interaction on the pretreatment temperature. The particles on the dried sample (RT, 390 K) could easily be moved under the STM tip by increasing the bias voltage. This is exemplified in Figure 5.5, which presents images of the same area of a sample dried at 390 K in successive STM scans. The majority of small particles present in the left image of Figure 5.5 disappeared after additional scanning (compare with right image of Figure 5.5) either by moving with or collection by the STM tip (increasing the scan area after scanning at high bias revealed that some particles accumulated at the edges of the previous scan window). This suggests that the particles are only weakly bound to the support at this stage of preparation. In contrast, no such

behavior was observed for the sample heated to 600 K indicating a clear enhancement of the particle-support interaction by heating. Similar movement of surface species by STM tip scanning was observed for Pt species deposited on a graphite surface [71]. The reason for the mobility of particles is that the support surface is still covered by adsorbed precursor at this stage (as seen from XPS data in Figure 5.4b), which weakens the particle support interaction.

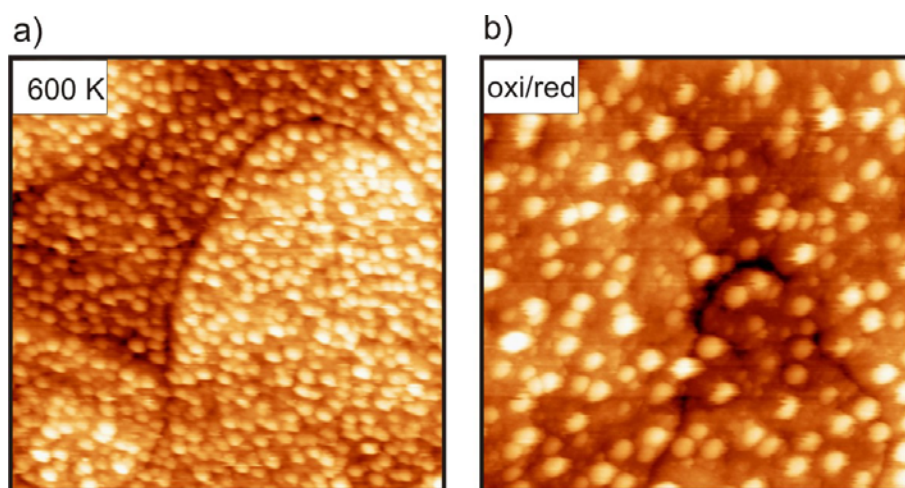


Fig.5.6 a) STM image ( $100 \text{ nm} \times 100 \text{ nm}$ ) of the  $\text{Fe}_3\text{O}_4(111)\text{-PdCl}_2$  (pH 1.3) sample after 600 K annealing (a) and additional oxidation and reduction treatment to remove chlorine (b).

Since chlorine is an unwanted residue of the preparation process, the sample was further subjected to oxidation ( $1 \times 10^{-6}$  mbar  $\text{O}_2$ , 600 K, 5 hours) and subsequent reduction ( $1 \times 10^{-6}$  mbar CO, 500 K, 1 hour). CO was used instead of  $\text{H}_2$  as reducing agent because reduction in  $\text{H}_2$  atmosphere leads to strong chemical modification of both the Pd particles and the  $\text{Fe}_3\text{O}_4$  substrate (refer to chapter 6). XPS showed that Cl was removed from the surface after this treatment. However, the oxidation/reduction treatment resulted in morphological changes as seen in STM: The average Pd particle diameter increased from 2 nm before (Figure 5.6a), to 4 nm after oxidation/reduction (Figure 5.6b). Particle sintering (and chlorine removal) occurred mainly during oxygen treatment, in accord with a recent UHV study which showed that the formation of surface and interface oxides is responsible for Pd sintering on  $\text{Fe}_3\text{O}_4$  under mild oxidation conditions [181]. The facile removal of chlorine observed here is related to the rather weak interaction of the  $\text{Fe}_3\text{O}_4(111)$  surface with HCl, as demonstrated by the XPS results in Figure 5.4b. In this respect, the  $\text{Fe}_3\text{O}_4(111)$  support is similar to silica supports, where chlorine can easily be removed by reduction (in contrast to alumina) [186]. In addition, and as already stated previously, the absence of diffusion limitation and re-adsorption on a flat

substrate as opposed to porous support materials, might influence the retention of chlorine [32].

To summarize, the wet impregnation approach used for preparation of a Pd/Fe<sub>3</sub>O<sub>4</sub> model catalyst was shown to result in small and homogeneously distributed Pd particles on the Fe<sub>3</sub>O<sub>4</sub>(111) surface. The chloride containing precursor complexes can be decomposed into Pd nanoparticles by simple thermal activation in UHV, which does not, however, eliminate chlorine from the surface. The particle-support interaction depends strongly on the activation temperature and environment. An oxidation treatment that is necessary to remove chlorine from the surface results in the formation of surface and interface oxides, leading to particle sintering.

### 5.5 Pd on Fe<sub>3</sub>O<sub>4</sub>(111) – modified deposition-precipitation (pH 10)

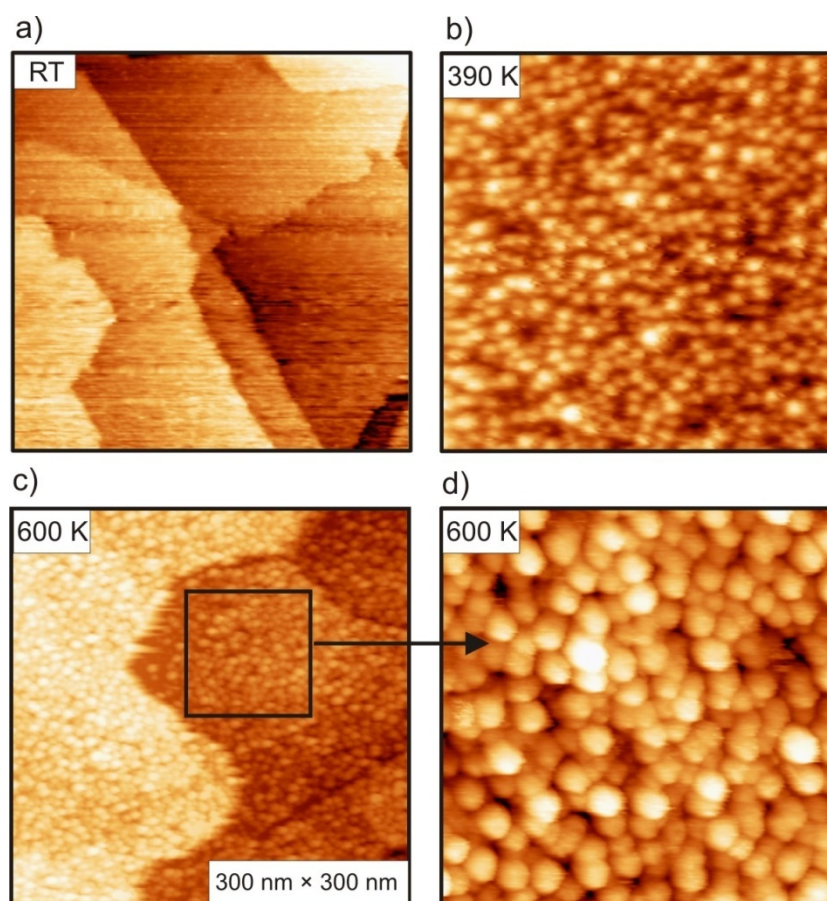


Fig. 5.7. STM images of Fe<sub>3</sub>O<sub>4</sub>(111) films were taken after contacting with PdCl<sub>2</sub> (pH 10) solution for 60 min at RT (a), after UHV-annealing at 390 K (b), after UHV-annealing at 600 K (c and d). All images are 100 nm × 100 nm except (c) which is 300 nm × 300 nm.

Figure 5.7 shows STM images of the Pd/Fe<sub>3</sub>O<sub>4</sub> sample after 60 min deposition from pH 10 PdCl<sub>2</sub> solution. Just after deposition, STM images (RT) of the sample surface showed a flat surface. When the bias voltage was increased, a rough structure was observed but no particle could be imaged. Adsorbed poly-nuclear Pd complexes, if present, could not be resolved with STM under the present experimental conditions (and are therefore assumed to consist of a few Pd atoms at most). After annealing the sample in UHV to 390 K, STM could image homogeneously distributed nanoparticles with an average diameter of 4 nm. When the sample was further annealed to 600 K, large scale images of the sample showed that the terraces and steps are still apparent. In the zoomed-in image, the hemispherical, nanometer-sized particles (~ 6 nm) are clearly seen.

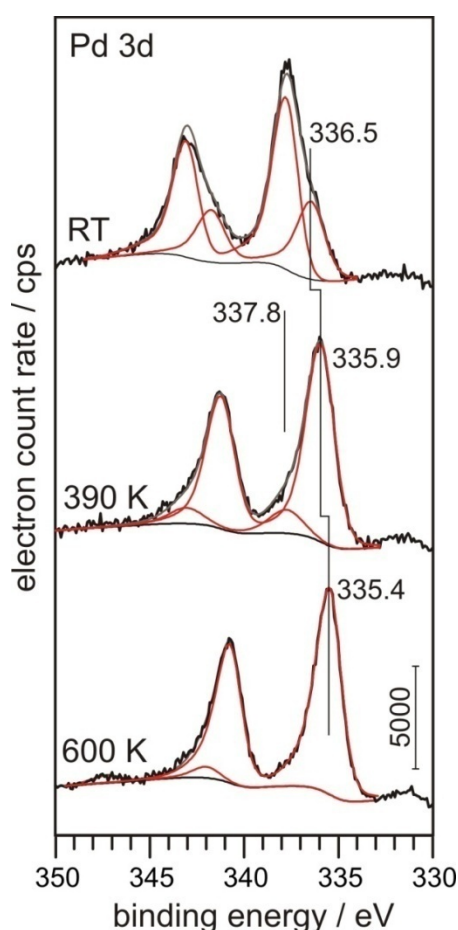


Fig. 5.8. Pd 3d photoemission spectra of Fe<sub>3</sub>O<sub>4</sub> (111) exposed to PdCl<sub>2</sub> (pH 10). The spectra were recorded (top) directly after exposure to PdCl<sub>2</sub> solution at RT, (middle) after subsequent annealing to 390 K in UHV, and (bottom) after further annealing to 600 K in UHV.

Figure 5.8 shows the XPS Pd 3d spectra of the pH 10 sample. Just after Pd deposition (RT), the spectra obtained contain a dominant Pd 3d<sub>5/2</sub> component with a binding energy (BE) of

337.8 eV and a second component at 336.5 eV. Because of the absence of a chlorine peak in XPS, the Pd species present on the surface can be assigned to oxidic species. Indeed, the BE values observed here are in the range of values reported for Pd(OH)<sub>2</sub> (337.4 eV) and PdO (336-337 eV). After drying at 390 K, the high BE component has transformed into the low BE component at 335.9 eV. Pd(OH)<sub>2</sub> precursor complexes are almost fully converted to Pd oxide particles at this stage. The peak of Pd 3d<sub>5/2</sub> shifts to 335.4 eV after 600 K annealing. This binding energy is consistent with the value for metallic Pd. While Pd oxide is reduced to metallic Pd, there is particle sintering, as shown by STM. Sintering is probably due to the weak interaction of PdO with the iron oxide support [181].

The preparation method employed here resembles in many aspects the deposition-precipitation approach reported by Haruta for the preparation of Au/TiO<sub>2</sub> catalysts starting from acidic HAuCl<sub>4</sub> solution and adjustment of the pH to 7-10 by NaOH or Na<sub>2</sub>CO<sub>3</sub>. [124] As mentioned by Louis et al., this procedure does, however, not strictly correspond to deposition-precipitation because it is performed at constant pH and with experimental parameters where precipitation of Au-hydroxide is not favorable. [126] Instead, a grafting reaction involving hydroxyl groups of the support and the solution complexes has been suggested to be the initial step in the preparation. A similar mechanism, i.e., hydrolytic adsorption of Pd chloro-hydroxo complexes at hydroxyl groups of the substrate, can be envisaged for the interaction of the alkaline Pd precursor solution with the Fe<sub>3</sub>O<sub>4</sub>(111) substrate. If this is the only adsorption route for Pd, the Pd uptake would be limited by the concentration and availability of surface OH groups (and would correspond to less than one monolayer taking steric factors into account), as discussed in the case of Au on TiO<sub>2</sub>. However, the high Pd coverage obtained in the present experiment (Figure 5.7) indicates that additional processes take place, such as the adsorption of colloids present in the solution.

In several recent reports that dealt with the preparation of supported Pd catalysts using oxidic Pd colloids obtained by hydrolysis of Pd<sup>2+</sup> solutions as precursor, particular emphasis was put on the characterization of the colloidal precursor state. [96, 100, 193, 194] The results of these studies can be summarized as follows: The average particle size as obtained from electron microscopy images of colloids deposited on carbon and oxide supports is in the range of 1-2 nm. [96, 100, 194] Microscopically, the colloids are reported to consist of [Pd(OH)<sub>2</sub>]<sub>n</sub> filaments coiled up to spherical particles. [194] The native colloids are X-ray amorphous but exhibit some degree of crystalline after deposition onto a support. Adsorbed [Pd(OH)<sub>2</sub>]<sub>n</sub> precursor can be easily transformed into crystalline PdO by drying.

The results of UV-Vis, STM and XPS for Pd deposition onto the single crystalline  $\text{Fe}_3\text{O}_4(111)$  surface presented in Figure 3.2, Figure 5.7 and Figure 5.8 are in agreement with these findings. Although the colloidal nature of the precursor solution is readily deduced from the UV-Vis spectrum, we did not observe any specific particles on the freshly prepared sample surface by STM. This is probably due to the amorphous nature and the homogeneous dense packing of the colloids on the surface. The XPS results provide, however, direct information about the presence of Pd species and their chemical nature. The reported binding energies of 337.8 eV and 336.5 eV are in agreement with the presence of Pd-hydroxide and Pd-oxide species after adsorption. Similar values have been obtained for polymer stabilized  $\text{PdO}_x\text{H}_y$  particles deposited on carbon supports [100]. By drying at 390 K in UHV, the BE of the Pd species shifts to 335.9 eV, which is consistent with decomposition of the majority of the hydroxide precursor to PdO. Under the preparation conditions used here, the resulting PdO particles cover the entire surface. Further heating to 600 K leads to reduction to metallic Pd accompanied by particle sintering. Thermal decomposition of unsupported PdO powder is reported to occur in steps between 400 K and 750 K in UHV conditions.[195] A recent EXAFS study of thermal reduction of PdO on high surface area  $\text{SiO}_2\text{-Al}_2\text{O}_3$  found that reduction of PdO to Pd was only partial at 673 K, but complete at 873 K.[196] It should be noted that the reduction temperature depends on the nature of the support [197] and that  $\text{Fe}_3\text{O}_4$ , because of its redox properties and high conductivity, may strongly aid the reduction process, resulting in this rather low PdO decomposition temperature.

To summarize, the results in this section demonstrate that high loadings of Pd can be applied to the  $\text{Fe}_3\text{O}_4(111)$  surface by deposition from alkaline  $\text{PdCl}_2$  precursor solution. By hydrolysis of the Pd chloro complexes, polynuclear Pd-hydroxo-complexes are formed in solution and are chemically anchored to the surface during exposure of the support to the precursor solution. Unfortunately, STM was not able to resolve individual polynuclear complexes. Facile thermal decomposition of the hydroxo complexes is possible, with small PdO particles formed in an intermediate decomposition step. The use of the alkaline precursor solution has the advantage over the acidic solution of easier removal of chlorine (simply by washing). However, the PdO species formed during decomposition interact only weakly with the support surface and, hence, strong sintering occurs at high decomposition temperature.

## 5.6 Effect of solution pH

Solutions of PdCl<sub>2</sub> adjusted to five different pH values (from pH 1.3, pH 1.6, pH 2.5, pH 4.7 to pH 10) but the same concentration (5 mM) were applied to prepare Fe<sub>3</sub>O<sub>4</sub>(111)-supported Pd in order to investigate the effect of precursor speciation on metal loading and distribution. Similar to the pH 1.3 and pH 10 solution described above, no Pd particles could be observed with STM on any of the samples directly after deposition. The Pd 3d XPS spectra, however, clearly indicate that Pd was adsorbed on the surfaces (Figure 5.9a; only spectra for pH 1.6, pH 2.5 and pH 4.7 samples are displayed). A summary of the XPS results for all precursor solutions investigated is presented in Table 2. The Pd 3d XPS spectra were fitted again with

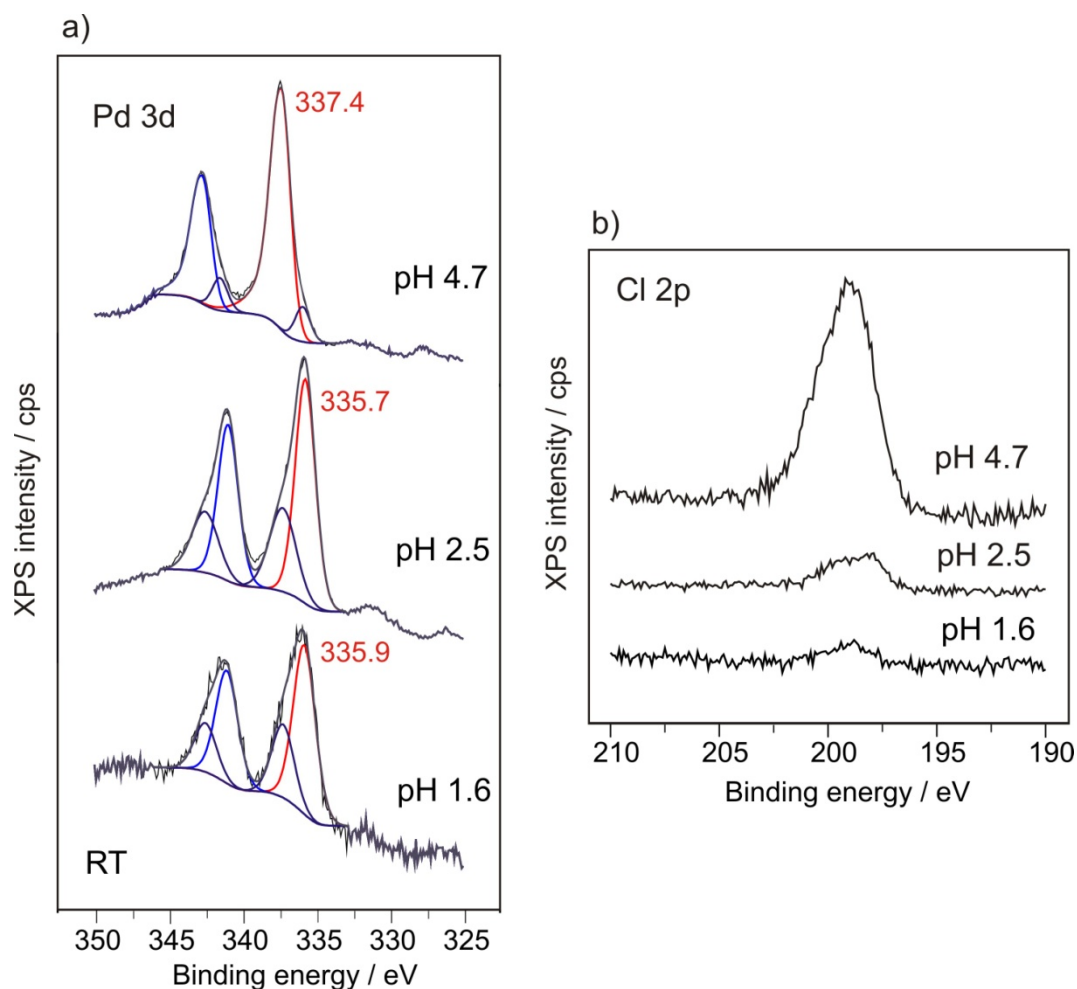


Fig. 5.9 Pd 3d XPS (a) and Cl 2p XPS (b) of Fe<sub>3</sub>O<sub>4</sub> samples just after Pd deposition from three different pH solutions, pH 1.6, pH 2.5 and pH 4.7.

two components. Starting at low pH, a gradual decrease of the intensity ratio of high BE to low BE component is evident up to pH 2.5. Interestingly, this trend is reversed for pH 4.7,

where predominantly the high BE component is formed. In parallel, a strong increase of the amount of adsorbed Cl (sum of Cl contained in the precursor and Cl adsorbed from solution) is seen up to pH 4.7.

Table 2

XPS data of Pd 3d<sub>5/2</sub> and Cl 2p of Pd/Fe<sub>3</sub>O<sub>4</sub> samples prepared using solutions of different pH of PdCl<sub>2</sub>.

XPS \ pH		pH 1.3	pH 1.6	pH 2.5	pH 4.7	pH 10
Pd 3d <sub>5/2</sub> (eV)	RT	337.8 /336.2 (> 1)	337.4/335.9 (< 1)	336.8/335.6 (< 1)	337.4/335.8 (> 1)	337.8/336.5 (> 1)
	390 K	337.1/336.0 (> 1)	337.4/335.7 (< 1)	336.8/335.6 (< 1)	336.8/335.5 (< 1)	337.8/335.9 (< 1)
	600 K	337.1/335.7 (< 1)	337.4/335.5 (< 1)	336.4/335.5 (< 1)	335.4	335.4
Cl 2p	RT	Yes	Yes	Yes	Yes	No
	600 K	Yes	Yes	Yes	No	No

The decomposition of the precursor and the formation of Pd particles have subsequently been studied with XPS and STM. With increasing heating temperature in UHV, the high BE Pd 3d<sub>5/2</sub> component gradually transforms into the low BE component for all pH values as shown in Table 2. After annealing at 600 K, while pH 4.7 and pH 10 samples show a metallic Pd state according to the Pd peak position, the Pd 3d<sub>5/2</sub> peaks of all other pH samples still have one component at higher binding energy. XPS of Cl shows that these samples still have chlorine on the surface.

Figure 5.10 (a-e) shows STM images of Pd samples taken after annealing to 600 K in UHV. For the pH 1.3 sample, a low density of particles with a diameter of about 2 nm was observed on the surface. The particle density and particle size increases up to pH 2.5. It is noted that up to this pH the particle size distribution is very uniform and the particles stay rather small although the loading significantly increases from pH 1.3 to pH 2.5. By contrast, a very high loading is obtained with the pH 4.7 precursor solution. This sample contains much larger particles (7-11 nm) with a broad particle size distribution. For pH 10, the loading and size of particles decreases again and the particle size distribution is uniform. The dependence of the Pd particle size on the pH of the precursor solution is summarized in Figure 5.10f. It is obvious that very low pH produces small sized Pd particles while the high pH gives relatively large particles (this correlates with the Pd loading obtained with the various pH solutions). It

is also clearly seen from STM images that homogeneously distributed Pd particles with a narrow size distribution are formed on  $\text{Fe}_3\text{O}_4(111)$  at low and high pH. However, at intermediate pH values, for example pH 4.7, not only large particles were obtained, but a wide distribution of particle sizes was observed.

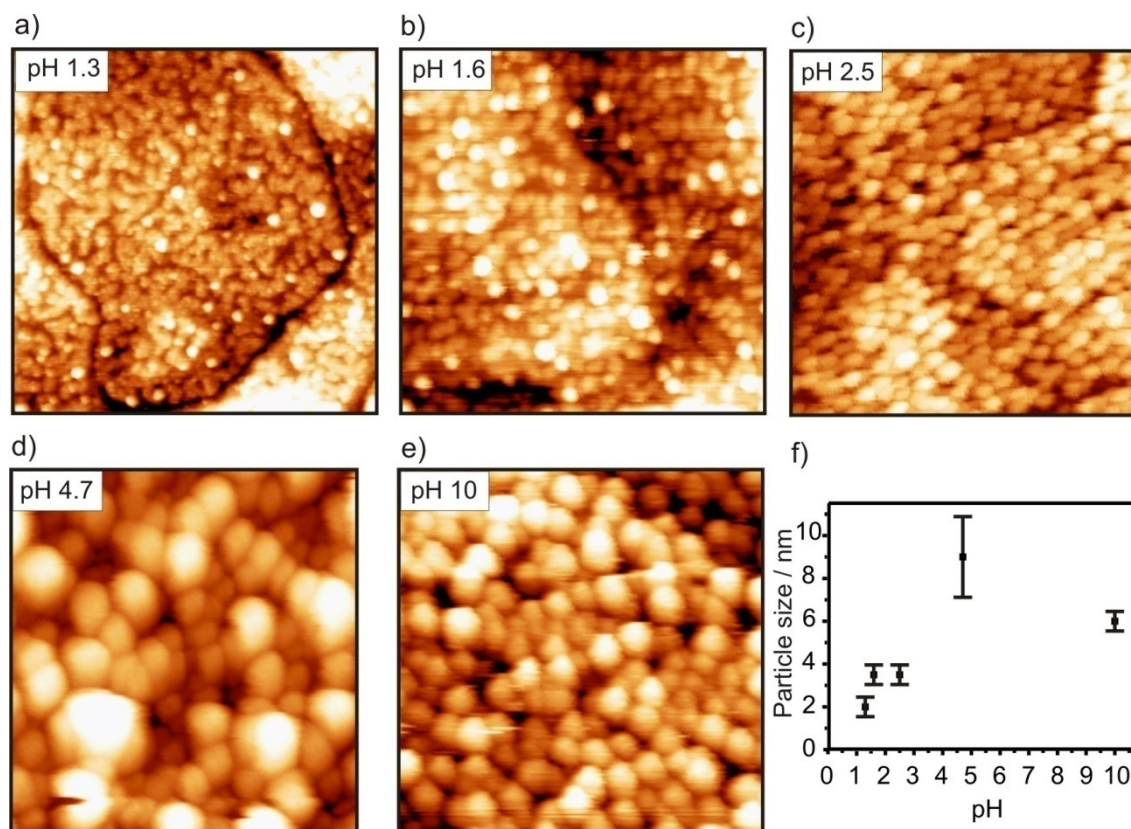


Fig. 5.10. STM images ( $75 \text{ nm} \times 75 \text{ nm}$ ) of Pd/Fe<sub>3</sub>O<sub>4</sub> samples prepared using different pH values of the precursor solution (5 mM PdCl<sub>2</sub> solution, 0.016 M Cl<sup>-</sup>) followed by annealing at 600 K in UHV. f) The dependence of Pd loading and particle size on solution pH.

The UV-Vis spectra in Figure 3.2 indicate that solutions with pH from 1.3 to 2.5 contain Pd complexes such as  $[\text{PdCl}_4]^{2-}$ ,  $[\text{PdCl}_3(\text{H}_2\text{O})]^-$ , and  $[\text{PdCl}_3(\text{OH})]^{2-}$ . In this pH range, the Pd precursor anions are attracted by the positively charged oxide surface (PZC of Fe<sub>3</sub>O<sub>4</sub>  $\sim 6.5$ ) and the interaction is probably electrostatic in nature. Among all the samples, the loading is lowest for pH 1.3 as seen from STM images in Figure 5.10. In the literature, the low loading of noble metal at very low pH is often explained by the decrease of the equilibrium adsorption constant as an effect of high ionic strength of low pH solution [107]. However, the pH 1.3 solution prepared here has a similar ionic strength as the pH 2.5 solution, and, although the ionic strength is similar, a much higher loading was obtained for the latter sample. Therefore,

ionic strength seems not to be the reason for the low loading of the pH 1.3 Pd sample. Alternatively, competitive adsorption of chloride or adsorption modes other than electrostatic adsorption might have an effect. Competitive adsorption of chloride, which is expected to be more pronounced at lower pH since the surface potential is more positive, leads to screening and, therefore, less adsorption of Pd complexes. However, the effect of competitive adsorption of chloride cannot be quantified here, because the Cl XPS signal contains both Cl in the adsorbed complex and chloride adsorbed from solution, and the separation of the two contributions is not easy. A second alternative explanation for the higher loading obtained with the pH 2.5 solution is a change in adsorption mode, from electrostatic adsorption at pH 1.3, to chemical bonding (grafting) at pH 2.5. Both, the different speciation of Pd complexes in solution (reflected also in the Pd 3d binding energies of the adsorbed complexes) and a change of the protonation state of surface OH groups with increasing pH could lead to a stronger bonding and, hence, more adsorbed Pd complexes at pH 2.5 as compared to pH 1.3.

According to the UV-Vis spectra (Figure 3.2), PdCl<sub>2</sub> solutions of pH 4.7 and pH 10 contain colloidal particles (polynuclear Pd complexes) in addition to monomeric Pd species. The high loading obtained for these two precursor solutions is explained by the combined effect of colloidal particle formation in solution and availability of surface hydroxyls. Close to the PZC, the neutral OH groups present on the surface are involved in hydrolytic adsorption of solution complexes, leading to strongly bound precursor on the surface. The large amount of chlorine detected on the sample exposed to pH 4.7 precursor solution results from Cl ligands in the polynuclear Pd complexes at this pH, where hydrolysis is not complete. Interestingly, thermal treatment at 600 K in UHV is sufficient to remove all Cl from this sample, in contrast to the samples prepared at lower pH (see Table 2). Obviously, complete decomposition of the precursor is more facile at higher loading.

To summarize, the results presented in this section have shown how the solution pH affects the loading as well as size and distribution of supported Pd nanoparticles on Fe<sub>3</sub>O<sub>4</sub>(111). Small Pd particles with uniform size distribution are obtained when precursor solutions with low pH are applied. The sample prepared by exposure of Fe<sub>3</sub>O<sub>4</sub>(111) to pH 2.5 PdCl<sub>2</sub> precursor solution represents a good compromise if both loading and particle size are important. High Pd loadings are obtained with precursor solution of pH 4.7 and pH 10 as a result of deposition of colloidal particles.

### 5.7 Morphological comparison with PVD Pd/Fe<sub>3</sub>O<sub>4</sub>(111)

As shown in the section 5.5, deposition of Pd from a colloidal, alkaline Pd precursor solution on Fe<sub>3</sub>O<sub>4</sub>(111) followed by thermal reduction at 600 K in vacuum produces a model catalyst of supported metallic Pd nanoparticles. This surface is free of any residues from the precursor solution (Na<sup>+</sup>, Cl<sup>-</sup>) and can, therefore, be directly compared to a model Pd/Fe<sub>3</sub>O<sub>4</sub>(111) surface prepared exclusively in UHV by physical vapor deposition. In this section, the morphology and the size distribution of Pd particles on Fe<sub>3</sub>O<sub>4</sub>(111) obtained (1) by PVD of different amounts of Pd (0.5 Å, 2 Å, 4 Å), and (2) by interaction with the Pd solution for various times (10 min, 30 min, 60 min), are compared. Pd coverage and interaction times have been chosen to allow direct comparison of Pd particles obtained by PVD and solution deposition. A summary of the results is presented in Figure 5.11, where representative STM images of different coverage of Pd obtained by PVD (a-c) and by solution treatment (d-f) are shown, and in Figure 5.12, where the particle density (a) and the particle size distributions (b-d) determined from these (and other) images are presented.

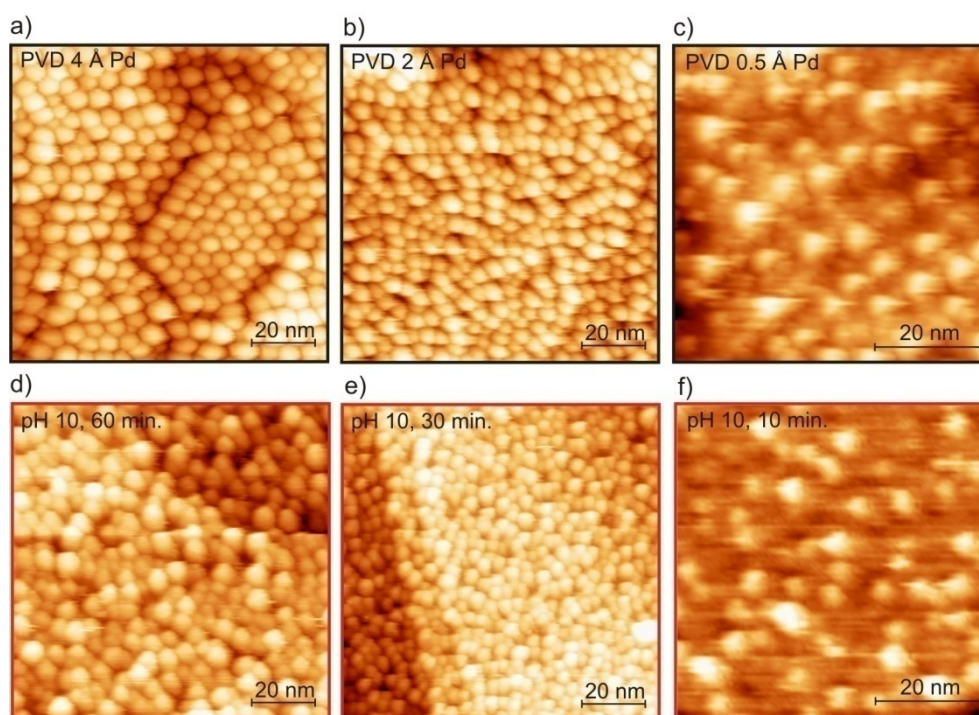


Fig. 5.11. STM images of Pd particles formed on Fe<sub>3</sub>O<sub>4</sub>(111) by PVD with coverage of a) 4 Å, b) 2 Å and c) 0.5 Å, and after contact with pH 10 Pd<sup>2+</sup> precursor solution for d) 60 min, e) 30 min, and f) 10 min. and subsequent thermal reduction at 600 K in UHV. All samples were annealed to 600 K prior to STM imaging. Image size: a), b), d), e): 100 nm x 100 nm, c), f): 60 nm x 60 nm.

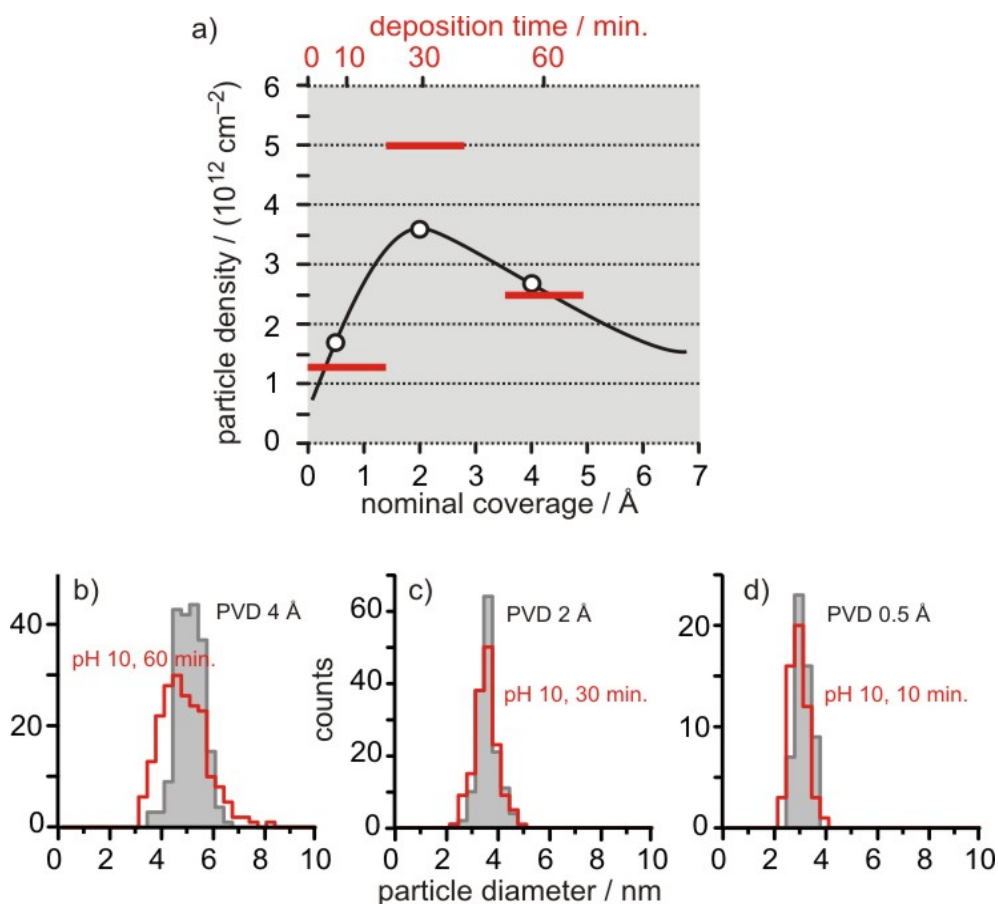


Fig. 5.12. a) shows the particle density of Pd particles for the various preparations (black: PVD; red: precursor solution) and b), c) and d) represent the particle size distributions of samples (PVD 4  $\text{\AA}$ /precursor 60 min), (PVD 2  $\text{\AA}$ /precursor 30 min) and (PVD 0.5  $\text{\AA}$ /precursor 10 min), respectively as shown in Figure 5.11.

The results for PVD Pd on  $\text{Fe}_3\text{O}_4(111)$  are in general agreement with previous studies [198], showing homogeneous distribution of particles across the surface and uniform particle size. The average particle size for the three cases studied here is 3 nm (0.5  $\text{\AA}$ ), 3.6 nm (2  $\text{\AA}$ ) and 5.2 nm (4  $\text{\AA}$ ), respectively, and a maximum particle density is reached after deposition of a nominal amount of 2  $\text{\AA}$  Pd. Slight differences compared to the previous study [198] result from different deposition temperature and deposition rate. Comparison with the STM images (Figure 5.11d-f) and the respective particle density and size distribution (Figure 5.12 a-d) obtained from the samples prepared from solution reveals that two preparation procedures yield qualitatively very similar supported Pd particles in terms of their morphological properties. However, two details require further discussion. Firstly, the maximum particle density obtained in the solution experiment exceeds that of the UHV experiment (Figure 5.12a). And secondly, a deviation from the normal particle size

distribution is observed for the sample prepared by exposure to Pd precursor solution for 60 min. (Figure 5.12b), which is also apparent from visual comparison of the STM images in Figure 5.11a and 5.11d. As discussed in the following, these differences can be traced back to different support functionality (UHV clean vs. exposed to solution) rather than to the different nature of the precursor (single atoms vs. solution complexes).

Exposure of  $\text{Fe}_3\text{O}_4(111)$  to alkaline solution leads to hydroxylation of the surface. Hydroxyl groups are actively involved in the adsorption of precursor complexes from solution and determine to a great extent the nucleation density of particles. The higher particle density obtained in the solution experiment compared to the UHV experiment is, therefore, attributed to the larger abundance of nucleation centers under these conditions. A strong influence of hydroxyls on metal nucleation and sintering has recently been demonstrated for Au/MgO and Au/TiO<sub>2</sub> model systems [199, 200]. In addition, partial dehydroxylation induces roughening of the  $\text{Fe}_3\text{O}_4(111)$  surface during thermal treatment as shown in Chapter 4. Accordingly, the presence of a variety of adsorption sites exhibiting different interaction with Pd can strongly influence growth and sintering of Pd particles at elevated temperature. In order to corroborate this statement experimentally, a  $\text{Fe}_3\text{O}_4(111)$  surface has been exposed to NaOH (pH 10) solution to achieve a support functionality comparable to the one of the solution deposition experiment. Subsequently, Pd was deposited onto this chemically modified surface in UHV by vapor deposition.

An STM image of Pd particles that formed after PVD of 4 Å Pd on the chemically modified  $\text{Fe}_3\text{O}_4(111)$  surface is shown in Figure 5.13a. Comparison with Figure 5.11a and Figure 5.11d reveals that the surface morphology of the sample prepared by evaporation of Pd onto the chemically modified surface is qualitatively similar to the one obtained by precipitation of Pd-hydroxide (Figure 5.11d). This result is confirmed by Figure 5.13b, showing that essentially identical particle size distributions are obtained for these preparations (solid blue line: 4 Å Pd on chemically modified  $\text{Fe}_3\text{O}_4$ ; dashed red line: Pd/ $\text{Fe}_3\text{O}_4$  obtained by 60 min. exposure to precursor solution), and which exhibit the same characteristic deviation from the normal size distribution of the UHV Pd/ $\text{Fe}_3\text{O}_4(111)$  sample (dashed gray line). It is interesting to note that this deviation is only observed for the sample with the highest Pd coverage (60 min. deposition time, see Figure 5.11), where agglomeration effects play a role as indicated by the reduced particle density compared to the maximum particle density exhibited by the sample obtained after 30 min. exposure to precursor solution (Figure 5.12a). This finding can be regarded as a corroboration of the existence of adsorption sites exhibiting different adhesion

for Pd on the chemically modified  $\text{Fe}_3\text{O}_4(111)$  support leading to more heterogeneous sintering of Pd particles as in the case of a UHV-clean support.

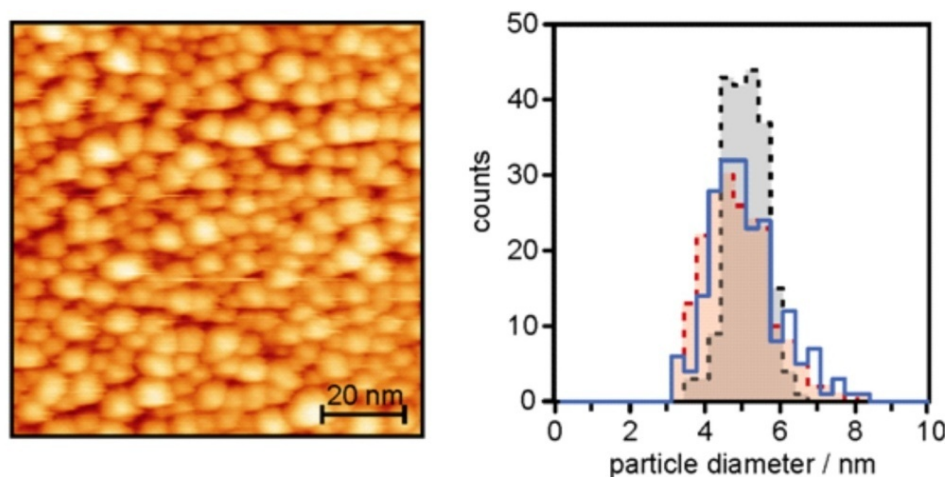


Figure 5.13. a) STM image ( $100 \times 100 \text{ nm}^2$ ) of PVD Pd on  $\text{Fe}_3\text{O}_4(111)$  chemically modified by exposure to pH 10 NaOH solution. The sample was heated to 600 K in UHV prior to STM imaging. b) Particle size distribution of Pd particles formed by PVD on clean  $\text{Fe}_3\text{O}_4(111)$  (black), interaction with Pd precursor solution for 60 min. (red), and PVD of Pd on a  $\text{Fe}_3\text{O}_4(111)$  surface that has been exposed to pH 10 NaOH solution (blue).

In summary, comparison of  $\text{Fe}_3\text{O}_4(111)$ -supported Pd nanoparticles prepared either by Pd vapor deposition in UHV or precipitation of Pd-hydroxide from solution reveals that the overall morphological properties are qualitatively very similar. Slight differences in maximum particle density and sinter behavior can be explained by modification of the interfacial properties of  $\text{Fe}_3\text{O}_4(111)$  by functionalization with hydroxyl groups. The nature of the precursor seems to play only a minor role.

## 5.8 Summary

Real supported catalysts are usually characterized after high temperature calcination. Here, we have studied the stability of local structure and monitored the evolution of the interfacial deposited metal complex during the heating process with a combination of STM and XPS to obtain both morphological and chemical information of the early stages of catalyst preparation. The effect of solution pH on Pd loading, particle size and distribution, and the Pd speciation in solution and on the surface during preparation has been studied. Homogeneously distributed Pd particles with narrow size distribution are formed on  $\text{Fe}_3\text{O}_4(111)$  after

---

deposition from low (pH 1-3) and high pH (e.g. pH 10) of PdCl<sub>2</sub> solutions. Chloride on the catalyst surface induces the weak particle-support interaction and can be eliminated by oxidation and reduction. A comparison between wet chemical prepared Pd and physical vapor deposited Pd particles has also been made and it was found that, if the influence of residues from the precursor solution is excluded, the main difference in the morphology of Pd particles observed after wet chemical deposition as compared to UHV deposition arises from the difference in substrate morphology.

# Chapter 6

## Activation of Pd/Fe<sub>3</sub>O<sub>4</sub> catalyst

Parts of the results presented in this chapter have been published in:

H.-F. Wang, W. E. Kaden, R. Dowler, M. Sterrer, H.-J. Freund

**Model oxide-supported metal catalysts – Comparison of ultrahigh vacuum and solution based preparation of Pd nanoparticles on a single-crystalline oxide substrate.**

*Phys.Chem.Chem.Phys.*, **2012**, 14, 11525.

## 6.1 Introduction

Catalyst activation is the transformation of the pre-catalyst, i.e. the adsorbed precursor, into a different, catalytically active compound. Together with preparation parameters such as pH and type of precursor salt, the applied activation procedure can affect the final properties of the catalyst (activity, selectivity and stability), mainly because the chemical state of the catalyst, its dispersion and the interaction with the support are determined during activation. Depending on the catalytic reaction and the materials used as catalyst, three major activation procedures can be distinguished:

- calcination, which consists of heating the pre-catalyst in air or oxygen to transform the precursor into oxidic compounds. This kind of activation is usually performed with supported oxide catalysts (e.g. VO<sub>x</sub>, MoO<sub>3</sub>).
- reduction, which transforms the precatalyst into a metallic component and is usually applied to precious metal catalysts such as Pt and Pd. Often, a calcination step is carried out before reduction.
- sulfidization, e.g. in the hydrodesulfurization reaction. Here, an initially oxidic catalyst is transformed into a sulfide during a “running in” period, where the catalyst is in contact with the sulfur containing feed.

Supported Pd catalysts are usually activated by direct reduction of the precursor, or by a combination of calcination and reduction. In most cases, hydrogen is used as a reducing agent.

In this chapter, results for typical activation procedures applied to the model catalysts as prepared and described in the previous chapters, will be presented. All treatments were carried out in the UHV chamber using gas pressures in the range 10<sup>-5</sup> mbar. Molecular oxygen was used for oxidation, whereas CO or H<sub>2</sub> were alternatively used in reduction treatments. The chemisorption properties of the resulting catalyst were analyzed with IRAS and TPD using CO as a probe molecule, and were complemented by XPS analysis. Before presenting the results, a short overview of the interaction of Pd with O<sub>2</sub>, CO and H<sub>2</sub>, as well as into strong metal support interaction (SMSI), which is often encountered when Pd is activated by H<sub>2</sub> reduction at elevated temperature, will be given.

CO is often used as a probe molecule in TPD and IRAS studies of metal single crystals and supported metal nanoparticles and from the spectroscopic results information about the

morphology of supported Pd nanoparticles may be deduced. CO adsorption on Pd has been studied on different systems ranging from Pd single crystal, to physical vapor deposited Pd nanoparticles on the flat oxide support, to chemically prepared Pd nanoparticles on high surface area oxide supports. On Pd(111), CO adsorbs initially at threefold hollow sites. With increasing coverage, compression of the CO adlayer leads to population of bridge sites, and at maximum CO coverage ( $\theta = 0.75$ ), both on-top and threefold hollow sites are populated [201]. On small supported Pd particles, a large fraction of CO adsorbs in on-top position (related to defect structures, steps and edges), while for larger particles single-crystal like behavior with occupation of bridge and/or threefold hollow sites is found. CO does not dissociate on the Pd single crystal surfaces [21], whereas particle size-dependent CO dissociation has been reported for supported Pd particles, with remaining elemental carbon being responsible for site blocking [202, 203].

The interaction of O<sub>2</sub> with Pd surfaces as well as the formation of subsurface and bulk oxygen species has been extensively studied. Studies on Pd single crystal surfaces have shown that molecularly adsorbed oxygen dissociates already at temperatures above 200 K [204]. At elevated temperatures and pressures, slow formation of subsurface and bulk oxygen species occurs [205-210], and finally a PdO phase is stabilized [209, 210]. The reactivity of the different oxygen species in oxidation reactions has been the subject of numerous studies. However, the assignment of the catalytically active phase is still debated [171, 211, 212]. The interaction of oxygen with supported Pd particles is more complicated because support effects and defects also play an important role [206, 213]. The interaction of oxygen with Pd nanoparticles supported on Al<sub>2</sub>O<sub>3</sub>/NiAl(110) and Fe<sub>3</sub>O<sub>4</sub>(111)/Pt(111) has been studied in our department. Oxygen diffusion into NiAl(110) and thickening of the alumina film have been observed [206]. For the Pd/Fe<sub>3</sub>O<sub>4</sub> system, the formation of an interface oxide layer and its effect on CO oxidation have been investigated [178, 179, 181].

H<sub>2</sub> readily dissociates on Pd upon adsorption and then diffuses into the subsurface layers or the bulk [214]. The interaction of H<sub>2</sub> with Pd depends on parameters such as temperature, gas pressure and crystallite size. For bulk-like Pd samples (single crystals), absorbed hydrogen is lost for reactions. On the other hand, hydrogen stored in the subsurface or bulk of Pd nanoparticles remains available for reactions and contributes to the higher activity of Pd nanoparticles compared to Pd bulk single crystals in hydrogenation reactions [215, 216]. In addition, it has been found that carbon deposits influence the hydrogen distribution in Pd nanoparticles by promoting diffusion of H<sub>2</sub> into the subsurface regions [182, 217, 218]. H<sub>2</sub> dissociation and subsequent spill-over onto the support surface can strongly affect the

chemical properties of catalysts during activation. This is particularly true when reducible transition metal oxides are used as supports, which can easily be reduced by hydrogen atoms [219-221].

SMSI was first reported and named in 1978 by Tauster [222], when a strong loss of H<sub>2</sub> sorption capacity was found after high temperature reduction of catalysts consisting of group VIII noble metals supported by reducible oxides (TiO<sub>2</sub>, CeO<sub>2</sub>). Since the loss of sorption capacity was not due to metal agglomeration, an explanation based on a strong interaction between metal and support has been put forward. In the initial work, chemical modification of the supported metal particles, e.g. by bonding with reduced support cations or by formation of intermetallic compounds was suggested to be the primary reason for the modification of the sorption properties [175, 219, 222-224]. Later on it has been shown that, especially for noble metal particles supported on titania, the SMSI is manifested by partial or complete encapsulation of the metal particle by a reduced oxide phase.[175, 225-227] Although SMSI suppresses the chemisorption capacity of the catalyst and is, therefore, in most cases detrimental for catalytic activity, several studies have shown that for some reactions (e.g. CO-H<sub>2</sub> reaction) improved activity and selectivity is obtained with catalysts in the SMSI state [223, 228].

Previous reports have shown that both, encapsulation (e.g. Pd/TiO<sub>2</sub> [175, 229], Pd/CeO<sub>2</sub> [230, 231], Pd/Fe<sub>2</sub>O<sub>3</sub> [232], Pd/silica [233]) and alloy formation (e.g. Pd/ZnO [234], Pd/Ga<sub>2</sub>O<sub>3</sub> [235]) are a possible result of SMSI for supported Pd catalysts.

## 6.2 Catalyst activation: oxidation and CO reduction

As a first step of activation, oxidation and CO reduction of a wet chemically prepared pH 10 Pd/Fe<sub>3</sub>O<sub>4</sub> sample has been studied. Such treatments have previously been reported to be necessary in order to stabilize UHV-prepared supported Pd nanoparticles.[181] Therefore, it can be expected that after this treatment the wet chemically prepared samples studied here will exhibit chemisorption properties similar to those of UHV-prepared samples. It has also to be noted that because of carbon contamination, which could not be avoided during wet chemical preparation and which could not be removed by heating in UHV, no chemisorption of CO was detected on the samples that were reduced by simple thermal treatment. Oxidation and reduction was, therefore, also necessary to clean off carbon.

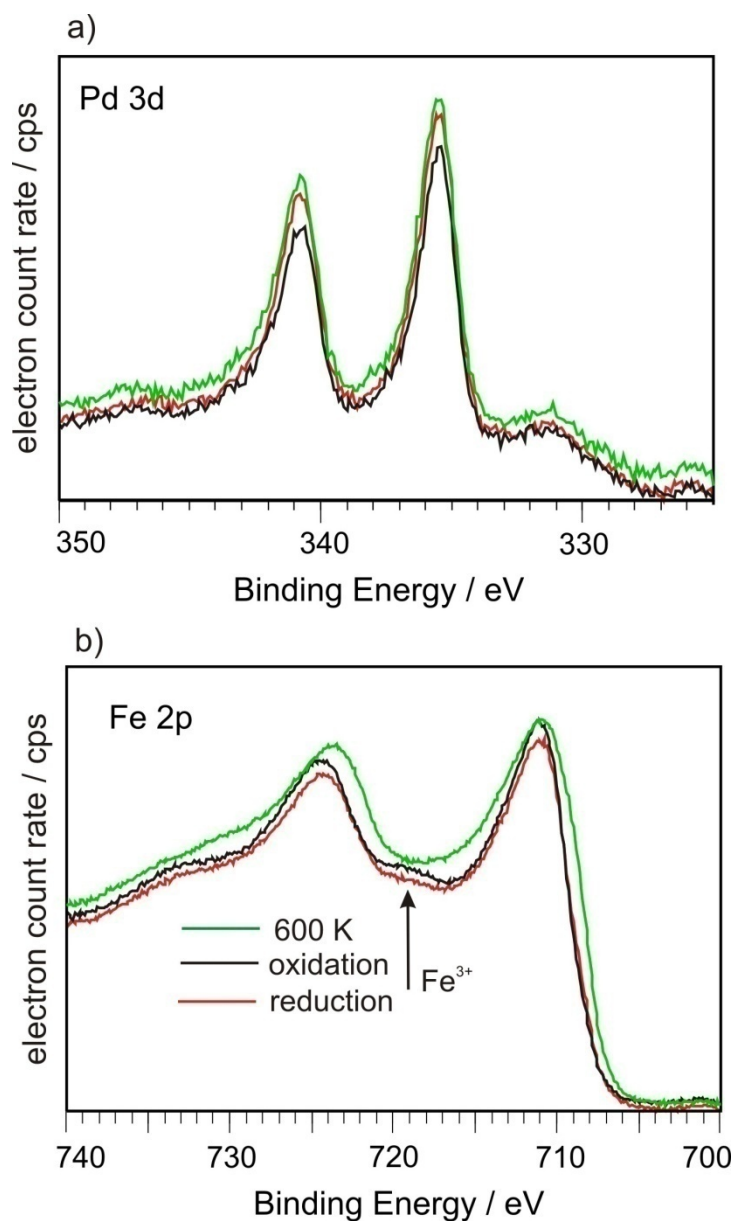


Fig. 6.1. Pd 3d and Fe 2p XPS of Pd/Fe<sub>3</sub>O<sub>4</sub> sample (pH10) after preparation (annealing at 600 K), oxidation and CO reduction.

Figure 6.1 shows Pd 3d and Fe 2p XPS spectra of the Pd/Fe<sub>3</sub>O<sub>4</sub> sample recorded after preparation (annealing at 600 K in UHV), oxidation (600 K, 10<sup>-6</sup> mbar O<sub>2</sub> for 2 h, followed by evacuation at 600 K) and CO reduction (500 K, 10<sup>-6</sup> mbar CO for 1 h). Apart from slight variation in peak intensity, no significant BE shifts are observed in the Pd 3d spectra. This is due to the fact that (i) Pd particles are already fully reduced after thermal reduction in UHV, and (ii) the sample has been evacuated at high temperature after the oxidation treatment, which leads to complete decomposition of the oxidic Pd formed during oxidation. The oxidation has, however, fulfilled its purpose of removal of carbon contaminations.

In contrast to the Pd 3d region, noticeable changes are observed in the Fe 2p region: In comparison to the vacuum-reduced sample, the appearance of the Fe<sup>3+</sup> satellite at 719 eV after oxidation treatment shows that the Fe<sub>3</sub>O<sub>4</sub> support surface becomes readily oxidized. Furthermore, subsequent CO reduction does obviously not significantly affect the oxidation state of the substrate (compare black and red trace in Figure 6.1b).

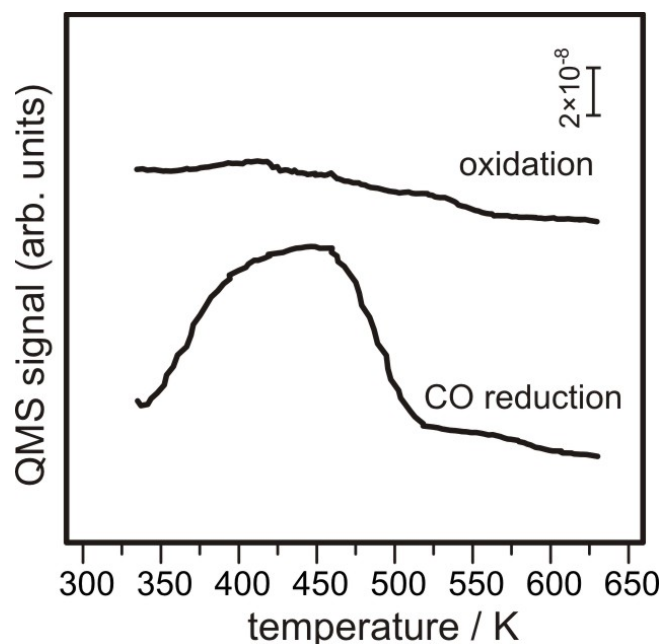


Fig. 6.2. TPD spectra of CO from Pd/Fe<sub>3</sub>O<sub>4</sub> (pH 10) sample were taken after oxidation and CO reduction, respectively. Prior to TPD 10 L CO was dosed at RT. Heating rate was 3 K/s.

The oxidation and CO reduction steps were further studied with CO-TPD and CO-IRAS. In the TPD spectra shown in Figure 6.2, only tiny CO-desorption was observed after oxidation. In contrast, a broad desorption signal extending from 300 K to 500 K, with a maximum at 450 K appears after CO reduction. Similarly, in the corresponding IRAS spectra (Figure 6.3), no CO related bands appeared after the oxidation step, whereas two bands, at 2105 cm<sup>-1</sup> and 1990 cm<sup>-1</sup>, are observed after CO reduction.

The TPD and IRAS results obtained from Pd particles, prepared by wet chemical methods and further subjected to an oxidation and CO reduction treatment, are in line with the expectations for supported Pd nanoparticles. The broad CO desorption feature above room temperature is typical for supported Pd nanoparticles [177]. The presence of metallic Pd nanoparticles is further evidenced by the stretching frequencies noted in IRAS after adsorbing CO over the samples. The band at 2105 cm<sup>-1</sup> can be assigned to CO adsorbed linearly (atop) on Pd sites at Pd(111) facets or defects (steps, edges), and the band at 1990 cm<sup>-1</sup> corresponds

to CO adsorbed on Pd bridge sites at particle edges or Pd(100) facets, respectively.[203, 236] The high atop/bridge intensity ratio observed in Figure 6.3 is typical for small Pd particles and in good agreement with previous CO-IRAS data of UHV prepared Fe<sub>3</sub>O<sub>4</sub>(111)-supported Pd nanoparticles.[198]

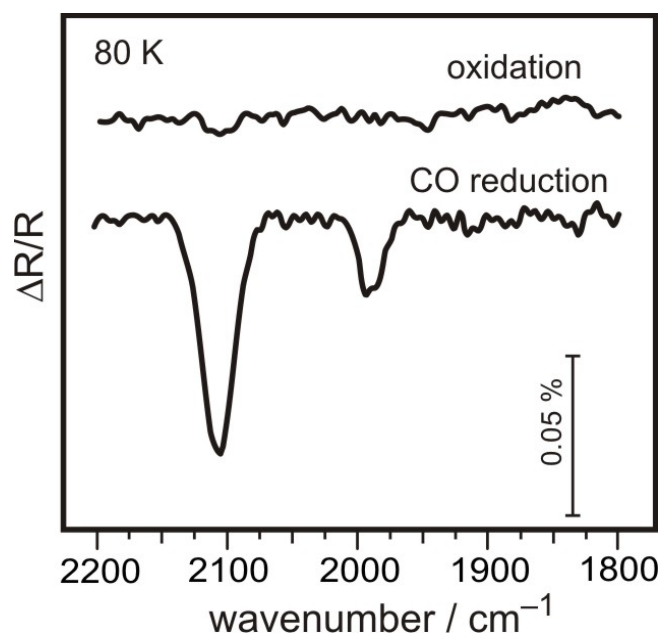


Fig. 6.3. IRAS spectra taken at 80 K for CO saturation coverage on Pd/Fe<sub>3</sub>O<sub>4</sub> (pH 10) sample after oxidation and reduction, respectively.

It has to be noted that while all spectroscopic results obtained after CO reduction are consistent, this is not the case for the oxidized samples. Although similar oxidation protocols were applied for the samples used for XPS, TPD and IRAS analysis, the low BE value in XPS, which is characteristic of metallic Pd rather than of oxidized Pd, does not support the TPD and IRAS results, which, because of the absence of CO chemisorption, point to oxidized Pd particles. On the one hand, this discrepancy may be caused by the fact that the experiments were performed in different UHV chambers. On the other hand, slight variations in Pd loading and particle size could also have an effect on the extent of oxidation.

## 6.3 Effect of reduction atmosphere

### 6.3.1 Results

As an alternative to CO, the reduction treatment was carried out in hydrogen ( $1 \times 10^{-6}$  mbar, 500 K), because it is the most frequently used reducing agent in typical powder catalyst preparations. The TPD results obtained after H<sub>2</sub> reduction of a pH 10 Pd/Fe<sub>3</sub>O<sub>4</sub> sample are

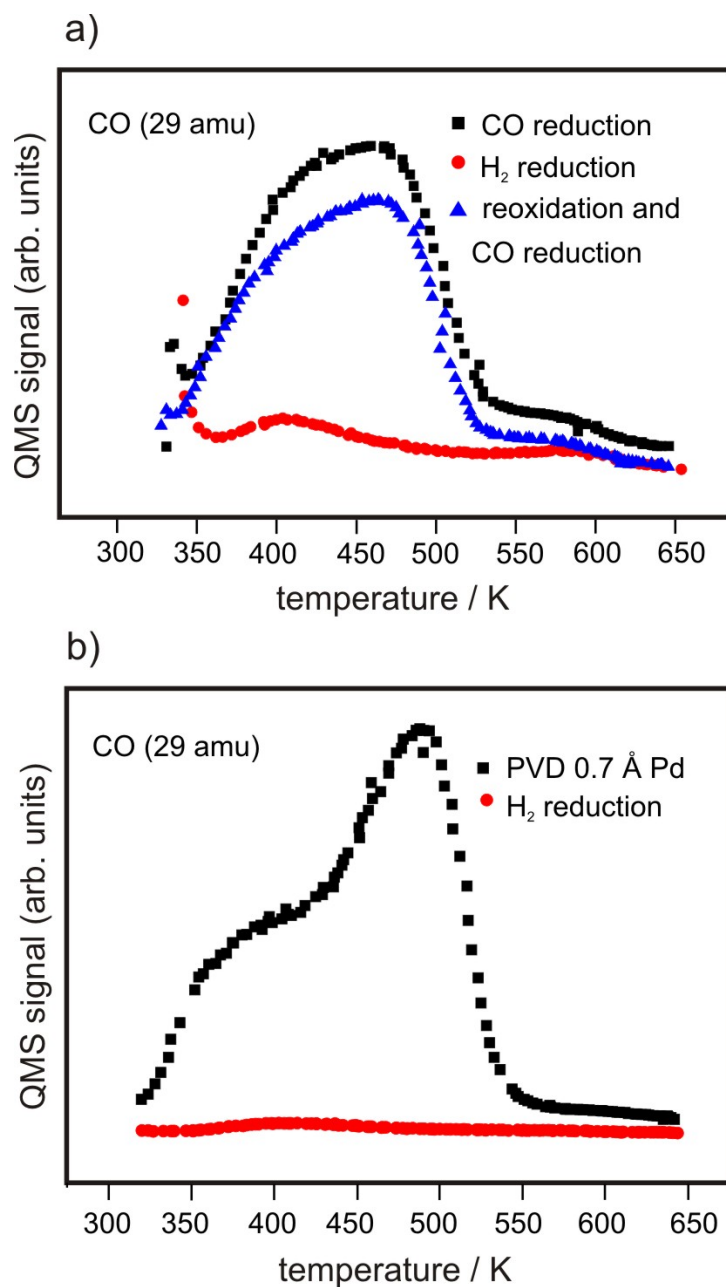


Fig. 6.4. (a) TPD spectra of Pd/Fe<sub>3</sub>O<sub>4</sub> sample (pH 10) after taken after CO reduction, H<sub>2</sub> reduction, reoxidation and CO reduction, respectively; (b) TPD spectra of Pd/Fe<sub>3</sub>O<sub>4</sub> sample prepared by PVD and after H<sub>2</sub> reduction treatment.

shown in Figure 6.4a together with the corresponding results for CO reduction, as well as results for a H<sub>2</sub>-reduced sample following reoxidation and subsequent CO reduction. For the H<sub>2</sub>-reduced sample, strong suppression of CO adsorption above room temperature is clearly evident in the TPD (Figure 6.4a, red trace). A similar suppression in CO adsorption after H<sub>2</sub> reduction was also observed for the PVD-Pd sample as shown in Figure 6.4b. STM images of the Pd/Fe<sub>3</sub>O<sub>4</sub> sample taken before and after H<sub>2</sub> reduction indicate that the morphology of the

particles does not change during the H<sub>2</sub> treatment (Figure 6.5). Reoxidation of this sample followed by CO reduction leads to almost complete restoration of the CO adsorption properties (Figure 6.4a, blue trace).

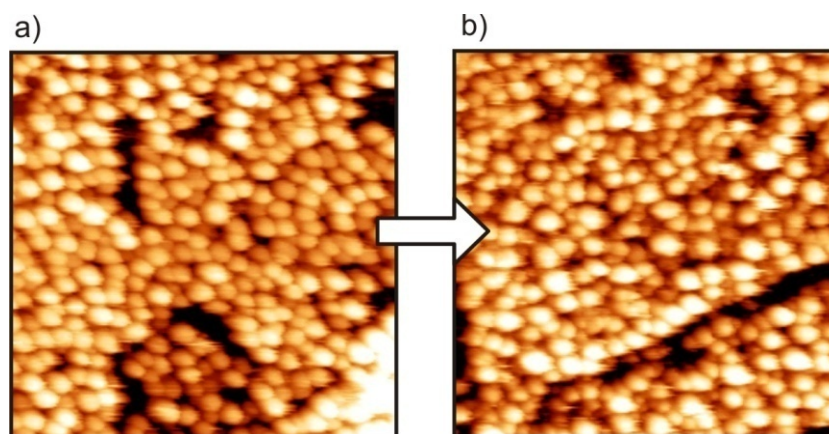


Fig. 6.5. STM images (108 nm × 108 nm) of Pd/Fe<sub>3</sub>O<sub>4</sub> sample (pH10). (a) After annealing at 600 K, (b) after H<sub>2</sub> reduction at 573 K for 30 min.

XPS was applied to gain information about changes in the electronic structure caused by H<sub>2</sub> reduction. Figure 6.6 shows a compilation of Pd 3d and Fe 2p core level spectra from wet deposited Pd (Figure 6.6a) and PVD-Pd (Figure 6.6b), and the Fe 2p spectra from a blank Fe<sub>3</sub>O<sub>4</sub> sample (Figure 6.6c), taken after CO reduction and H<sub>2</sub> reduction, respectively. The changes observed for the wet and PVD Pd/Fe<sub>3</sub>O<sub>4</sub> samples are qualitatively very similar, apart from the larger BE shifts observed for the wet sample. The Pd 3d BE of the CO-reduced sample is found at 335.4 eV, consistent with the presence of metallic Pd nanoparticles. A positive BE shift is observed for both samples after H<sub>2</sub> reduction, the extent being +0.5 eV for the wet sample. By contrast, a shift in the opposite direction, towards lower BE from 710.8 eV to 710.3 eV (Fe 2p<sub>3/2</sub>) in the wet sample, is observed in the Fe 2p region upon H<sub>2</sub> reduction. In addition, a significant broadening of the Fe 2p line with a small shoulder at the low BE side at around 706 eV BE, as well as the disappearance of the Fe<sup>3+</sup> satellite and the appearance of the Fe<sup>2+</sup> satellite are noted. The blank experiment (Fe<sub>3</sub>O<sub>4</sub> exposed to pH10 solution without Pd) shows a similar shift of the Fe 2p line to lower BE after H<sub>2</sub> reduction, but to a slightly lesser extent as compared to the Pd/Fe<sub>3</sub>O<sub>4</sub> sample.

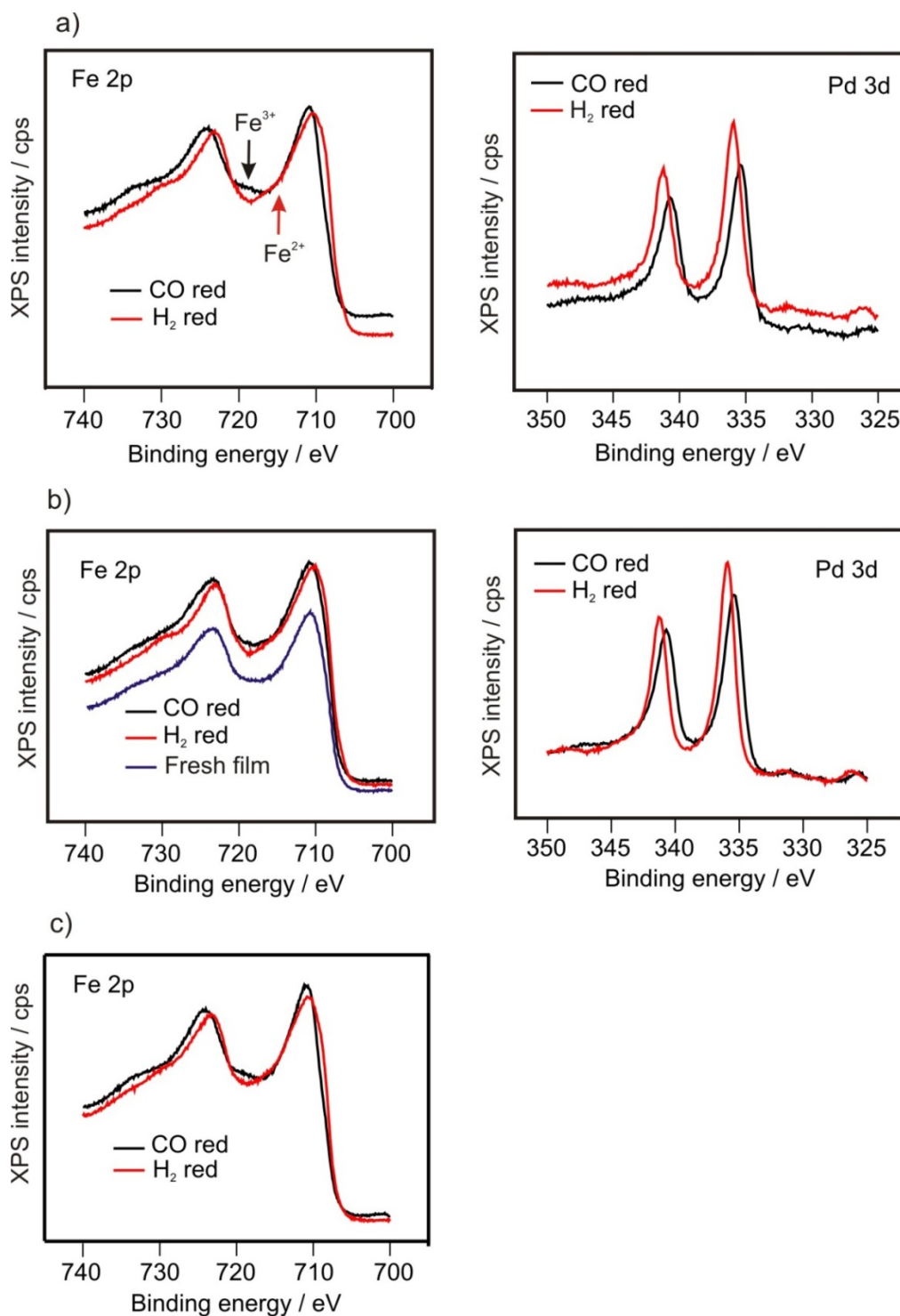


Fig. 6.6. Pd 3d and Fe 2p photoemission spectra of “wet” Pd/Fe<sub>3</sub>O<sub>4</sub>(111) (a), PVD Pd/Fe<sub>3</sub>O<sub>4</sub>(111) (b) and Fe<sub>3</sub>O<sub>4</sub>(111) after contact with pH 10 NaOH solution (c) samples after a series of treatments.

The effect of H<sub>2</sub> reduction was further studied using CO-IRAS. Figure 6.7 shows a comparison of the CO vibrational spectra obtained after dosing 10 L CO on the CO- and H<sub>2</sub>-reduced samples, respectively. The two bands typical of on-top (2105 cm<sup>-1</sup>) and bridge bonded CO (1990 cm<sup>-1</sup>) on small, metallic Pd nanoparticles observed after CO reduction are

replaced by three bands at 2145 cm<sup>-1</sup>, 2087 cm<sup>-1</sup>, and 2020 cm<sup>-1</sup> after H<sub>2</sub> reduction. The changes in the CO chemisorption properties, observed with both TPD and IRAS, point to strong modification of the Pd nanoparticles upon H<sub>2</sub> reduction. The origin of this modification will be discussed in the following.

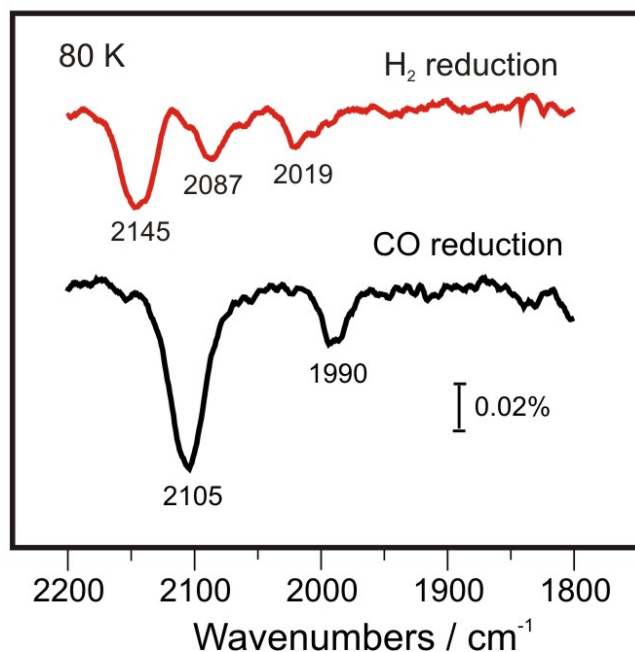


Fig. 6.7. IRAS of Pd/Fe<sub>3</sub>O<sub>4</sub> sample (pH 10) taken at 80 K after CO reduction, H<sub>2</sub> reduction, respectively.

### 6.3.2 Discussion

The suppression of CO adsorption capacity observed with TPD provides strong support for the occurrence of strong metal support interaction (SMSI) induced by H<sub>2</sub> reduction in the Pd/Fe<sub>3</sub>O<sub>4</sub> system. As discussed above, one typical manifestation of SMSI is encapsulation of particles by an oxide layer. Encapsulation would reasonably explain the suppression of CO chemisorption, because the bonding of CO to the oxide surfaces is usually rather weak. Based on the IRAS and XPS data in Figures 6.6 and 6.7, encapsulation can, however, be excluded as possible origin of the SMSI state for the Pd/Fe<sub>3</sub>O<sub>4</sub> sample. Although CO adsorption above room temperature is suppressed after H<sub>2</sub> reduction, IRAS data recorded at low temperature show characteristic CO adsorption features, albeit, different from those present over regular Pd particles. Based on agreement with previously reported CO-IR data for co-deposited Pd and Fe particles on alumina,[237] the observed changes in the IR spectrum after H<sub>2</sub> reduction

can be explained by the formation of PdFe alloy particles, with the observed IRAS bands assigned as follows: The signal at 2087 cm<sup>-1</sup> is indicative of atop CO-Pd binding over the PdFe bimetallic particles. The red-shift with respect to the monometallic Pd particles results from modification of the electronic structure at the binding site due to the presence of neighboring Fe atoms, and a reduced dipolar coupling. Fe atoms on the modified particles give rise to the CO signal at 2020 cm<sup>-1</sup>, in agreement with studies on bimetallic PdFe particles.[237] The bridge-bonded CO observed on regular Pd particles at 1990 cm<sup>-1</sup> cannot be populated on the bimetallic particles because the presence of Fe atoms on the particle surface results in a corresponding unavailability of multi-coordinated Pd sites. Instead, a new CO band appears at 2145 cm<sup>-1</sup>, which is frequently observed for CO adsorbed on Pd particles which have been modified by chemisorbed oxygen.[181, 238] However, under the conditions of the present experiment (H<sub>2</sub> reduction), the presence of a chemisorbed oxygen layer on the Pd particles can reasonably be excluded. Therefore, this signal is assigned to CO adsorbed on iron sites that are formed on the oxide support during H<sub>2</sub> reduction.

Pd-Fe alloy particle formation is further supported by the XPS results (Figure 6.6). A shift of the Pd 3d photoemission peak to higher binding energy relative to monometallic Pd is indicative of Pd-Fe alloying, and has been observed previously for extended bimetallic systems as well as oxide supported bimetallic particles.[237, 239] Such shifts arise in part from charge transfer of electrons from Pd to Fe and Pd(4d) → Pd(5s,5p) orbital rehybridization. For such Pd-Fe alloys to form, a certain degree of Fe mobility within the film is required, which may be achieved by the removal of O atoms in sufficiently reducing conditions. The Fe 2p peak shifting to lower BE and the observation of a pronounced Fe<sup>2+</sup> satellite in XPS both point to the strong reduction of the substrate from predominantly Fe<sup>3+</sup> to Fe<sup>2+</sup>. In addition, a small shoulder appears on the H<sub>2</sub> reduced sample at the low binding energy side at around 706 eV, which is indicative of metallic iron sites in the bimetallic particles.

Typically, the reduction of iron oxides in hydrogen follows the sequence (FeOOH → Fe<sub>2</sub>O<sub>3</sub> → Fe<sub>3</sub>O<sub>4</sub> → Fe), and the reduction temperature, which is usually in the range 550-900 K, depends on various parameters, such as preparation, and H<sub>2</sub>O partial pressure.[240] The presence of metals capable of dissociating H<sub>2</sub> (e.g. Pd) leads to lowering of the reduction temperature via spill-over of hydrogen atoms onto the support.[220, 221] The rather mild conditions that were shown to induce the formation of Pd-Fe particles here are in agreement with such a spill-over mechanism. Further support for the enhanced substrate reduction in the

presence of Pd comes from comparison with the blank Fe<sub>3</sub>O<sub>4</sub> sample (Figure 6.6b), which shows that in this case the support is affected by H<sub>2</sub> treatment to a much lesser extent.

Although the reduction behavior and SMSI states of many catalyst materials have been investigated, rather little is known about this subject on iron oxide supported Pd particles. Previous studies reported alloy formation after reduction of Pd-Fe bimetallic catalysts supported on zeolites or Al<sub>2</sub>O<sub>3</sub>, [241, 242] and more recently, encapsulation of Pd has been reported after H<sub>2</sub> reduction at 523 K for iron oxide supported Pd prepared by coprecipitation. [232] In that case, the encapsulated Pd particles showed high activity towards low-temperature CO oxidation, which is conceptually similar to recent reports of high activity for thin FeO(111) layers on Pt(111) substrates. [152] It is interesting to note that at similar reduction temperature, the coprecipitated sample shows a different SMSI state relative to the model system prepared in here (encapsulation vs. alloy formation). A possible explanation for this difference involves the different support phases, and while oxygen released during the transformation of Fe<sub>2</sub>O<sub>3</sub> into Fe<sub>3</sub>O<sub>4</sub> may facilitate Pd encapsulation over the coprecipitated samples, a similar phase transformation is not possible in the model system described here, where partial reduction of the Fe<sub>3</sub>O<sub>4</sub> surface activates alloy formation.

Finally, comparison should be made to a similar system investigated previously in our department. Qin et al. reported that Pt nanoparticles supported on Fe<sub>3</sub>O<sub>4</sub>(111) can be driven into a SMSI state by simple UHV annealing to 850 K [243]. Different to a Pd/Fe<sub>3</sub>O<sub>4</sub> sample, they observed sintering of Pt particles and wetting of the Fe<sub>3</sub>O<sub>4</sub> surface with formation of extended two-dimensional islands. Interestingly, the surface of the extended Pt islands showed some contrast modulation in STM, which could be identified as a FeO overlayer, providing evidence for Pt particle encapsulation. Pd did not show such a behavior after high temperature annealing and remained present as three-dimensional particles. The reason for the different behavior observed for Pd and Pt on Fe<sub>3</sub>O<sub>4</sub> is most likely the difference in adhesion energy, being higher for Pt and favoring wetting of the Fe<sub>3</sub>O<sub>4</sub> surface. The wetting seems to represent an important prerequisite for encapsulation to occur. Qin et al. also investigated the effect of H<sub>2</sub> reduction (at 600 K) on the properties of Pt on Fe<sub>3</sub>O<sub>4</sub>. Based on the same suppression of CO adsorption as for the Pt/Fe<sub>3</sub>O<sub>4</sub> sample heated to 850 K as observed with TPD, they suggested that H<sub>2</sub> reduction leads also to particle encapsulation. Based on the results presented here, this interpretation needs, however, to be questioned, since Pt-Fe alloy formation seems to be another likely explanation for the observed suppression of CO adsorption capacity.

## 6.4 CO oxidation

From the point of view of fundamental research, CO oxidation is recognized as a prototypical reaction for heterogeneous surface processes and as a chemical probe for the surface properties. [232] CO oxidation is one of the simplest catalytic reactions occurring on metal surfaces and is represented by the chemical equation (1)



which consists of the following three individual reaction steps:



Over noble metals, CO oxidation follows a Langmuir-Hinshelwood mechanism in which both reactants are adsorbed on the metal surface (see eq. 2-4). However, when the metal catalyst is supported on a reducible oxide, an additional reaction pathway involving oxygen species delivered by the support (Mars-Van Krevelen mechanism) may open up.

Here, CO oxidation was used as a test reaction in order to investigate the influence of the different chemical states attained by the Pd/Fe<sub>3</sub>O<sub>4</sub> model systems after CO and H<sub>2</sub>-reduction on the catalytic activity. CO oxidation has previously been studied by Meyer et al. using a Pd/Fe<sub>3</sub>O<sub>4</sub>(111) model system [177]. According to their findings, the results presented here are split into a) the non-catalytic reaction, and b) the catalytic reaction. The catalytic tests were performed as temperature programmed reaction experiments with <sup>13</sup>C<sup>16</sup>O and <sup>16</sup>O<sub>2</sub> dosed at 300 K onto the sample surface, followed by heating at a constant heating rate of 3 K/s and mass spectrometric detection of the reaction product <sup>13</sup>C<sup>16</sup>O<sub>2</sub>.

## 6.4.1 Non-catalytic test

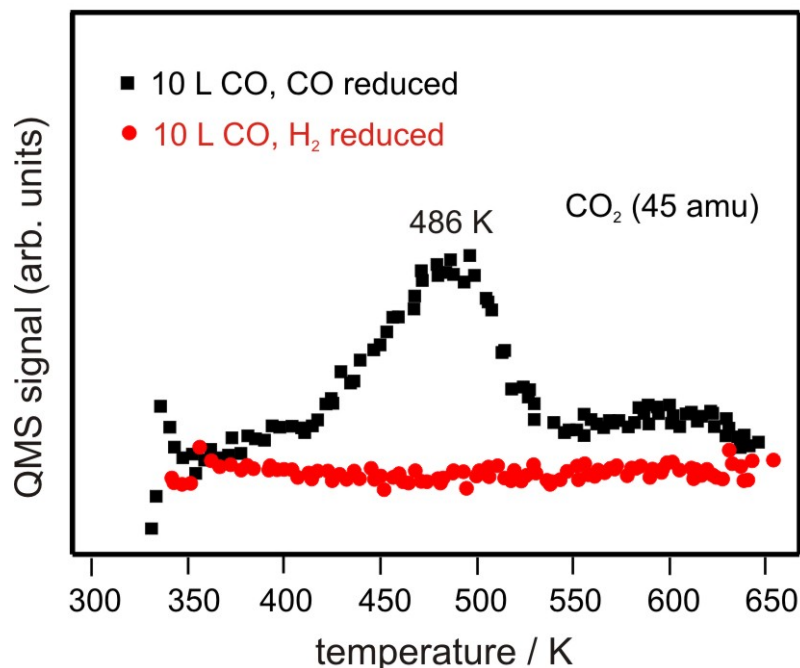


Fig. 6.8 CO<sub>2</sub>-TPD spectra of Pd/Fe<sub>3</sub>O<sub>4</sub> sample (pH 10) reduced with CO or H<sub>2</sub> by dosing 10 L CO initially.

For the non-catalytic test, the Pd/Fe<sub>3</sub>O<sub>4</sub> samples were dosed only with CO, and the formation of CO<sub>2</sub> was monitored with the QMS. Figure 6.8 shows the <sup>13</sup>C<sup>16</sup>O<sub>2</sub> traces obtained from the CO- and H<sub>2</sub>-reduced samples, respectively. The CO-reduced sample exhibits clear activity for non-catalytic CO<sub>2</sub> production, with CO<sub>2</sub> formation observed at ~ 486 K (Figure 6.8, black trace). This result is in agreement with previous experiments on UHV-prepared Pd/Fe<sub>3</sub>O<sub>4</sub> model systems.[177] According to Meyer et al., this non-catalytic activity stems from reaction of CO adsorbed on the Pd particles, with lattice oxygen species from the Fe<sub>3</sub>O<sub>4</sub> support (eq. 5).



At first sight, this result seems a bit surprising, bearing in mind that, in contrast to the UHV-prepared model catalyst, the sample prepared here has already been extensively exposed to CO during the reduction treatment. However, the XPS result reported in Figure 6.1b has shown that no substrate reduction occurs during high temperature CO treatment. The short residence time of CO on both, the Pd particles and the Fe<sub>3</sub>O<sub>4</sub> support at the selected reduction

temperature and reduction pressure is the most likely explanation for this observation. Therefore, the support surface remains oxidized and lattice oxygen remains available for reaction even after CO reduction treatment.

In contrast, strong reduction of the support occurs during H<sub>2</sub> reduction, as discussed in Sec. 6.3 (Figure 6.6). As a consequence, the non-catalytic CO oxidation test performed with the H<sub>2</sub>-reduced sample shows no activity at all (Figure 6.8). Although the abundance of CO adsorbed on Pd is quite small (Figure 6.4a), which could explain this result, it is rather the unavailability of lattice oxygen, which has been effectively depleted from the surface regions during reduction, that accounts for the inactivity of this sample in non-catalytic CO oxidation.

#### 6.4.2 Catalytic test

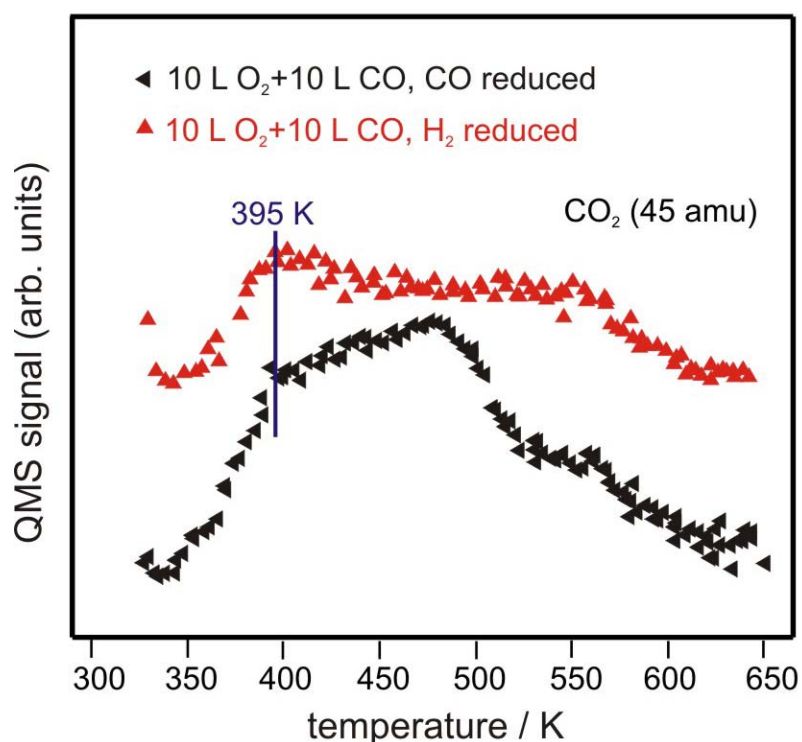


Fig. 6.9 CO<sub>2</sub>-TPD spectra of Pd/Fe<sub>3</sub>O<sub>4</sub> sample (pH 10) reduced with CO or H<sub>2</sub> by dosing 10 L O<sub>2</sub> initially followed by 10 L CO.

In the catalytic CO oxidation test, the samples were first precovered with oxygen, followed by saturation coverage of <sup>13</sup>CO (300 K). The results for <sup>13</sup>C<sup>16</sup>O<sub>2</sub> production during the TPR runs are shown in Figure 6.9. Two CO<sub>2</sub> desorption maxima, at 395 K and 490 K, are observed for the CO-reduced sample (Figure 6.9, black trace). The peak at 490 K can be assigned,

according to the results presented in the previous section, to the non-catalytically produced CO<sub>2</sub>. The second peak at lower temperature results from catalytic CO<sub>2</sub> formation resulting from oxygen and CO chemisorbed on the Pd nanoparticles, in line with previous observation for this reaction on Pd single crystal surfaces and supported Pd nanoparticles [206, 238, 244].

The H<sub>2</sub>-reduced sample shows also reactivity in the catalytic test, with a broad CO<sub>2</sub> desorption extending from 350 K to 600 K exhibiting a clear maximum at 395 K. Close inspection of the TPR spectra in Figure 6.9 and comparison with Figure 6.8 reveals that apart from the non-catalytic contribution that is missing in the H<sub>2</sub>-reduced sample, catalytic activity in CO oxidation is similar in H<sub>2</sub>- and CO reduced samples. It has been proposed that reduced Fe-oxide phases may actively be involved in the supply of reactive oxygen species for CO oxidation reaction [154], which could explain the catalytic activity of the H<sub>2</sub>-reduced sample. However, it can be expected the Pd-Fe alloy particles formed during H<sub>2</sub> reduction are similarly, if not even more reactive towards oxygen dissociation than the monometallic Pd nanoparticles. According to the similar CO<sub>2</sub> desorption temperature for the catalytic reaction observed for both the H<sub>2</sub>- and CO-reduced samples, it is concluded that the activity of the Pd-Fe alloy particles results from a catalytic reaction occurring mainly on the particles surfaces.

The results presented in Figure 6.9 show that the catalytic activity toward CO oxidation is not influenced by the SMSI state under the conditions of this experiment. It has also to be noted that, given the fact that similar catalytic CO<sub>2</sub> yield is obtained for both samples, which have, however, very different CO chemisorption properties (Figure 6.4a), the fraction of adsorbed CO that reacts under these conditions, is obviously quite small.

## 6.5 Summary

In this chapter, results for activation of a Pd/Fe<sub>3</sub>O<sub>4</sub> model catalyst prepared by wet chemical methods in different reducing atmosphere, together with spectroscopic characterization of the resulting surface properties, were presented. The catalyst activated by CO reduction shows CO adsorption capacity and infrared spectroscopic features of adsorbed CO that are characteristic for monometallic Pd nanoparticles. When the catalyst is reduced in H<sub>2</sub>, the CO adsorption is heavily suppressed although the morphology of the catalyst surfaces does not change. The results indicate strong metal support interaction. The combined IRAS and XPS results presented here show that Pd-Fe alloy particles are formed as a result of SMSI.

Non-catalytic CO oxidation on CO-reduced Pd follows a Mars-Van Krevelen mechanism with CO adsorbed on Pd reacting with lattice oxygen from the oxide support. The test of catalytic activity of the Pd catalysts shows that the SMSI state does not significantly alter the catalytic activity for CO oxidation under the experimental conditions used in this study.

# **Chapter 7**

## **Summary and outlook**

Catalyst preparation is one of the most important steps in a catalysts lifetime, because factors that influence the applicability or usability of a catalyst, such as morphology, chemical properties, and stability, are to a great extent determined by the applied preparation and activation procedures. Because of the chemical complexity of the fundamental processes involved in catalyst preparation and the morphological complexity of real-world catalyst samples, elucidation of the basic mechanisms of catalyst preparation remains a great challenge. In this work, a surface science approach to catalyst preparation has been developed, which relies on the utilization of thin, single crystalline oxide films as substrates. The use of thin oxide films allows typical surface science methods to be applied and both morphological and chemical insights during the early stages of supported metal catalyst preparation to be gained. Thin iron oxide films grown on Pt(111) were chosen as model supports and the preparation of supported Pd nanoparticle model catalysts resulting from adsorption of Pd precursor complexes out of PdCl<sub>2</sub> solution has been studied. Scanning Tunneling Microscopy (STM) and X-ray Photoelectron Spectroscopy (XPS) allowed studying the morphological and chemical changes during the transformation of adsorbed Pd precursor complexes into nanoparticles in the early stages of catalyst preparation. Chemisorption properties of the activated Pd catalysts have been investigated by Temperature Programmed Desorption (TPD) and Infrared Reflection Absorption Spectroscopy (IRAS).

Single crystalline FeO(111) and Fe<sub>3</sub>O<sub>4</sub>(111) films supported on Pt(111) in different environments haven been firstly studied by STM. The FeO film becomes highly reactive with hydroxyls formation on the surface when exposed to air and water, while retaining an ordered surface structure. An in situ STM study of the FeO film in aqueous solution showed that the surface structure remained ordered in acid solution and less ordered in neutral or basic solutions. The strong stability of Fe<sub>3</sub>O<sub>4</sub> film in acid or alkaline solution makes it an ideal material as support for metal catalyst preparation.

We have in particular investigated the thermal transformation of Pd precursor complexes into metal nanoparticles on Fe<sub>3</sub>O<sub>4</sub>(111). STM results revealed that during heating Pd particles homogeneously nucleate from the adsorbed molecular precursor after impregnation of Fe<sub>3</sub>O<sub>4</sub>(111) with acidic PdCl<sub>2</sub> solution, and that the particle-substrate interaction is temperature dependent. In addition, the morphological information is important for the interpretation of the spectroscopic data and helps in the assignment of the XPS signals. Residual chlorine is found to be mainly in contact with the Pd particles and could be easily removed by oxidation/reduction, which, however, leads to particle sintering.

The effect of solution pH on Pd loading, particle size and distribution, and the Pd speciation during preparation has been studied. Homogeneously distributed Pd particles with narrow size distribution are formed on  $\text{Fe}_3\text{O}_4(111)$  after deposition from  $\text{PdCl}_2$  solutions with low (pH 1-3) and high pH (e.g. pH 10). Large particles and high loading were obtained when a  $\text{PdCl}_2$  solution in the near-neutral pH range (pH 4.5-6) was used.

$\text{Pd}/\text{Fe}_3\text{O}_4$  model catalysts prepared by wet-chemical methods can be activated by oxidation and CO reduction. The chemisorptive properties as investigated with CO as a probe molecule show that the wet-chemical preparation and the following CO activation lead to Pd particles with properties similar to a  $\text{Pd}/\text{Fe}_3\text{O}_4$  model catalyst prepared exclusively in UHV. Slight differences in the morphology of the Pd particles obtained with wet-chemical methods as compared to the UHV approach result from a different functionalization of the support surface because of exposure to solution. When the catalyst is reduced with  $\text{H}_2$  instead of CO, the CO adsorption capacity is heavily suppressed, indicating strong metal support interaction (SMSI). Often, encapsulation of the metal particles by an oxide overlayer is the result of SMSI; however, the combined XPS and IRAS results for the model catalyst investigated here provides evidence that a Pd-Fe alloy is formed during reduction with  $\text{H}_2$ .

Non-catalytic CO oxidation on CO-reduced  $\text{Pd}/\text{Fe}_3\text{O}_4$  follows a Mars-Van Krevelen mechanism with CO adsorbed on Pd reacting with lattice oxygen of the oxide support. On  $\text{H}_2$ -reduced  $\text{Pd}/\text{Fe}_3\text{O}_4$ , no  $\text{CO}_2$  was detected because of the unavailability of lattice oxygen due to the strong reduction of the  $\text{Fe}_3\text{O}_4$  support by  $\text{H}_2$ . The catalytic CO oxidation test suggests that the SMSI state does not greatly affect the catalytic activity under the condition used in this study.

The approach presented herein offers great potential for further elucidation of catalyst preparation procedures. In particular, variation of parameters such as concentration and type of precursor salt and, hence, the different nucleation behavior and chemical identity of surface species, may contribute to a better understanding of the influence of preparation parameters on the final properties of a catalyst. In addition, more work should be invested in in-situ microscopic and spectroscopic studies of the oxide-solution interface during the impregnation step, which could reveal in detail the adsorption behavior of precursor complexes. In the future, the work present in this thesis should also be extended to study the effect of preparation conditions on the reactivity and selectivity of the catalyst in catalytic reactions.

---

## Abbreviations

AES	Auger Electron Spectroscopy
AFM	Atomic Force Microscopy
DOS	Density of States
CVD	Chemical Vapor Deposition
EXAFS	Extended X-ray Absorption Fine Structure
IRAS	Infrared Reflection Absorption Spectroscopy
LDOS	Local Density of States
LEED	Low Energy Electron Diffraction
LEIS	Low Energy Ion Scattering
ML	Monolayer
NMR	Nuclear Magnetic Resonance
PVD	Physical Vapor Deposition
QMS	Quadrupole Mass Spectrometer
SFG	Sum Frequency Generation
SIMS	Secondary Ion Mass Spectrometry
SMSI	Strong Metal-Support Interaction
STM	Scanning Tunneling Microscopy
TPD	Temperature Programmed Desorption
UHV	Ultra-high Vacuum
XPS	X-ray Photoemission Spectroscopy

## Curriculum Vitae

For reasons of data protection,  
the curriculum vitae is not included in the online version

## Publications and conference presentations

### Publications

- **Hui-Feng Wang**, William Kaden, Rhys Dowler, Martin Sterrer, Hans-Joachim Freund, Model oxide-supported metal catalysts - Comparison of ultrahigh vacuum and solution based preparation of Pd nanoparticles on a single-crystalline oxide substrate, *Phys.Chem.Chem.Phys.*, **2012**, 14, 11525.
- **Hui-Feng Wang**, Hiroko Ariga, Rhys Dowler, Martin Sterrer, Hans-Joachim Freund, Surface science approach to catalyst preparation – Pd deposition onto thin Fe<sub>3</sub>O<sub>4</sub>(111) films from PdCl<sub>2</sub> precursor, *J. Catal. (Priority Communication)* **2012**, 286, 1.
- Franziska Ringleb, Yuichi Fujimori, **Hui-Feng Wang**, Hiroko Ariga, Esther Carrasco, Martin Sterrer, Hans-Joachim Freund, et al., Interaction of Water with FeO(111)/Pt(111) – Environmental Effects and Influence of Oxygen, *J. Phys. Chem. C*, **2011**, 115, 19328.

### Conference Presentations

- Model studies of supported metal catalyst preparation – Deposition of Pd on Fe<sub>3</sub>O<sub>4</sub>(111) from PdCl<sub>2</sub> precursor, **15th International Congress on Catalysis 2012**, München, **July 2012** (Poster)
- “Model studies of catalyst preparation: Deposition of Pd on Fe<sub>3</sub>O<sub>4</sub>(111) from aqueous solution and formation of Pd-Fe bimetallic particles during activation”, **2nd International Symposium on Intermetallic Compounds in Methanol Steam Reforming**, München, **June 2012** (Poster)
- “The effect of solution variables and pretreatment on supported Pd catalyst preparation”, **XV. International Symposium on Relations between Homogeneous and Heterogeneous Catalysis**, Berlin, **September 2011** (Excellent Poster).
- “Model studies of supported catalyst preparation: Pd deposition on iron oxide films from the liquid phase”, **Rideal Conference**, Cardiff, UK, **April 2011** (Best Poster)
- “Deposition of Pd on a single crystalline Fe<sub>3</sub>O<sub>4</sub>(111) surfaces from liquid phase precursors”, **Bunsentagung 2010**, Bielefeld, Germany, **May 2010** (Talk)
- “Model studies of supported catalyst preparation: Pd deposition on FeO(111) films from the liquid phase”, **43. Jahrestreffen Deutscher Katalytiker**, Weimar, Germany, **March 2010** (Poster)

## Bibliography

1. Ertl, G., *Reactions at Surfaces: From Atoms to Complexity (Nobel Lecture)*. Angewandte Chemie International Edition, 2008. **47**(19): p. 3524-3535.
2. Gunter, P.L.J., et al., *Surface science approach to modeling supported catalysts*. Catalysis Reviews-Science and Engineering, 1997. **39**(1-2): p. 77-168.
3. Ertl, G., *Reactions at Well-Defined Surfaces*. Surface Science, 1994. **299**(1-3): p. 742-754.
4. Marsh, A.L., Ribeiro, F. H., Somorjai, G. A., *Single Crystal Surfaces*, in *Handbook of Heterogeneous Catalysis*, G. Ertl, Knözinger, H., Schüth, F., and Weitkamp, J., Editor. 2008, Wiley-VCH Verlagsgesellschaft mbH: Weinheim. p. 1259-1276.
5. Rodriguez, J.A., Goodman, D. W., *High-Pressure Catalytic Reactions over Single-Crystal Metal-Surfaces*. Surface Science Reports, 1991. **14**(1-2): p. 1-107.
6. McIntyre, B.J., Salmeron, M., Somorjai, G. A., *In-Situ Scanning-Tunneling-Microscopy Study of Platinum (110) in a Reactor Cell at High-Pressures and Temperatures*. Journal of Vacuum Science & Technology a-Vacuum Surfaces and Films, 1993. **11**(4): p. 1964-1968.
7. Cremer, P.S., et al., *Ethylene hydrogenation on Pt(111) monitored in situ at high pressures using sum frequency generation*. Journal of the American Chemical Society, 1996. **118**(12): p. 2942-2949.
8. Dellwig, T., et al., *Bridging the pressure and materials gaps: High pressure sum frequency generation study on supported Pd nanoparticles*. Physical Review Letters, 2000. **85**(4): p. 776-779.
9. Osterlund, L., et al., *Bridging the pressure gap in surface science at the atomic level: H/Cu(110)*. Physical Review Letters, 2001. **86**(3): p. 460-463.
10. Hendriksen, B.L.M., Frenken, J. W. M., *CO oxidation on Pt(110): Scanning tunneling microscopy inside a high-pressure flow reactor*. Physical Review Letters, 2002. **89**(4).
11. Freund, H.J., et al., *Preparation and characterization of model catalysts: from ultrahigh vacuum to in situ conditions at the atomic dimension*. Journal of Catalysis, 2003. **216**(1-2): p. 223-235.
12. Salmeron, M., Schlogl, R., *Ambient pressure photoelectron spectroscopy: A new tool for surface science and nanotechnology*. Surface Science Reports, 2008. **63**(4): p. 169-199.
13. Yang, F., Goodman, D. W. , *In Situ STM Studies of Model Catalysts*, in *Scanning Tunneling Microscopy in Surface Science, Nanoscience and Catalysis*, M. Bowker and P.R. Davies, Editors. 2010, WILEY-VCH Verlag GmbH & Co. KGaA: Weinheim. p. 55-95.
14. Tao, F., Salmeron, M., *In Situ Studies of Chemistry and Structure of Materials in Reactive Environments*. Science, 2011. **331**(6014): p. 171-174.
15. Goodman, D.W., *Catalysis - from Single-Crystals to the Real-World*. Surface Science, 1994. **299**(1-3): p. 837-848.
16. Freund, H.J., *Adsorption of Gases on Solid-Surfaces*. Berichte Der Bunsen-Gesellschaft-Physical Chemistry Chemical Physics, 1995. **99**(11): p. 1261-1281.
17. Goodman, D.W., *Model Studies in Catalysis Using Surface Science Probes*. Chemical Reviews, 1995. **95**(3): p. 523-536.
18. Freund, H.J., Kuhlbeck, H., Staemmler, V., *Oxide surfaces*. Reports on Progress in Physics, 1996. **59**(3): p. 283-347.

19. Freund, H.J., *Adsorption of gases on complex: Solid surfaces*. Angewandte Chemie-International Edition, 1997. **36**(5): p. 452-475.
20. Campbell, C.T., *Ultrathin metal films and particles on oxide surfaces: Structural, electronic and chemisorptive properties*. Surface Science Reports, 1997. **27**(1-3): p. 1-111.
21. Henry, C.R., *Surface studies of supported model catalysts*. Surface Science Reports, 1998. **31**(7-8): p. 235-325.
22. Baumer, M., Freund, H. J., *Metal deposits on well-ordered oxide films*. Progress in Surface Science, 1999. **61**(7-8): p. 127-198.
23. Freund, H.J., Baumer, M., Kuhlenbeck, H., *Catalysis and surface science: What do we learn from studies of oxide-supported cluster model systems?* Advances in Catalysis, Vol 45, 2000. **45**: p. 333-384.
24. Goodman, D.W., *Model catalysts: from imagining to imaging a working surface*. Journal of Catalysis, 2003. **216**(1-2): p. 213-222.
25. Libuda, J., Freund, H. J., *Molecular beam experiments on model catalysts*. Surface Science Reports, 2005. **57**(7-8): p. 157-298.
26. Freund, H.J., Goodman, D. W. , *Ultrathin Oxide Films*, in *Handbook of Heterogeneous Catalysis*, G. Ertl, Knözinger, H., Schüth, F., and Weitkamp, J., Editor. 2007, Wiley-VCH Verlagsgesellschaft mbH: Weinheim. p. 1309-1338.
27. Freund, H.-J., Pacchioni, G., *Oxide ultra-thin films on metals: new materials for the design of supported metal catalysts*. Chemical Society Reviews, 2008. **37**(10): p. 2224-2242.
28. Lai, X., et al., *Scanning tunneling microscopy studies of metal clusters supported on TiO<sub>2</sub> (110): Morphology and electronic structure*. Progress in Surface Science, 1998. **59**(1-4): p. 25-52.
29. Thune, P.C., Niemantsverdriet, J. W., *Surface science models of industrial catalysts*. Surface Science, 2009. **603**(10-12): p. 1756-1762.
30. Freund, H.J., Goodman, D. W. , *Ultrathin Oxide Films*, in *Handbook of Heterogeneous Catalysis*, G. Ertl, Knözinger, H., Schüth, F., and Weitkamp, J., Editor. 2008, Wiley-VCH Verlagsgesellschaft mbH: Weinheim. p. 1309-1338.
31. Eshelman, L.M., Dejong, A. M., Niemantsverdriet, J. W., *Preparation of ZrO<sub>2</sub> on Flat, Conducting SiO<sub>2</sub>/Si(100) Model Supports by Wet Chemical Techniques - X-Ray Photoelectron-Spectroscopy and Auger Depth Profiling*. Catalysis Letters, 1991. **10**(3-4): p. 201-209.
32. Borg, H.J., Vandenoetelaar, L. C. A., Niemantsverdriet, J. W., *Preparation of a Rhodium Catalyst from Rhodium Trichloride on a Flat, Conducting Alumina Support Studied with Static Secondary Ion Mass-Spectrometry and Monochromatic X-Ray Photoelectron-Spectroscopy*. Catalysis Letters, 1993. **17**(1-2): p. 81-95.
33. Doornkamp, C., et al., *Exploration of the Deposition of Submicrometer Particles by Spin-Coating*. Journal of Materials Research, 1995. **10**(2): p. 411-424.
34. Bird, D.P.C., de Castilho, C. M. C., Lambert, R. M., *Catalyst genesis studied by atomic force microscopy*. Surface Science, 2000. **449**(1-3): p. L221-L227.
35. Akita, T., et al., *SEM and RHEED-REM study of au particles deposited on rutile TiO<sub>2</sub> (110) by deposition precipitation and gas-phase grafting methods*. Journal of Catalysis, 2002. **212**(1): p. 119-123.
36. Park, C., et al., *Probing outer-sphere adsorption of aqueous metal complexes at the oxide-water interface with resonant anomalous X-ray reflectivity*. Physical Review Letters, 2005. **94**(7): p. 076104-1-4.

37. Bourikas, K., Kordulis, C., Lycourghiotis, A., *The role of the liquid-solid interface in the preparation of supported catalysts*. Catalysis Reviews-Science and Engineering, 2006. **48**(4): p. 363-444.
38. Marceau, E., Carrier, X., Che, M., Clause, O., and Marcilly, C. , *Ion Exchange and Impregnation*, in *Handbook of Heterogeneous Catalysis*, G. Ertl, Knözinger, H., Schüth, F., and Weitkamp, J., Editor. 2008, Wiley-VCH Verlagsgesellschaft mbH: Weinheim. p. 467-484.
39. Lambert, J.F., Che, M., *The molecular approach to supported catalysts synthesis: state of the art and future challenges*. Journal of Molecular Catalysis a-Chemical, 2000. **162**(1-2): p. 5-18.
40. Shelimov, B., et al., *Initial steps of the alumina-supported platinum catalyst preparation: A molecular study by Pt-195 NMR, UV-visible, EXAFS, and Raman spectroscopy*. Journal of Catalysis, 1999. **185**(2): p. 462-478.
41. Schreier, M., Regalbuto, J. R., *A fundamental study of Pt tetraammine impregnation of silica I. The electrostatic nature of platinum adsorption*. Journal of Catalysis, 2004. **225**(1): p. 190-202.
42. Spieker, W.A., et al., *An EXAFS study of the coordination chemistry of hydrogen hexachloroplatinate(IV) 2. Speciation of complexes adsorbed onto alumina*. Applied Catalysis a-General, 2003. **243**(1): p. 53-66.
43. Mondloch, J.E., Bayram, E., Finke, R. G., *A review of the kinetics and mechanisms of formation of supported-nanoparticle heterogeneous catalysts*. Journal of Molecular Catalysis a-Chemical, 2012. **355**: p. 1-38.
44. Sterrer, M., et al., *Crossover from three-dimensional to two-dimensional geometries of Au nanostructures on thin MgO(001) films: A confirmation of theoretical predictions*. Physical Review Letters, 2007. **98**(20): p. 206103.
45. Vurens, G.H., Salmeron, M., Somorjai, G. A., *The Preparation of Thin Ordered Transition-Metal Oxide-Films on Metal Single-Crystals for Surface Science Studies*. Progress in Surface Science, 1989. **32**(3-4): p. 333-360.
46. Libuda, J., et al., *Structure and Defects of an Ordered Alumina Film on NiAl(110)*. Surface Science, 1994. **318**(1-2): p. 61-73.
47. Baumer, M. and H.J. Freund, *Metal deposits on well-ordered oxide films*. Progress in Surface Science, 1999. **61**(7-8): p. 127-198.
48. Weissenrieder, J., et al., *Atomic structure of a thin silica film on a Mo(112) substrate: A two-dimensional network of SiO<sub>4</sub> tetrahedra*. Physical Review Letters, 2005. **95**(7): p. 076103.
49. Loeffler, D., et al., *Growth and Structure of Crystalline Silica Sheet on Ru(0001)*. Physical Review Letters, 2010. **105**(14).
50. Xu, X.P., Goodman, D. W., *The Preparation and Characterization of Ultra-Thin Silicon Dioxide Films on a Mo(110) Surface*. Surface Science, 1993. **282**(3): p. 323-332.
51. Chen, M.S., Santra, A. K., Goodman, D. W., *Structure of thin SiO<sub>2</sub> films grown on Mo(112)*. Physical Review B, 2004. **69**(15).
52. Wu, M.C., et al., *Synthesis and Characterization of Ultra-Thin MgO Films on Mo(100)*. Chemical Physics Letters, 1991. **182**(5): p. 472-478.
53. Schintke, S., et al., *Insulator at the ultrathin limit: MgO on Ag(001)*. Physical Review Letters, 2001. **87**(27).
54. Sterrer, M., et al., *Identification of color centers on MgO(001) thin films with scanning tunneling microscopy*. Journal of Physical Chemistry B, 2006. **110**(1): p. 46-49.
55. Weiss, W., Ranke, W., *Surface chemistry and catalysis on well-defined epitaxial iron-oxide layers*. Progress in Surface Science, 2002. **70**(1-3): p. 1-151.

56. Lu, J.L., et al., *Morphology and defect structure of the CeO<sub>2</sub>(111) films grown on Ru(0001) as studied by scanning tunneling microscopy*. Surface Science, 2006. **600**(22): p. 5004-5010.
57. Hardacre, C., Roe, G. M., Lambert, R. M., *Structure, Composition and Thermal-Properties of Cerium Oxide-Films on Platinum(111)*. Surface Science, 1995. **326**(1-2): p. 1-10.
58. Mullins, D.R., Radulovic, P. V., Overbury, S. H., *Ordered cerium oxide thin films grown on Ru(0001) and Ni(111)*. Surface Science, 1999. **429**(1-3): p. 186-198.
59. Dupuis, A.C., et al., *V<sub>2</sub>O<sub>3</sub>(0001) on Au(111) and W(110): growth, termination and electronic structure*. Surface Science, 2003. **539**(1-3): p. 99-112.
60. Leisenberger, F.P., et al., *Nature, growth, and stability of vanadium oxides on Pd(111)*. Journal of Vacuum Science & Technology a-Vacuum Surfaces and Films, 1999. **17**(4): p. 1743-1749.
61. Lewis, K.B., Oyama, S. T., Somorjai, G. A., *The Preparation and Reactivity of Thin, Ordered Films of Vanadium-Oxide on Au(111)*. Surface Science, 1990. **233**(1-2): p. 75-83.
62. Shao, X., et al., *Growth and Morphology of Calcium-Oxide Films Grown on Mo(001)*. Journal of Physical Chemistry C, 2011. **115**(17): p. 8784-8789.
63. Kumar, D., Chen, M. S., Goodman, D. W., *Characterization of ultra-thin TiO<sub>2</sub> films grown on Mo(112)*. Thin Solid Films, 2006. **515**(4): p. 1475-1479.
64. Boffa, A.B., et al., *The Growth and Structure of Titanium-Oxide Films on Pt(111) Investigated by LEED, XPS, ISS, and STM*. Surface Science, 1995. **326**(1-2): p. 80-92.
65. Diebold, U., *The surface science of titanium dioxide*. Surface Science Reports, 2003. **48**(5-8): p. 53-229.
66. Fu, Q., Wagner, T., *Interaction of nanostructured metal overlayers with oxide surfaces*. Surface Science Reports, 2007. **62**(11): p. 431-498.
67. Nickl, J., Schlogl, R., Baiker, A., Knozinger, H., Ertl, G., *Preparation and Characterization of a Model System for the Study of Monolayers and Multilayers of Vanadia Supported on Titania*. Catalysis Letters, 1989. **3**(5-6): p. 379-387.
68. Yeung, K.L., Wolf, E. E., *A Scanning Tunneling Microscopy Study of the Platinum Catalysts Particles Supported on Graphite*. Journal of Vacuum Science & Technology B, 1991. **9**(2): p. 798-803.
69. Yeung, K.L., Wolf, E. E., *Scanning Tunneling Microscopy Studies of Size and Morphology of Pt Graphite Catalysts*. Journal of Catalysis, 1992. **135**(1): p. 13-26.
70. Atamny, F., Duff, D., Baiker, A., *Stm and Tem Investigation of a Technical Platinum Graphite Catalyst*. Catalysis Letters, 1995. **34**(3-4): p. 305-311.
71. Atamny, F., Baiker, A., *Investigation of carbon-based catalysts by scanning tunneling microscopy: Opportunities and limitations*. Applied Catalysis a-General, 1998. **173**(2): p. 201-230.
72. Chusuei, C.C., et al., *A nanoscale model catalyst preparation: Solution deposition of phosphine-stabilized gold clusters onto a planar TiO<sub>2</sub>(110) support*. Langmuir, 2001. **17**(13): p. 4113-4117.
73. Wilms, M., Kruft, M., Bermes, G., Wandelt, K., *A new and sophisticated electrochemical scanning tunneling microscope design for the investigation of potentiodynamic processes*. Review of Scientific Instruments, 1999. **70**(9): p. 3641-3650.
74. Bardeen, J., *Tunnelling from a Many-Particle Point of View*. Physical Review Letters, 1961. **6**(2): p. 57.
75. Tersoff, J., Hamann, D. R., *Theory of the Scanning Tunneling Microscope*. Physical Review B, 1985. **31**(2): p. 805-813.

76. Chen, C.J., *Introduction to Scanning Tunneling Microscopy*. 2008, Oxford: Oxford University Press.
77. Wilms, M., et al., *New and versatile ultrahigh vacuum scanning tunneling microscope for film growth experiments*. Review of Scientific Instruments, 1998. **69**(7): p. 2696-2703.
78. Sonnenfeld, R., Hansma, P. K., *Atomic-Resolution Microscopy in Water*. Science, 1986. **232**(4747): p. 211-213.
79. Kolb, D.M., *Electrochemical surface science*. Angewandte Chemie-International Edition, 2001. **40**(7): p. 1162-1181.
80. Itaya, K., *In situ scanning tunneling microscopy in electrolyte solutions*. Progress in Surface Science, 1998. **58**(3): p. 121-247.
81. Wilms, M., et al., *In-situ STM investigation of adsorbate structures on Cu(111) in sulfuric acid electrolyte*. Surface Science, 1998. **416**(1-2): p. 121-140.
82. Eggleston, C.M., Stumm, W., *Scanning-Tunneling-Microscopy of Cr(III) Chemisorbed on Alpha-Fe<sub>2</sub>O<sub>3</sub> (001) Surfaces from Aqueous-Solution - Direct Observation of Surface Mobility and Clustering*. Geochimica Et Cosmochimica Acta, 1993. **57**(19): p. 4843-4850.
83. Besenbacher, F., Lauritsen, J. V. and Vang, R. T., *Scanning Probe Methods*, in *Handbook of Heterogeneous Catalysis, 2 edn*, H.K. G. Ertl, F. Schüth, J. Weitkamp, Editor. 2008, Wiley-VCH: Weinheim.
84. Bowker, M., Davies, P.R. (Editors), *Scanning Tunneling Microscopy in Surface Science, Nanoscience and Catalysis*. 2010, Weinheim: WILEY-VCH.
85. Berglund, C.N., Spicer, W. E., *Photoemission Studies of Copper + Silver - Theory*. Physical Review a-General Physics, 1964. **136**(4A): p. 1030.
86. Hüfner, S., *Photoelectron Spectroscopy - Principles and Applications*. 2003, Berlin: Springer.
87. Hedin, L., Michiels, J., Inglesfield, J., *Transition from the adiabatic to the sudden limit in core-electron photoemission*. Physical Review B, 1998. **58**(23): p. 15565-15582.
88. Koopmans, T., *Über die Zuordnung von Wellenfunktionen und Eigenwerten zu den Einzelnen Elektronen eines Atoms*. Physica, 1934. **1**: p. 104-113.
89. Niemantsverdriet, J.W., *Spectroscopy in Catalysis An Introduction*. 2007, Weinheim: WILEY-VCH.
90. Ratner, B.D., Castner, D. G. , *Electron Spectroscopy for Chemical Analysis*, in *Surface Analysis – The Principal Techniques, 2nd Edition*, J.C.a.G. Vickerman, I. S., Editor. 2009, John Wiley & Sons, Ltd: The Atrium.
91. Citrin, P.H., Wertheim, G. K., Baer, Y., *Many-Body Processes in X-Ray Photoemission Line-Shapes from Li, Na, Mg, and Al Metals*. Physical Review B, 1977. **16**(10): p. 4256-4282.
92. Somorjai, G.A., *Chemistry in Two Dimensions, Surfaces*. 1981, Ithaca: Cornell University Press.
93. Redhead, P.A., *Thermal desorption of gases*. Vacuum, 1962. **12**: p. 203.
94. Toebes, M.L., van Dillen, J. A., de Jong, Y. P., *Synthesis of supported palladium catalysts*. Journal of Molecular Catalysis a-Chemical, 2001. **173**(1-2): p. 75-98.
95. Regalbuto, J.R., in *Synthesis of Solid Catalysts*, K.P.d. Jong, Editor. 2009, Wiley-VCH: Weinheim. p. 45.
96. Didillon, B., et al., *From colloidal particles to supported catalysts: a comprehensive study of palladium oxide hydrosols deposited on alumina*, in *Preparation of Catalysts Vii*. 1998, Elsevier Science Publ B V: Amsterdam. p. 41-54.

97. Tait, C.D., Janecky, D. R., Rogers, P. S. Z., *Speciation of Aqueous Palladium(II) Chloride Solutions Using Optical Spectroscopies*. *Geochimica Et Cosmochimica Acta*, 1991. **55**(5): p. 1253-1264.
98. Troitskii, S.Y., Fedotov, M. A., Likholobov, V. A., *Studies of the Compositions of Pd(II) Hydrolysis Products*. *Russian Chemical Bulletin*, 1993. **42**(4): p. 634-639.
99. Elding, L.I., Olsson, L. F., *Electronic Absorption-Spectra of Square-Planar Chloro-Aqua and Bromo-Aqua Complexes of Palladium(II) and Platinum(II)*. *Journal of Physical Chemistry*, 1978. **82**(1): p. 69-74.
100. Klasovsky, F., Claus, P., Wolf, D., *Influence of Preparation Parameters on the Performance of Colloid-derived Oxidic Palladium Catalysts for Selective Hydrogenation of C-C Triple Bonds*. *Topics in Catalysis*, 2009. **52**(4): p. 412-423.
101. Espinosa-Alonso, L., de Jong, K. P., Weckhuysen, B. M., *A UV-Vis micro-spectroscopic study to rationalize the influence of Cl(-) (aq) on the formation of different Pd macro-distributions on gamma-Al(2)O(3) catalyst bodies*. *Physical Chemistry Chemical Physics*, 2010. **12**(1): p. 97-107.
102. Harada, T., et al., *A simple method for preparing highly active palladium catalysts loaded on various carbon supports for liquid-phase oxidation and hydrogenation reactions*. *Journal of Molecular Catalysis a-Chemical*, 2007. **268**(1-2): p. 59-64.
103. Boily, J.-F., Seward, T. M., Charnock, J. M., *The hydrolysis and precipitation of Pd(II) in 0.6 mol kg<sup>-1</sup> NaCl: A potentiometric, spectrophotometric, and EXAFS study*. *Geochimica Et Cosmochimica Acta*, 2007. **71**(20): p. 4834-4845.
104. Moreau, F., Bond, G. C., Taylor, A. O., *Gold on titania catalysts for the oxidation of carbon monoxide: control of pH during preparation with various gold contents*. *Journal of Catalysis*, 2005. **231**(1): p. 105-114.
105. Heise, M.S., Schwarz, J. A., *Preparation of Metal Distributions within Catalyst Supports .1. Effect of PH on Catalytic Metal Profiles*. *Journal of Colloid and Interface Science*, 1985. **107**(1): p. 237-243.
106. Lee, S.J., Gavriilidis, A., *Supported Au catalysts for low-temperature CO oxidation prepared by impregnation*. *Journal of Catalysis*, 2002. **206**(2): p. 305-313.
107. Lekhal, A., Glasser, B. J., Khinast, J. G., *Influence of pH and ionic strength on the metal profile of impregnation catalysts*. *Chemical Engineering Science*, 2004. **59**(5): p. 1063-1077.
108. K.P. de Jong (Ed.), *Synthesis of Solid Catalysts*. 2009, Weinheim: Wiley-VCH.
109. Ivanova, S., et al., *Preparation of alumina supported gold catalysts: Influence of washing procedures, mechanism of particles size growth*. *Applied Catalysis a-General*, 2006. **298**: p. 57-64.
110. Hugon, A., El Kolli, N., Louis, C., *Advances in the preparation of supported gold catalysts: Mechanism of deposition, simplification of the procedures and relevance of the elimination of chlorine*. *Journal of Catalysis*. **274**(2): p. 239-250.
111. Delannoy, L., et al., *Preparation of supported gold nanoparticles by a modified incipient wetness impregnation method*. *Journal of Physical Chemistry B*, 2006. **110**(45): p. 22471-22478.
112. Roth, D., et al., *Catalytic behaviour of Cl-free and Cl-containing Pd/Al<sub>2</sub>O<sub>3</sub> catalysts in the total oxidation of methane at low temperature*. *Applied Catalysis a-General*, 2000. **203**(1): p. 37-45.
113. Oh, H.S., et al., *Selective catalytic oxidation of CO: Effect of chloride on supported Au catalysts*. *Journal of Catalysis*, 2002. **210**(2): p. 375-386.
114. Baatz, C., Decker, N., Prusse, U., *New innovative gold catalysts prepared by an improved incipient wetness method*. *Journal of Catalysis*, 2008. **258**(1): p. 165-169.

115. Haruta, M., *Catalysis of gold nanoparticles deposited on metal oxides*. Cattech, 2002. **6**(3): p. 102-115.
116. Gopinath, R., et al., *Influence of Pd precursor and method of preparation on hydrodechlorination activity of alumina supported palladium catalysts*. Catalysis Letters, 2008. **120**(3-4): p. 312-319.
117. Lear, T., et al., *The application of infrared spectroscopy to probe the surface morphology of alumina-supported palladium catalysts*. Journal of Chemical Physics, 2005. **123**(17).
118. Lear, T., et al., *A model high surface area alumina-supported palladium catalyst*. Physical Chemistry Chemical Physics, 2005. **7**(4): p. 565-567.
119. Kepinski, L., Wolcyrz, M., Okal, J., *Effect of Chlorine on Microstructure and Activity of Pd/CeO<sub>2</sub> Catalysts*. Journal of the Chemical Society-Faraday Transactions, 1995. **91**(3): p. 507-515.
120. Kepinski, L., Okal, J., *Occurrence and mechanism of formation of CeOCl in Pd/CeO<sub>2</sub> catalysts*. Journal of Catalysis, 2000. **192**(1): p. 48-53.
121. Karhu, H., et al., *XPS analysis of chlorine residues in supported Pt and Pd catalysts with low metal loading*. Applied Catalysis a-General, 2003. **247**(2): p. 283-294.
122. Geus, J.W., van Dillen, A. J., *Preparation of Supported Catalysts by Deposition-Precipitation*, in *Handbook of Heterogeneous Catalysis*, G. Ertl, Knözinger, H., Schüth, F., and Weitkamp, J., Editor. 2008, Wiley-VCH Verlagsgesellschaft mbH: Weinheim. p. 428-467.
123. Louis, C., *Deposition-Precipitation Synthesis of Supported Metal Catalysts*, in *CATALYST PREPARATION Science and Engineering*, J.R. Regalbuto, Editor. 2007, CRC Press: New York.
124. Tsubota, S., Cunningham, D.A.H., Bando, Y., Haruta, M., *Preparation of nanometer gold strongly interacted with TiO<sub>2</sub> and the structure sensitivity in low-temperature oxidation of CO*. Studies in Surface Science and Catalysis, 1991. **91**: p. 227-235.
125. Bamwenda, G.R., et al., *The influence of the preparation methods on the catalytic activity of platinum and gold supported on TiO<sub>2</sub> for CO oxidation*. Catalysis Letters, 1997. **44**(1-2): p. 83-87.
126. Zanella, R., Delannoy, L., Louis, C., *Mechanism of deposition of gold precursors onto TiO<sub>2</sub> during the preparation by cation adsorption and deposition-precipitation with NaOH and urea*. Applied Catalysis a-General, 2005. **291**(1-2): p. 62-72.
127. Cornell, R.M., Schwertmann, U., *The iron oxides*. 2003, Weinheim: Wiley-VCH.
128. Vurens, G.H., Salmeron, M., Somorjai, G. A., *Structure, Composition and Chemisorption Studies of Thin Ordered Iron-Oxide Films on Platinum(111)*. Surface Science, 1988. **201**(1-2): p. 129-144.
129. Weiss, W., et al., *Surface-Structure Determination of an Oxide Film Grown on a Foreign Substrate - Fe<sub>3</sub>O<sub>4</sub> Multilayer on Pt(111) Identified by Low-Energy-Electron Diffraction*. Physical Review Letters, 1993. **71**(12): p. 1848-1851.
130. Galloway, H.C., Benitez, J. J., Salmeron, M., *The Structure of Monolayer Films of Feo on Pt(111)*. Surface Science, 1993. **298**(1): p. 127-133.
131. Kim, Y.J., et al., *The growth of iron oxide films on Pt(111): a combined XPD, STM, and LEED study*. Surface Science, 1998. **416**(1-2): p. 68-111.
132. Roddatis, V.V., et al., *Transmission electron microscopy investigation of Fe<sub>3</sub>O<sub>4</sub> films grown on (111) Pt substrates*. Thin Solid Films, 2001. **396**(1-2): p. 78-83.
133. Lemire, C., et al., *The surface structure of Fe<sub>3</sub>O<sub>4</sub>(111) films as studied by CO adsorption*. Surface Science, 2004. **572**(1): p. 103-114.
134. Rienks, E.D.L., et al., *Surface potential of a polar oxide film: FeO on Pt(111)*. Physical Review B, 2005. **71**(24): p. 4.

135. Huang, W.X., Ranke, W., *Autocatalytic partial reduction of FeO(111) and Fe<sub>3</sub>O<sub>4</sub>(111) films by atomic hydrogen*. Surface Science, 2006. **600**(4): p. 793-802.
136. Ketteler, G., et al., *Bulk and surface phases of iron oxides in an oxygen and water atmosphere at low pressure*. Physical Chemistry Chemical Physics, 2001. **3**(6): p. 1114-1122.
137. Ritter, M., Ranke, W., Weiss, W., *Growth and structure of ultrathin FeO films on Pt(111) studied by STM and LEED*. Physical Review B, 1998. **57**(12): p. 7240-7251.
138. Weiss, W., Ritter, M., *Metal oxide heteroepitaxy: Stranski-Krastanov growth for iron oxides on Pt(111)*. Physical Review B, 1999. **59**(7): p. 5201-5213.
139. Fadley, C.S., et al., *Photoelectron diffraction: New dimensions in space, time, and spin*. Journal of Electron Spectroscopy and Related Phenomena, 1995. **75**: p. 273-297.
140. Galloway, H.C., Sautet, P., Salmeron, M., *Structure and contrast in scanning tunneling microscopy of oxides: FeO monolayer on Pt(111)*. Physical Review B, 1996. **54**(16): p. 11145-11148.
141. Shaikhutdinov, S.K., et al., *Defect structures on epitaxial Fe<sub>3</sub>O<sub>4</sub>(111) films*. Physical Review B, 1999. **60**(15): p. 11062-11069.
142. Paul, M., et al., *Thermodynamic stability and atomic and electronic structure of reduced Fe<sub>3</sub>O<sub>4</sub> (111) single-crystal surfaces*. Physical Review B, 2007. **76**(7): p. 075412-1-8.
143. Joseph, Y., et al., *Adsorption of water on FeO(111) and Fe<sub>3</sub>O<sub>4</sub>(111): identification of active sites for dissociation*. Chemical Physics Letters, 1999. **314**(3-4): p. 195-202.
144. Kendelewicz, T., et al., *Reaction of water with the (100) and (111) surfaces of Fe<sub>3</sub>O<sub>4</sub>*. Surface Science, 2000. **453**(1-3): p. 32-46.
145. Joseph, Y., Ranke, W., Weiss, W., *Water on FeO(111) and Fe<sub>3</sub>O<sub>4</sub>(111): Adsorption behavior on different surface terminations*. Journal of Physical Chemistry B, 2000. **104**(14): p. 3224-3236.
146. Leist, U., Ranke, W., Al-Shamery, K., *Water adsorption and growth of ice on epitaxial Fe<sub>3</sub>O<sub>4</sub>(111), FeO(111) and Fe<sub>2</sub>O<sub>3</sub>(biphase)*. Physical Chemistry Chemical Physics, 2003. **5**(11): p. 2435-2441.
147. Daschbach, J.L., et al., *Water adsorption, desorption, and clustering on FeO(111)*. Journal of Physical Chemistry B, 2005. **109**(20): p. 10362-10370.
148. Cutting, R.S., et al., *Substrate-termination and H<sub>2</sub>O-coverage dependent dissociation of H<sub>2</sub>O on Fe<sub>3</sub>O<sub>4</sub>(111)*. Surface Science, 2008. **602**(6): p. 1155-1165.
149. Yamamoto, S., et al., *Water Adsorption on alpha-Fe<sub>2</sub>O<sub>3</sub>(0001) at near Ambient Conditions*. Journal of Physical Chemistry C. **114**(5): p. 2256-2266.
150. Wang, W., et al., *Observation of water dissociation on nanometer-sized FeO islands grown on Pt(111)*. Chemical Physics Letters, 2010. **500**(1-3): p. 76-81.
151. de Smit, E., et al., *On the Surface Chemistry of Iron Oxides in Reactive Gas Atmospheres*. Angewandte Chemie-International Edition, 2011. **50**(7): p. 1584-1588.
152. Sun, Y.N., et al., *Monolayer iron oxide film on platinum promotes low temperature CO oxidation*. Journal of Catalysis, 2009. **266**(2): p. 359-368.
153. Sun, Y.N., et al., *The Interplay between Structure and CO Oxidation Catalysis on Metal-Supported Ultrathin Oxide Films*. Angewandte Chemie-International Edition, 2010. **49**(26): p. 4418-4421.
154. Liu, L.Q., et al., *Low-temperature CO oxidation over supported Pt, Pd catalysts: Particular role of FeO<sub>x</sub> support for oxygen supply during reactions*. Journal of Catalysis, 2010. **274**(1): p. 1-10.
155. Liu, J., et al., *Aqueous-phase reforming of ethylene glycol to hydrogen on Pd/Fe<sub>3</sub>O<sub>4</sub> catalyst prepared by co-precipitation: Metal-support interaction and excellent intrinsic activity*. Journal of Catalysis, 2010. **274**(2): p. 287-295.

156. Shaikhutdinov, S., Weiss, W., *Adsorbate dynamics on iron oxide surfaces studied by scanning tunneling microscopy*. Journal of Molecular Catalysis a-Chemical, 2000. **158**(1): p. 129-133.
157. SchedelNiedrig, T., W. Weiss, and R. Schlogl, *Electronic structure of ultrathin ordered iron oxide films grown onto Pt(111)*. Physical Review B, 1995. **52**(24): p. 17449-17460.
158. Brundle, C.R., Chuang, T. J., Wandelt, K., *Core and Valence Level Photoemission Studies of Iron-Oxide Surfaces and Oxidation of Iron*. Surface Science, 1977. **68**(1): p. 459-468.
159. Muhler, M., R. Schlogl, and G. Ertl, *The Nature of the Iron Oxide-Based Catalyst for Dehydrogenation of Ethylbenzene to Styrene*. Journal of Catalysis, 1992. **138**(2): p. 413-444.
160. Ringleb, F., et al., *Interaction of Water with FeO(111)/Pt(111): Environmental Effects and Influence of Oxygen*. Journal of Physical Chemistry C, 2011. **115**(39): p. 19328-19335.
161. Mancey, D.S., et al., *An Electrochemical Investigation of the Dissolution of Magnetite in Acidic Electrolytes*. Journal of the Electrochemical Society, 1993. **140**(3): p. 637-642.
162. Virtanen, S., et al., *Dissolution of thin iron oxide films used as models for iron passive films studied by in situ x-ray absorption near-edge spectroscopy*. Journal of the Electrochemical Society, 1997. **144**(1): p. 198-204.
163. Shen, W.J., Matsumura, Y., *Low-temperature methanol decomposition to carbon monoxide and hydrogen catalysed over cationic palladium species in Pd/CeO<sub>2</sub>*. Physical Chemistry Chemical Physics, 2000. **2**(7): p. 1519-1522.
164. Babu, N.S., et al., *Influence of particle size and nature of Pd species on the hydrodechlorination of chloroaromatics: Studies on Pd/TiO<sub>2</sub> catalysts in chlorobenzene conversion*. Catalysis Today, 2009. **141**(1-2): p. 120-124.
165. Li, Z., et al., *A titania-supported highly dispersed palladium nano-catalyst generated via in situ reduction for efficient Heck coupling reaction*. Journal of Molecular Catalysis a-Chemical. **328**(1-2): p. 93-98.
166. Pavlova, S.N., et al., *Low-temperature co oxidation on iron oxide supported palladium*. Reaction Kinetics and Catalysis Letters, 1996. **59**(1): p. 103-110.
167. Musolino, M.G., et al., *Aliphatic carbonyl reduction promoted by palladium catalysts under mild conditions*. Applied Catalysis a-General. **379**(1-2): p. 77-86.
168. Zou, W.Q., Gonzalez, R. D., *Thermal-Stability of Silica-Supported Palladium Catalysts Prepared by the Sol-Gel Method*. Applied Catalysis a-General, 1995. **126**(2): p. 351-364.
169. Berlowitz, P.J., Peden, C. H. F., Goodman, D. W., *Kinetics of CO Oxidation on Single-Crystal Pd, Pt, and Ir*. Journal of Physical Chemistry, 1988. **92**(18): p. 5213-5221.
170. Hendriksen, B.L.M., Bobaru, S. C., Frenken, J. W. M., *Looking at heterogeneous catalysis at atmospheric pressure using tunnel vision*. Topics in Catalysis, 2005. **36**(1-4): p. 43-54.
171. Gao, F., et al., *CO Oxidation on Pt-Group Metals from Ultrahigh Vacuum to Near Atmospheric Pressures. 2. Palladium and Platinum*. Journal of Physical Chemistry C, 2009. **113**(1): p. 174-181.
172. Borasio, M., et al., *In situ studies of methanol decomposition and oxidation on Pd(111) by PM-IRAS and XPS spectroscopy*. Journal of Physical Chemistry B, 2005. **109**(38): p. 17791-17794.

173. Teschner, D., et al., *High-pressure X-ray photoelectron spectroscopy of palladium model hydrogenation catalysts. Part 2: Hydrogenation of trans-2-pentene on palladium*. Journal of Catalysis, 2005. **230**(1): p. 195-203.
174. Renaud, G., Barbier, A., Robach, O., *Growth, structure, and morphology of the Pd/MgO(001) interface: Epitaxial site and interfacial distance*. Physical Review B, 1999. **60**(8): p. 5872-5882.
175. Bowker, M., et al., *Model catalyst studies of the strong metal-support interaction: Surface structure identified by STM on Pd nanoparticles on TiO<sub>2</sub>(110)*. Journal of Catalysis, 2005. **234**(1): p. 172-181.
176. Min, B.K., Santra, A. K., Goodman, D. W., *Understanding silica-supported metal catalysts: Pd/silica as a case study*. Catalysis Today, 2003. **85**(2-4): p. 113-124.
177. Meyer, R., Shaikhutdinov, S. K., Freund, H. J., *CO oxidation on a Pd/Fe<sub>3</sub>O<sub>4</sub>(111) model catalyst*. Zeitschrift Fur Physikalische Chemie-International Journal of Research in Physical Chemistry & Chemical Physics, 2004. **218**(8): p. 905-914.
178. Schalow, T., et al., *Oxygen storage at the metal/oxide interface of catalyst nanoparticles*. Angewandte Chemie-International Edition, 2005. **44**(46): p. 7601-7605.
179. Schalow, T., et al., *Size-dependent oxidation mechanism of supported Pd nanoparticles*. Angewandte Chemie-International Edition, 2006. **45**(22): p. 3693-3697.
180. Schalow, T., et al., *CO oxidation on partially oxidized Pd nanoparticles*. Journal of Catalysis, 2006. **242**(1): p. 58-70.
181. Schalow, T., et al., *Oxygen-induced restructuring of a Pd/Fe<sub>3</sub>O<sub>4</sub> model catalyst*. Catalysis Letters, 2006. **107**(3-4): p. 189-196.
182. Wilde, M., et al., *Influence of Carbon Deposition on the Hydrogen Distribution in Pd Nanoparticles and Their Reactivity in Olefin Hydrogenation*. Angewandte Chemie-International Edition, 2008. **47**(48): p. 9289-9293.
183. Brandt, B., et al., *Isomerization and hydrogenation of cis-2-butene on Pd model catalyst*. Journal of Physical Chemistry C, 2008. **112**(30): p. 11408-11420.
184. Ludwig, W., et al., *Role of Low-Coordinated Surface Sites in Olefin Hydrogenation: A Molecular Beam Study on Pd Nanoparticles and Pd(111)*. Chemphyschem, 2010. **11**(11): p. 2319-2322.
185. Meyer, R., et al., *Two-dimensional growth of Pd on a thin FeO(111) film: a physical manifestation of strong metal-support interaction*. Surface Science, 2003. **546**(2-3): p. L813-L819.
186. Bozonverduraz, F., et al., *Chemical State and Reactivity of Supported Palladium .I. Characterization by XPS and UV-Visible Spectroscopy*. Journal of Catalysis, 1978. **53**(1): p. 126-134.
187. Fleisch, T.H., Hicks, R. F., Bell, A. T., *An XPS Study of Metal Support Interactions on Pd/SiO<sub>2</sub> and Pd/La<sub>2</sub>O<sub>3</sub>*. Journal of Catalysis, 1984. **87**(2): p. 398-413.
188. Egelhoff, W.F., Tibbetts, G. G., *Growth of Copper, Nickel, and Palladium Films on Graphite and Amorphous-Carbon*. Physical Review B, 1979. **19**(10): p. 5028-5035.
189. Mason, M.G., *Electronic-Structure of Supported Small Metal-Clusters*. Physical Review B, 1983. **27**(2): p. 748-762.
190. Wertheim, G.K., Dicenzo, S. B., Youngquist, S. E., *Unit Charge on Supported Gold Clusters in Photoemission Final-State*. Physical Review Letters, 1983. **51**(25): p. 2310-2313.
191. Marks, F.A., Lindau, I., Browning, R., *Characterization of the Pd/ $\alpha$ -Al<sub>2</sub>O<sub>3</sub> Supported Cluster System*. Journal of Vacuum Science & Technology a-Vacuum Surfaces and Films, 1990. **8**(4): p. 3437-3442.

192. Tysoe, W.T., Lambert, R. M., *Structure and Reactivity at the Halogen Metal Interface - Chemisorption, Corrosion and Reaction Pathways in the Pd(111)-Cl<sub>2</sub> System*. Surface Science, 1988. **199**(1-2): p. 1-12.
193. Agostini, G., et al., *Preparation of Supported Pd Catalysts: From the Pd Precursor Solution to the Deposited Pd<sup>2+</sup> Phase*. Langmuir, 2010. **26**(13): p. 11204-11211.
194. Simonov, P.A., Troitskii, S. Y., Likholobov, V. A., *Preparation of the Pd/C catalysts: A molecular-level study of active site formation*. Kinetics and Catalysis, 2000. **41**(2): p. 255-269.
195. Peuckert, M., *XPS study on surface and bulk palladium oxide, its thermal stability, and a comparison with other noble-metal oxides*. Journal of Physical Chemistry, 1985. **89**(12): p. 2481-2486.
196. Agostini, G., et al., *Determination of the Particle Size, Available Surface Area, and Nature of Exposed Sites for Silica-Alumina-Supported Pd Nanoparticles: A Multitechnical Approach*. Journal of Physical Chemistry C, 2009. **113**(24): p. 10485-10492.
197. Farrauto, R.J., et al., *Thermal-Decomposition and Reformation of PdO Catalysts - Support Effects*. Applied Catalysis B-Environmental, 1995. **6**(3): p. 263-270.
198. Schalow, T., et al., *Particle size dependent adsorption and reaction kinetics on reduced and partially oxidized Pd nanoparticles*. Physical Chemistry Chemical Physics, 2007. **9**(11): p. 1347-1361.
199. Brown, M.A., et al., *Oxidation of Au by Surface OH: Nucleation and Electronic Structure of Gold on Hydroxylated MgO(001)*. Journal of the American Chemical Society. **133**(27): p. 10668-10676.
200. Veith, G.M., Lupini, Andrew R., Dudney, Nancy J., *Role of pH in the Formation of Structurally Stable and Catalytically Active TiO<sub>2</sub> Supported Gold Catalysts*. Journal of Physical Chemistry C, 2009. **113**(1): p. 269-280.
201. Szanyi, J., Kuhn, W. K., Goodman, D. W., *CO Adsorption on Pd(111) and Pd(100) - Low and High-Pressure Correlations*. Journal of Vacuum Science & Technology a-Vacuum Surfaces and Films, 1993. **11**(4): p. 1969-1974.
202. Frank, M., Baumer, M., *From atoms to crystallites: adsorption on oxide-supported metal particles*. Physical Chemistry Chemical Physics, 2000. **2**(17): p. 3723-3737.
203. Wolter, K., et al., *Infrared spectroscopic investigation of CO adsorbed on Pd aggregates deposited on an alumina model support*. Surface Science, 1998. **399**(2-3): p. 190-198.
204. Imbihl, R., Demuth, J. E., *Adsorption of Oxygen on a Pd(111) Surface Studied by High-Resolution Electron-Energy Loss Spectroscopy (EELS)*. Surface Science, 1986. **173**(2-3): p. 395-410.
205. Meusel, I., et al., *The interaction of oxygen with alumina-supported palladium particles*. Catalysis Letters, 2001. **71**(1-2): p. 5-13.
206. Shaikhutdinov, S., et al., *Interaction of oxygen with palladium deposited on a thin alumina film*. Surface Science, 2002. **501**(3): p. 270-281.
207. Conrad, H., et al., *Interaction of NO and O<sub>2</sub> with Pd(111) Surfaces .2*. Surface Science, 1977. **65**(1): p. 245-260.
208. Milun, M., et al., *Thermal-Desorption Spectroscopy of the O<sub>2</sub>/Pd(110) System*. Surface Science, 1989. **211**(1-3): p. 887-895.
209. Voogt, E.H., et al., *Adsorption of oxygen and surface oxide formation on Pd(111) and Pd foil studied with ellipsometry, LEED, AES and XPS*. Surface Science, 1997. **373**(2-3): p. 210-220.
210. Legare, P., et al., *Interaction of Oxygen and Hydrogen with Palladium*. Surface Science, 1981. **107**(2-3): p. 533-546.

211. Gabasch, H., et al., *Comparison of the reactivity of different Pd-O species in CO oxidation*. Physical Chemistry Chemical Physics, 2007. **9**(4): p. 533-540.
212. Hendriksen, B.L.M., Bobaru, S. C., Frenken, J. W. M., *Oscillatory CO oxidation on Pd(100) studied with in situ scanning tunneling microscopy*. Surface Science, 2004. **552**(1-3): p. 229-242.
213. Borchert, H., et al., *Pd nanoparticles with highly defined structure on MgO as model catalysts: An FTIR study of the interaction with CO, O<sub>2</sub>, and H<sub>2</sub> under ambient conditions*. Journal of Catalysis, 2007. **247**(2): p. 145-154.
214. Christmann, K., *Interaction of Hydrogen with Solid-Surfaces*. Surface Science Reports, 1988. **9**(1-3): p. 1-163.
215. Doyle, A.M., et al., *Hydrogenation on metal surfaces: Why are nanoparticles more active than single crystals?* Angewandte Chemie-International Edition, 2003. **42**(42): p. 5240-5243.
216. Shaikhutdinov, S., et al., *Structure-reactivity relationships on supported metal model catalysts: Adsorption and reaction of ethene and hydrogen on Pd/Al<sub>2</sub>O<sub>3</sub>/NiAl(110)*. Journal of Catalysis, 2001. **200**(2): p. 330-339.
217. Neyman, K.M., Schauermaun, Svetlana, *Hydrogen Diffusion into Palladium Nanoparticles: Pivotal Promotion by Carbon*. Angewandte Chemie-International Edition, 2010. **49**(28): p. 4743-4746.
218. Teschner, D., et al., *The roles of subsurface carbon and hydrogen in palladium-catalyzed alkyne hydrogenation*. Science, 2008. **320**(5872): p. 86-89.
219. Bernal, S., et al., *Some recent results on metal/support interaction effects in NM/CeO(2) (NM : noble metal) catalysts*. Catalysis Today, 1999. **50**(2): p. 175-206.
220. Benson, J.E., Kohn, H. W., Boudart, M., *On Reduction of Tungsten Trioxide Accelerated by Platinum and Water*. Journal of Catalysis, 1966. **5**(2): p. 307-&.
221. Sermon, P.A., Bond, G. C., *Hydrogen Spillover*. Catalysis Reviews-Science and Engineering, 1973. **8**(2): p. 211-239.
222. Tauster, S.J., Fung, S. C., Garten, R. L., *Strong Metal-Support Interactions - Group-8 Noble-Metals Supported on TiO<sub>2</sub>*. Journal of the American Chemical Society, 1978. **100**(1): p. 170-175.
223. Tauster, S.J., *Strong Metal-Support Interactions*. Accounts of Chemical Research, 1987. **20**(11): p. 389-394.
224. Beard, B.C., Ross, P. N., *Pt-Ti Alloy Formation from High-Temperature Reduction of a Titania-Impregnated Pt Catalyst - Implications for Strong Metal Support Interaction*. Journal of Physical Chemistry, 1986. **90**(26): p. 6811-6817.
225. Pesty, F., Steinruck, H. P., Madey, T. E., *Thermal-Stability of Pt Films on TiO<sub>2</sub>(110) - Evidence for Encapsulation*. Surface Science, 1995. **339**(1-2): p. 83-95.
226. Suzuki, T., Souda, R., *The encapsulation of Pd by the supporting TiO<sub>2</sub>(110) surface induced by strong metal-support interactions*. Surface Science, 2000. **448**(1): p. 33-39.
227. Dulub, O., Hebenstreit, W., Diebold, U., *Imaging cluster surfaces with atomic resolution: The strong metal-support interaction state of Pt supported on TiO<sub>2</sub>(110)*. Physical Review Letters, 2000. **84**(16): p. 3646-3649.
228. Tauster, S.J., et al., *Strong-Interactions in Supported-Metal Catalysts*. Science, 1981. **211**(4487): p. 1121-1125.
229. Wang, S.Y., Moon, S. H., Vannice, M. A., *The Effect of SMSI (Strong Metal-Support Interaction) Behavior on Co Adsorption and Hydrogenation on Pd Catalysts .2. Kinetic-Behavior in the Methanation Reaction*. Journal of Catalysis, 1981. **71**(1): p. 167-174.

230. Fan, L., Fujimoto, K., *Reaction mechanism of methanol synthesis from carbon dioxide and hydrogen on ceria-supported palladium catalysts with SMSI effect*. Journal of Catalysis, 1997. **172**(1): p. 238-242.
231. Tsubaki, N., Fujimoto, K., *Promotional SMSI effect on supported palladium catalysts for methanol synthesis*. Topics in Catalysis, 2003. **22**(3-4): p. 325-335.
232. Freund, H.J., et al., *CO Oxidation as a Prototypical Reaction for Heterogeneous Processes*. Angewandte Chemie-International Edition, 2011. **50**(43): p. 10064-10094.
233. Zhu, G.H., et al., *Coverage of palladium by silicon oxide during reduction in H<sub>2</sub> and complete oxidation of methane*. Journal of Catalysis, 2004. **225**(1): p. 170-178.
234. Hong, C.T., Yeh, C. T., Yu, F. H., *Effect of Reduction and Oxidation Treatments on Pd/ZnO Catalysts*. Applied Catalysis, 1989. **48**(2): p. 385-396.
235. Penner, S., et al., *Pd/Ga<sub>2</sub>O<sub>3</sub> methanol steam reforming catalysts: Part I. Morphology, composition and structural aspects*. Applied Catalysis a-General, 2009. **358**(2): p. 193-202.
236. Rainer, D.R., et al., *Adsorption of CO on Pd/Al<sub>2</sub>O<sub>3</sub>/Ta(110) model catalysts*. Journal of Vacuum Science & Technology a-Vacuum Surfaces and Films, 1996. **14**(3): p. 1184-1188.
237. Felicissimo, M.P., et al., *Characterization of a Pd-Fe bimetallic model catalyst*. Surface Science, 2007. **601**(10): p. 2105-2116.
238. Xu, X.P., Goodman, D. W., *An Infrared and Kinetic-Study of CO Oxidation on Model Silica-Supported Palladium Catalysts from 10<sup>-9</sup> to -15 Torr*. Journal of Physical Chemistry, 1993. **97**(29): p. 7711-7718.
239. Rodriguez, J.A., Campbell, R. A., Goodman, D. W., *The Nature of Metal-Metal Bonding at Bimetallic Interfaces*. Surface Science, 1994. **307**: p. 377-383.
240. Wimmers, O.J., Arnoldy, P., Moulijn, J. A., *Determination of the Reduction-Mechanism by Temperature-Programmed Reduction - Application to Small Fe<sub>2</sub>O<sub>3</sub> Particles*. Journal of Physical Chemistry, 1986. **90**(7): p. 1331-1337.
241. Xu, L.Q., et al., *Formation of PdFe Alloy Clusters in Zeolite-Y*. Journal of Physical Chemistry, 1993. **97**(44): p. 11517-11523.
242. Garten, R.L., Ollis, D. F., *Chemical State of Iron in Reduced PdFe-Al<sub>2</sub>O<sub>3</sub> Catalysts*. Journal of Catalysis, 1974. **35**(2): p. 232-246.
243. Qin, Z.H., et al., *Encapsulation of Pt nanoparticles as a result of strong metal-support interaction with Fe<sub>3</sub>O<sub>4</sub> (111)*. Journal of Physical Chemistry C, 2008. **112**(27): p. 10209-10213.
244. Zheng, G., Altman, E. I., *The reactivity of surface oxygen phases on Pd(100) toward reduction by CO*. Journal of Physical Chemistry B, 2002. **106**(5): p. 1048-1057.